# ABSTRACT

Title of Dissertation: LASER RANGE IMAGING FOR ON-LINE MAPPING OF 3D IMAGES TO PSEUDO-X-RAY IMAGES FOR POULTRY BONE FRAGMENT DETECTION

Hansong Jing, Doctor of Philosophy, 2003

Dissertation Directed by: Associate Professor Dr. Yang Tao
Department of Biological Resources Engineering

A laser ranging image system was developed for on-line high-resolution 3D shape recovery of poultry fillets. The range imaging system in conjunction with X-ray imaging was used to provide synergistic imaging detection of bone fragments in poultry fillets. In this research, two 5 mW diode lasers coupled with two CCD cameras were used to produce 3D information based on structured lights and triangulation. A laser scattering phenomenon on meat tissues was studied when calculating the object thickness. To obtain the accurate 3D information, the cameras were calibrated to correct for camera distortions. For pixel registrations of the X-ray and laser 3D images, the range imaging system was calibrated, and noises and signal variations in the X-ray and laser 3D images were analyzed. Furthermore, the relationship between the X-ray absorption and 3D thickness of fillets was obtained, and a mapping function based on this relationship was applied to convert the fillet 3D images into the pseudo-X-ray images. For the on-line system implementation, the imaging hardware and software engineering issues, including the data flow optimization and the operating system task scheduling, were also studied. Based on the experimental on-line test, the range imaging system developed was able to scan poultry fillets at a speed of 0.2 m/sec at a resolution of 0.8(X) x 0.7(Y) x 0.7(Z) $mm^3$. The results of this study have shown great potential for non-invasive detection of hazardous materials in boneless poultry meat with uneven thickness.

# LASER RANGE IMAGING FOR ON-LINE MAPPING OF 3D IMAGES TO PSEUDO-X-RAY IMAGES FOR POULTRY BONE FRAGMENT DETECTION

by

Hansong Jing

Thesis submitted to the Faculty of the Graduate School of the
University of Maryland, College Park in partial fulfillment
of the requirements for the degree of
Doctor of Philosophy
2003

Advisory Committee:

Dr. Yang Tao, Chair
Dr. Lewis Carr
Dr. Ramalingam Chellappa
Dr. Yud-Ren Chen
Dr. Arthur T. Johnson
Dr. Fredrick Wheaton

To Yongqi Yan

# ACKNOWLEDGEMENTS

I would like to thank my dissertation advisor, Dr. Yang Tao, for his invaluable guidance and insight into all the aspects of this research. I would also like to thank Dr. Lewis Carr, Dr. Fredrick Wheaton, Dr. Arthur T. Johnson, Dr. Yud-Ren Chen, and Dr. Ramalingam Chellappa for their time, support, and helpful criticisms during my research and academic development. I especially thank Dr. Lewis Carr who provided all the samples for our experiment.

I would like to express my gratitude to all present and former members of the Bio-Imaging Laboratory. I would also like to thank Mr. Gary Seibel for his shop assistance and Ms. Abby Vogel for providing invaluable suggestions.

Finally, I would like to extend my deepest gratitude to my family for their love, support, and sacrifice during my study at the University of Maryland.

# TABLE OF CONTENTS

# LIST OF TABLES

# LIST OF FIGURES

# LIST OF SYMBOLS

List of symbols for Chapter 2

| | |
|---|---|
| $R/C$ | Ratio of Rayleigh and Campton. |
| $\lambda$ | Wavelength. |
| $\lambda_\mathrm{b}$ | Starting wavelength. |
| $\lambda_\mathrm{e}$ | Ending wavelength. |
| $L$ | Length of spectrum area. |
| $d$ | Distance from wavelength $\lambda_b$ to $\lambda$. |
| $g$ | Distance between light source and linear wavelength filter (LWF). |
| $\beta$ | Angle between light source and LWF. |
| $\theta$ | Angle |
| $f$ | Focal length of the camera. |
| $(u,v)$ | Image plane. |
| $b$ | Base line distance between the light source and sensor center. |

List of symbols for Chapter 4

| | |
|---|---|
| $\theta_x$ | Angle between z-axis and x-axis. |
| $\theta_y$ | Angle between z-axis and x-axis. |
| $f$ | Focal length of the camera. |
| $(x_i\ y_i)$ | Coordinates of image. |
| $(x_0, y_0, z_0)$ | Coordinates of object. |
| $(x_s, y_s, z_s)$ | Coordinates of a known point |
| $z_{ref}$ | Calibration distance. |
| $\Delta x_i$ | Displacement in x direction. |
| $\Delta y_i$ | Displacement in y direction. |
| $T_{c1}$ | Coordinates matrix for camera I. |
| $T_{c2}$ | Coordinates matrix for camera II. |
| $T_t$, $T_z$ | Translation matrix |

List of symbols for Chapter 5

| | |
|---|---|
| $f(\mathrm{x})$ | Image line function |
| $h(x)$ | Impulse response of system. |
| $n(x)$ | Noise added to the original signal. |
| $I(x)$ | Symmetric Gaussian distribution |
| $\mu$ | Mean. |
| $\sigma$ | Standard deviation. |

| | |
|---|---|
| $I_0$ | Total incident strength. |
| $\xi$ | Index used to represent the energy lost by absorption and scattering. |
| $s(x)$ | Scattered light. |
| $c(x,y)$ | Function of x coordinates. |
| $q(x,y)$ | Function of y coordinates. |
| $g(x,y)$ | Function of gray value of the respondent pixel. |
| $S$ | Result image. |
| $R$ | Vector to represent local region. |
| $M$ | Mask used to enhance the edge. |
| $CR(x)$ | Light intensity received by the camera. |
| $\beta$ | Angle between the laser beam plane and camera axis plane. |
| $c(\theta)$ | Polar form of the image intensity. |
| $r(\theta)$ | Polar form of s(x). |
| $\theta$ | Angle between incident light and object surface. |
| $CI(x)$ | Center of the profile. |
| $C(x)$ | Centroid. |
| $K$ | Shift of the scatter. |
| $\varphi$ | Symmetrical index. |
| $x(P)$ | Peak position of profile. |
| $p_i$ | Calculated depth. |
| $P_i$ | Depth of reference object. |
| $i$ | Index of the point |

List of Symbols for Chapter 6

| | |
|---|---|
| $\alpha$ | Angle of sensor plane rotates around Z axe of the world coordinates |
| $\beta$ | Angle of sensor plane rotates around X axe of the world coordinates |
| $\gamma$ | Angle of sensor plane rotates around Y axe of the world coordinates |
| $f$ | Focal length of the lens |
| $\theta$ | Actual angle between the two lens axes |
| $d_u$ | Scale factors in the horizontal directions |
| $d_v$ | Scale factors in the vertical directions |
| $p(u',v',1)$ | Point in the obtained image |
| $P(x,y,z,1)$ | Point in world coordinate system |
| $x'', y''$ | Coordinates of the distorted normalized image |
| $xi, yi$ | Coordinates in the ideal normalized image coordinate system |
| $k_1, K_2$ | Two non-linear indices |
| $u', v'$ | Actual coordinates in the sensor plane |
| $u, v$ | Ideal coordinates in the sensor plane |
| $u_0, v_0$ | Shifted sensor center from the ideal center position |
| $R$ | Rotation matrix of the world coordinates to the lens coordinates system |
| $R'$ | Actual rotation matrix |
| $u_{x0}$ | Deviation from the ideal coordinates center |
| $xt_x, xt_y$ | Translation of origin of the world coordinates to the X-ray coordinate system origin |
| $d_x$ | Scale factor of the X-ray detector |
| $I_0$ | X-ray's incident intensity |
| $\rho$ | Medium density |

| | |
|---|---|
| $\mu/\rho$ | Mass-energy absorption coefficient |
| $d$ | Geometrical thickness of the object |
| $u_a,v_a$ | Real image position in the X-ray coordinate system |
| $u_b,v_b$ | Projection coordinate of point ($u_a,v_a$) in the detector plane |
| $v'$ | Original height of object |
| $v''$ | Transformed height of object |
| $p$ | Encoder resolution |
| $\delta$ | Distortion caused by lens distortion |
| $\delta_\mu,\delta_v$ | Distortion in the $u,v$ directions |
| $\Delta\delta_u,\Delta\delta_v$ | Distortion rate in the $u$ and $v$ directions |

## List of Symbols for Chapter 7

| | |
|---|---|
| $v(x,y)$ | Obtained image |
| $\eta(x,y)$ | Various noise added to the system |
| $u(x,y)$ | Original image |
| $w(x,y)$ | The image getting by convoluting the original image with a image system's impulse response |
| $h(x,y)$ | Image system's impulse response |
| $g$ | The function that models the characteristics of the image system. |
| $\bar{g}$ | Spatial average of $g$ |
| $f$ | Noise function of photo-electronic systems |
| $\eta_1$ | Additive wideband thermal noise which is multiplicative and signal dependent. |
| $\eta_2$ | Additive wideband thermal noise |
| $I_0$ | Intensity of the detected X-ray energy when the object is homogeneous |
| $\rho$ | Medium density |
| t | Medium thickness |
| $I$ | Intensity of the detected X-ray energy |
| $T_i$ | The X-ray path length |
| $I_R$ | Intensity of the detected X-ray energy when the object isn't homogeneous |
| $\bar{I}_R$ | Spatial average of $I_R$ |
| $I_A$ | Actual energy received by X-ray detector |
| $T_A$ | Obtained image intensity |
| $T(x,y)$ | Original image |
| $\delta$ | Additive Gaussian noise |
| Y | An (n×1) vector of observations of the response variable |
| X | (n×p) matrix contains the n observations on the p predictors |
| $W$ | Diagonally weighted matrix |
| $s$ | A scale factor |
| $e_i$ | residual |
| ε | Vector of error terms in a normal regression model |
| $\Lambda_{\varepsilon_i}$ | Variances of the residual $\varepsilon_i$ |

# Chapter 1

# INTRODUCTION

From 1970 to 1996, the consumption of poultry products increased 90% while consumption of traditional red meat (beef and pork) decreased 15% (USDA, 1998). In 1999, the United States produced over 40 billion pounds of poultry and 41% of that total was boneless meat (USDA, 1999). During the de-boning operation, bone fragments left in de-boned meat have been one of the major concerns of the poultry industry. To avoid accidental ingestion, USDA regulations state that all boneless poultry products must be free of any kind of bones.

The most common technological means to satisfy USDA regulations regarding boneless meat products is to use an X-ray inspection system to detect bone fragments, and then remove these fragments before the meat fillets are packaged or further processed. The X-ray absorption by the fillet is different depending on the thickness, whether a bone fragment is present or not. The X-ray energy reaching the image detector varies in proportion to the fillet thickness, thus the X-ray image does not have an even intensity. Consequently, X-ray absorption differences due to uneven meat thickness inevitably produce false patterns in X-ray images; making it very difficult to distinguish between bone fragments and normal meat patterns even by visual inspection of X-ray images. Frequently, various bone fragments, especially the less-calcified bone fragments, are camouflaged in the meat by false patterns; which makes it very difficult to find them in the X-ray image. Actually, X-ray inspection systems currently being used have a high failure rate of over 30% according to major poultry companies (Poultry companies, 1998).

To resolve the bone fragment problem, a novel non-invasive inspection method for physical contaminant detection in poultry packing lines was proposed by Tao (1997), and Jing, et al., (1999, 2000). The method combined laser-based range imaging and conventional X-ray imaging to compensate for thickness variation in poultry meat and provided higher sensitivity and accuracy to detect hazardous objects during bone fragment detection.

Although laser-based range imaging has been investigated and applied in various applications (Rioux, et al., 1991, Borghese, et al., 1998), major difficulties remain in developing a range imaging system for the detection of bone fragments. First, due to the physical property of poultry meat, a severe scattering phenomenon occurs when strong coherent laser light is projected onto the surface of the poultry meat. As a result of laser light scattering in biomaterials, common methods used to recover object height are incapable of producing accurate measurements. Second, in the combined X-ray and laser ranging image detection system, two different types of imagers are employed. Thus, pixel registrations between the X-ray and laser images must be done so that the two images can be integrated. Because on-line processing is required for the detection system, fast and accurate algorithms are essential to correct image distortions and align both the X-ray and laser 3D images. Third, the imaging principles are different for the X-ray and 3D range systems. In X-ray imaging, the intensity of the image represents the absorption of the X-rays along the light travel path, while the 3D image intensity represents the thickness/depth information. Therefore, image mapping is essential when information from both images is needed. Due to the complexity of biological materials, the variations such as meat ages, compositions, and bones are inevitably coupled into the image signal. Thus, transformations are required to convert the 3D image into a pseudo-X-ray image without the influence of the variations. Finally, in the practical system design, the image processing hardware and operating system data flow scheduling for real-time image processing must be carefully designed. In this dissertation, the on-line 3D range imaging system will be presented as part of the combined X-ray bone fragment detection system that meets the above requirements.

The dissertation is organized as follows. A review of literature is given in Chapter 2. Objectives are provided in Chapter 3. Detailed descriptions of the combined X-ray and laser imaging system and the laser range method are provided in Chapter 4. Then, several problems encountered during the dual imaging system development are discussed. In Chapter 5, the method used to recover the scattered laser lines is described. Chapter 6 summarizes the approach to calibrate various optical devices used in the dual imaging system. In Chapter 7, the X-ray and laser 3D image noise models are analyzed and a robust regression method to obtain the mapping coefficients is described. The software and hardware environments are analyzed in Chapter 8. The overall conclusion for the dissertation is given in Chapter 9. Suggestions for further study are given in Chapter 10.

# Chapter 2

# LITERATURE REVIEW

## 2.1 Review of Bone Fragment Detection Methods

The X-ray imaging technique is among the major methods used for solving non-destructive inspection problems. The research most related to the proposed project was done by Schatzki, et al. (1996) and Schatzki, et al.(1997). In their work, a remarkable study was conducted to test the efficacy of detecting particulate contaminants in processed meat samples as a function of meat thickness and texture of X-ray images. Visual recognition of contaminants in meat samples as a function of meat thickness, size, shape, and texture of X-ray images was studied and analyzed. It was found that inclusions were more difficult to recognize in textured X-ray images, and the errors varied with the size, shape, and thickness of the inclusions and samples. As a new approach, Morita, et al. (1997) proposed an X-ray system for detecting foreign materials in food and agricultural products by employing soft X-ray radiation and a high resolution image intensifier. Also, a noteworthy study of X-ray imaging for the accurate detection of bone and cartilage fragments in poultry meat was presented by Papanicolopoulos, et al. (1992). Their research was based on Rayleigh X-ray scattering and the ratio of Rayleigh and Campton (R/C) scattering. The implementation, however, demanded a very precise angle (0.1 degrees) for the detection, because at slightly different angles, the R/C value indicated materials with an atomic number different from meat. Moreover, because scattering occurred while using this method, noises were coupled in the useful signal, making it difficult to achieve the needed resolution and accuracy for this application. More importantly, as in any other method, the uneven thickness of each piece of meat (and from one piece to the next) caused vital problems such as incident energy variation, transmission field intensity variation, detection shifting, and scattering changes as realized by the investigators. Papanicolopoulos's X-ray system unit cost nearly $900,000, making it infeasible for the poultry processing industry. Renesse and Klumper (1993) discussed the existence of food contaminated with glass and the consequent need for efficient inspection. General detection methods including optical inspection, X-ray, acoustic, and microwave detection were addressed as possible future solutions to the problem. Significant work was also performed by Tollner and Murphy (1991), Tollner (1993), Thai, et al. (1991), Harrison, et al. (1993), Chen, et al. (1992), Brecht, et al. (1991), and Munier and House (1989) in X-ray inspection of agricultural materials.

To overcome X-ray absorption variations due to uneven meat thickness, meat was submerged in water for thickness compensation. Because poultry fillets are largely water, the method worked very well; however, sanitation, cross-contamination, and dirty water disposal were obvious problems, preventing any practical use (EG&G, 1995).

Commercial equipment exists for detection of metal and other foreign materials, but these inspection systems are ineffective or inaccurate when inspecting meats of uneven thickness (EG&G,1995). EG&G Inc.(1995) developed a system consisting of an X-ray tube and a line scan detector, but the machine had a very high error rate. A pressing belt was used to press the meat to an homogeneous thickness, but meats, such as chicken breasts, which are thick in the center and thin on the edges, cannot be compressed enough to correct for uneven thickness. The uneven thickness of meat causes the X-ray image to be of irregular intensity even when no foreign objects are present, making recognition of bone fragments very difficult.

To overcome thickness variations, Thermo Goring Kerr Inc.(2003) used a pump to press meat into a pipe and then compress the meat into a rectangular block for viewing by an X-ray system. The method worked particularly well for ground meats, but did not work for whole meats because of meat damage. Furthermore, the rejection of the contaminated meat in the pipe becomes a problem, because a large section of meat flow has to be rejected, causing considerable false rejections.

Another method currently under investigation is the X-ray dual energy method, which is frequently used in the biomedical engineering area (Devic, et al., 2000, Redus, et al., 2002, Wagner, et al., 1989, Wojcik, et al., 1996, and Zhao and Jiang, 1992). However, due to the significant variation of physical characteristics of various bone fragments, algorithm complexity, and high cost, this method has limited use in the detection of small bone fragments in poultry products.

## 2.2 Methods for Range Measurement

Various techniques have been used to obtain object thickness information. For example, there are mechanical methods such as contact-probe-type coordinate-measuring machines (CMMs) and acoustic methods such as ultrasound used by Motluk (1997) to produce a three-dimensional image of the human brain.

The most widely used methods for range imaging are optical-based because they are flexible, accurate, and non-invasive. Strand (1985) classified the optical range sensing techniques into four categories: geometric range measurement, time-of-flight range measurement, interferometric, and diffraction range measurement.

Geometric range measurement techniques are based on triangulation. If two triangles are congruent to each other, their corresponding sides are in proportion and the corresponding angles are equal. Then with the information of a reference triangle, all the parameters of the other triangle can be determined by partial knowledge of this triangle. In practice, some geometric pattern is projected onto the object to help calculate the depth/shape of the object. A multi-stripe structured light system proposed by Sorgel (1997) for the recognition of cylindrical surfaces is an example of the geometric range measurement technique.

The time-of-flight range measurement techniques are based on the measurement of light wave flight time. Usually, the light transmission speed is known in certain environmental media. The time of flight of light can be calculated by measuring the phase shift of a modulated light beam after the wave reflects back from the measured object (Strand, 1985). Other methods have also been adopted to measure the time. Seta and O'ishi. (1990) proposed a distance meter utilizing the intermode beat of a He-Ne laser instead of an optical modulator. Its performance was tested at distances between 10 and 1300 m on a 300 m baseline in a tunnel. The resolution was about 20 μm and the total uncertainty was within 0.1 mm, if the air was stable. Because the light travelled very fast, it was more suitable to measure long distances. Using this method, the result was usually very accurate if the environmental media was stable, but a very complicated device was needed to measure the distance. Note that this method measured only one point instead of an image because light beams spread out over distance.

The interferometric techniques are based on interferometry, a method that utilizes the interference of waves for precise determinations of distance. In the measurement, a reference plane is used. The same light is projected on both the reference plane and the object by a beam splitter. If the distance from the light source to the reference plane and object is different, an interference pattern can be observed by interfering two reflected waves from the two surfaces. In this way, the optical path length variations are measured and the shape of the surface is obtained (Pratt, 1991). Another use of this concept is the lens-less camera suggested by Marks (1999) which captures planes of mutual intensity data to reconstruct an incoherently illuminated visible object in three dimensions. The interferometer technique is extremely sensitive, and can get the depth with an accuracy of $\lambda/100$, or better, where $\lambda$ is the wavelength. The drawback of interferometric methods is that they are highly sensitive to temperature gradients and are easily disturbed by air turbulence and vibrations.

Diffraction range measurement techniques are used the least in range measurements. The method is based on the diffraction of reflected incident light that strickes on the measured surface. Based on this technique, Farid and Simoncelli (1998) used a single stationary camera and a pair of calibrated optical masks to measure this differential quantity directly. After changing the aperture size, the subsequent computation of the range image involves simple arithmetic operations and is suitable for real-time implementation.

In spite of the optical methods mentioned above, there are many other optical methods available to find the surface shape of an object. Moiré techniques can be used to get depth information. The basis of Moiré techniques is to project a set of white and black stripes, or gratings, on the object. The grating can be of any shape. Normally two identical gratings are used with one serving as a reference grating. The difference of these two gratings is used to determine the deformation or contour of the object (Pratt, 1991). The resolution of this method depends on the pitch of the gratings. Because two images are needed to calculate the depth, it is difficult to apply this on-line.

Shapes can also be recovered from shading (Horn, et al., 1988, Frankot and Chellappa, 1987), from a sequence of images (Poelman and Kanade, 1993), or from a video stream (Zhao and Chellppa, 2001). Although these methods can be successful in specific applications, they can be implemented in real-time applications to achieve high depth resolution only if high computation power is used.

Deng and Wang (1994) used a non-interferometric technique for high-resolution distance measurements. The technique utilized the theory that the wavelength of a broadband continuous wave (CW) laser can be changed by external feedback. The design let the reflected beam feed back into the laser cavity to change the wavelength of the laser. To produce a position-sensitive feedback, the ranging target was put near the focal point of a microscope objective. The optical devices were designed to have a large numerical aperture for obtaining a short con-focal parameter. In Deng's experiment, a 20 nm longitudinal resolution and a 0.8 μm transverse resolution were obtained. Among other techniques, Glaser and Konforti (1992) used a camera with an astigmatic lens to get the range information. Krishnan and Ahuja (1996) used a non-frontal imaging camera to get the range image.

A high-resolution laser range system based on geometric triangulation is non-intrusive, can be very accurate depending on the imaging device used, and has a fast data acquisition rate. These systems are widely used in industrial inspections, biomedical imaging, and other various applications. In fact, most commercially available non-contact laser-based systems are based on geometric triangulation. This method has faster data acquisition rates than the probe-type CMMs and ultrasound-based systems and measures object depth without touching the object. However, the ambient light, the occlusion, the laser speckle and scattering phenomena, and object surface properties affect the accuracy of the depth information captured by the detectors in many of these systems. Compared with devices designed using the time-of-flight method, triangulation laser range imaging systems are usually simpler and more compact. But measured depth accuracy by time-of-flight systems are not affected by the depth of field, while the triangulation method's measurement accuracy is limited by its depth of field. Interferometric, Moiré and diffraction based methods can have very high depth resolution. However, it is more suitable to use them when measuring small deformation or depth variation. Because the comparison of two images is usually needed, these methods are not likely to be used in real-time applications. Although retrieving the shape from shading or video methods does not require very complex instruments, currently the computational power is not high enough to process the images on-line when high depth resolution is required.

## 2.3 Structured Light-Based Laser Range Imaging

The triangulation-based laser ranging method has wide application. This method is simple to be implemented and has high accuracy. Industrial companies often used it for dimension control in the 1980s (Pirlet, et al., 1986). To allow a 360 degree examination of an object, Godhwani, et al. (1994) used six cameras to construct a multi-sensor structured light range scanner. Six Charge Injection Device (CID) cameras were installed around the target and six projectors were used to project light patterns onto the surface of the object. The areas scanned by neighboring cameras were significantly overlapped. The cameras and projectors were calibrated to a fixed configuration. A block of known size with circular ring patterns was used to calibrate these optical devices. In the overlapped segments, a linear interpolation algorithm had to be applied to overcome the non-continuity of data from different cameras. This system scanned an object in 0.75 second with 0.25 mm accuracy. Because twelve devices were used in the system, the calibration process was very complex, and because only co-planar points were used in the calibration, if the object to be measured was significantly bigger or smaller than the block used for calibration, all the cameras and projectors had to be calibrated again to get accurate results.

Today, there are 3D scanners commercially available with accuracies from 50-200 μm and scan speeds up to 60,000 points/s (Headus, 2003). However, these systems need specialized hardware and the object needs to be scanned several times when the object surface is uneven, making them unsuitable for industrial on-line inspection.

One 3D scanner designed by Geng (1997) deserves special attention. In the scanner, a known spatially distributed wavelength spectrum (from 420 μm to 650 μm) is used. To generate the continuous spectrum, a white light source (containing all visible wavelengths) is projected through a linear wavelength filter (LWF) is used. The LWF filter produces a rainbow-like spectrum pattern, where the light wavelength $\lambda$ passing through a particular position of the filter is a linear function of *d* as shown in Figure 1.

If the starting wavelength ($\lambda_b$), ending wavelength ($\lambda_e$) and effective length of filter (L) are known, then

$$\lambda = \lambda_b + \frac{\lambda_e - \lambda_b}{L} d , \tag{1}$$

where $\lambda$ is the light wavelength passing through a particular position of the LWF, and d is the displacement of that position from blue edge of the filter glass.

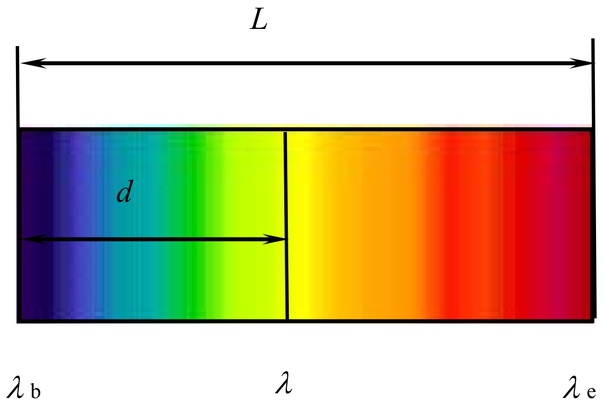

Figure 1. The LWF filter used by Geng (1997) for rainbow pattern generation.

Because the whole scanning area can be covered by the light spectrum, no moving parts are needed in the system, and the video scanning rates can be archived. Theoretically, the resolution of the obtained 3D image is infinity because the

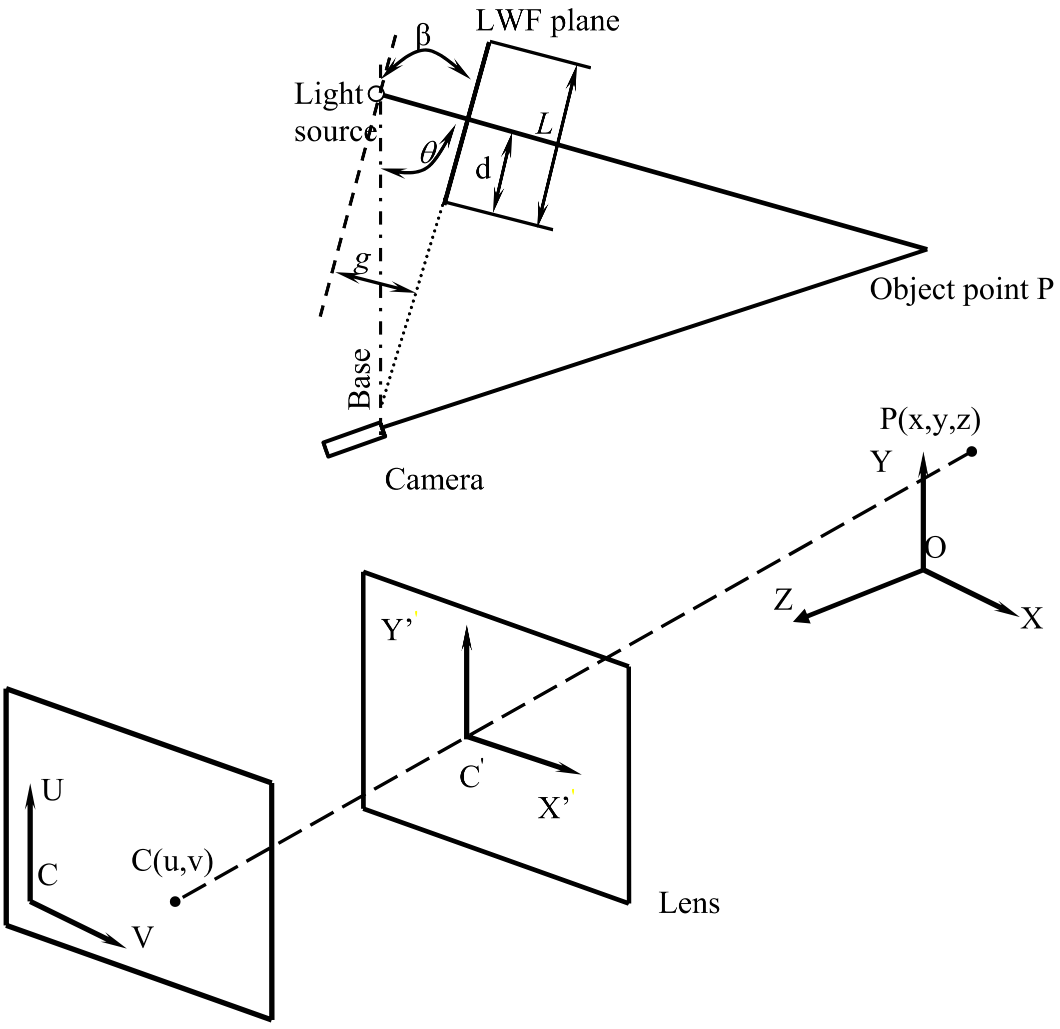

Figure 2. Illustration of Geng's scanner.

wavelength of the projected spectrum is continuous in space. It is only limited by the camera resolution.

The principle of the scanner is illustrated in Figure 2. First, from the spectrum data captured by the camera, the distance *d* can be calculated based on Equation 1.

Because the distance $g$ and angle $\beta$ between the light source and LWF are already known, the equation becomes

$$\theta = \beta - \tan^{-1}\frac{L/2-d}{g}, \tag{2}$$

Suppose the focal length of the camera is *f*, the position of the object image in the image plane is *(u,v)*, then the space coordinates of that point can be calculated by Equation 3

$$x = \frac{b}{f \cdot ctg\theta - u} \cdot u, \tag{3a}$$
$$y = \frac{b}{f \cdot ctg\theta - u} \cdot v, \tag{3b}$$
$$z = \frac{b}{f \cdot ctg\theta - u} \cdot f, \tag{3c}$$

where, b is the baseline distance between the light source and sensor center, and x, y and z are actual coordinates.

However, the visible light spectrum information is usually used in the scanner, and the surface color of the object has to be considered (Caspi, et al., 1998). To overcome this problem, Geng (1997) suggested capturing images twice, with one image captured as the reference without the light pattern. Although it solves the problem when the object is static, it introduces error when the background changes and objective moves, as is the case with on-line processing.

## 2.4 Encountered Problems

Different objects have different physical characteristics and the techniques used to collect the depth information from each object may be different from each other. Designing a range image system may lead to difficulties noted below.

### 2.4.1 System Error and Calibration

There were four error sources involved in range imaging calibrations as given by Hashemi, et al. (1994): 1) Statistical errors caused by device noise; 2) drift errors caused by reference wave phase shift; 3) alignment errors caused by the dependence of the measurement offset upon the width, position, and intensity of the returned beam, and 4) slope error caused by an inaccuracy in the calculation of the rangefinder's characteristic length that was decided by the modulation frequency and group refractive index of the air. Although this system was designed based on the time-of-flight, it is still a good reference for range system error analyses based on the triangulation method.

When a camera is used in the range system, the system inevitably has geometric distortion. Therefore, the data collected by the system exhibits a high degree of nonlinearity. Bumbaca, et al. (1986) thought this nonlinearity, in the form of interrelated range and geometric distortions could be corrected in real-time without imposing any severe restrictions on the type of distortion laws to which the particular sensor was adhered. If the object is sampled in the x- and y- directions, N and M times respectively, there are NM values of I and P with I representing uncorrected intensity and P representing range. The P is a highly nonlinear function of (x,y) position and corrected range z. The author proposed using a lookup table based on (x,y,P,z) to correct this nonlinearity and to simplify the lookup table by eliminating z when the object surface is in a constant-height plane. Thus the geometric error of the optics device is corrected. However, it is not always easy to get the reference points to calculate the look-up table in applications.

Manthey, et al. (1994) presented a calibration method which used an active laser triangulation system. First the system was calibrated by positioning a flat plane at a minimum of three different positions in the depth of the field. These positions were chosen to span the entire depth of the field in order to compensate for geometrical nonlinearities in the system caused by optics. Then, a standard sphere with a known diameter was used to calibrate the system. The sphere was placed on a positioned system with linear accuracy of 6.0 μm in both the x- and y-directions. After getting the reference data, a least-square regression algorithm was used to obtain the system calibration parameters. When using a 75 mm lens, the reported resolution was 0.1250 by 0.0006 by 0.0171 mm in the x, y and depth directions and the accuracy was 0.1262 mm of the measured depth.

### 2.4.2 Image Pixel Registration

To obtain 3D information of an object with a complicated surface shape, optical and electrical devices are used in range imaging systems. Accurate image registration is required to integrate data from different sensors. Different registration methods should be used for different applications.

Zhou, et al. (2000) described a real-time image system to make continuous geometric measurements of 3D surfaces. In this system, two cameras and thirty-three laser beams were used to improve the resolution and accuracy of the object measured. The object was placed on a rotatable table. By over-sampling the object surface and using a Gaussian interpolation and re-sampling operation to smooth the combined data, the images taken by the two cameras were integrated together and the accuracy of the surface depth information was improved while maintaining a given spatial resolution.

### 2.4.3 Laser Scattering on Biomaterials

In biological applications, the most serious problem occurs when light scattering takes place on the surface or inside of the object. Scattering is a common phenomenon when the light wavelength is comparable with the object surface roughness or the object consists of scatters due to different refractive indices. Because chicken fillets are of a relatively loose structured material, laser light easily penetrates into the meat, and scattering thus occurs both at and under the surface. Laser light scattered under the surface is reflected back to the surface and blurs the laser line sharpness. Thus, this reflection degrades the image quality (Posudin, 1998, Popp, et al., 2003).

### 2.4.4 Speckle Noise

Speckle noise is shown to constitute a fundamental limit to laser range finders based on triangulation (Baribeau and Rioux, 1991b). The speckle originates from object surface scattering. When the surface is rough, the wave summation cancels each other out, leading to dark speckles in the image, while in the other portion of the image the waves reinforce each other, leading to bright speckles. From this theory, the error caused by speckle is related to the wavelength, the angle between the camera and laser, and the diameter of the camera lens. A method used to reduce the speckle is to average the image.

## 2.5 Meat Characteristics

Meat characteristics are important to the optical imaging because the meat structure and composition are directly related to light scattering and X-ray absorption. Meat generally contains approximately 75 percent water, 19 percent protein, 3.5 percent soluble, non-protein substances, and 2.5 percent fat (Lawrie, 1991). The percentage of water in meat varies with the type of muscle, the kind of meat, the season of the year, and the pH of the meat. Fat in meats is found both between muscles and within muscles. In both locations, fat contributes to the overall flavor and juiciness of meats. Meat contains muscle, connective tissue, fat, and other biological materials. The major component of poultry breast meat is skeletal muscle. Skeletal muscle is a syncytium of multinucleated muscle fibers which originate from single nucleated mesodermal cells. The whole muscle is surrounded by a sheath of connective tissue known as the epimysium. Inside the epimysium, another layer of membranes of connective tissue called perimysium penetrate into the muscle and separate the muscle fibers into smaller fiber bundles. The large blood vessels and nerves are also included in the perimysium. Under the perimysium, each individual muscle fiber is wrapped by a fine connective tissue called the endomysium. The wrapped fibers are rod-like contractile myofibrils, or muscle cells, which are about one millimeter in diameter. Furthermore, between the collagenous fibers of the endomysium and the muscle cell membrane, there is another microstructure referred to as the basement membrane, or sarcolemma complex, which connects them together (Richardson and Mead, 1999). The cross section of a typical skeletal muscle is illustrated below in Figure 3.

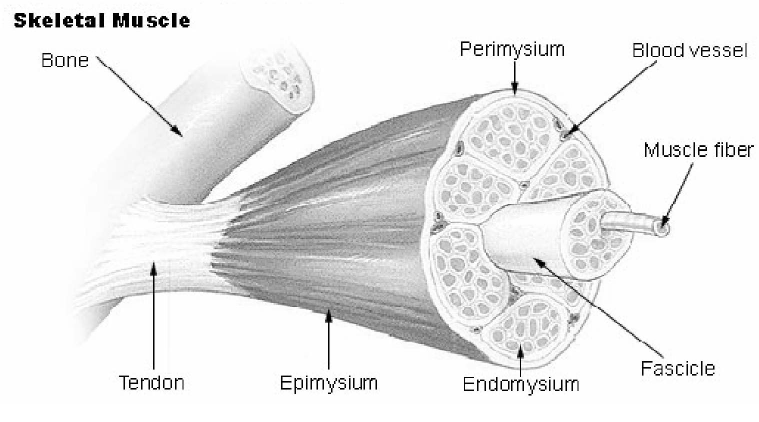

Figure 3. Illustration of skeletal muscle structure (NCI, 2003).

Chicken skeletal muscle fibers, similarly to mammalian muscle fibers, can be divided into three different types of twitch muscle fibers: type 1, type 2a, and type 2b. Type 1 (oxidative) muscle fibers are efficient and economical for slow repetitive movements. Type 2b (fast, glycolytic) muscle fibers are adapted for a high-power output over a short period. Type 2a (fast, oxidative, glycolytic), on the other hand, are mainly used to generate high-power output over a longer period of time. The type 1 fibers are particularly abundant in postural muscle which is activated during standing, walking and running (Lawrie, 1991).

The chicken breast meat being investigated is mainly composed of the pectoralis major whose fibers are exclusively the fast, glycolytic (2b) type. During the maturation of chickens, the composition of muscle is continuously changing as the age, nutrition and living environments change (Touraille, et al.,1981).

### 2.5.1 Muscle Cell Structure

A normal single nucleated cell is a very complex structure. As illustrated in Figure 3, it includes several components. There is cytoplasm, a nucleus, proteins, chromatin, and mitochondria. There are also other cell components such as endoplasmic reticulum(ER), lysomes, and peroxisomes that exist in the cell. The component sizes and refraction indexes determine the scattering properties of the cell. The total volume of each component related to the entire cell volume depends on many factors, but, typically, the cytoplasm occupies 50-80%, nucleus 5-10%, mitochondria 5-15%, and other organelles 1-10% of the cell volume. (Alberts, et al., 2002).

Table 1. Size and refraction index of some cell components (Dunn, 1997)

| Cell component | Size (μm) | Cell component | Refractive index |
|---|---|---|---|
| cytoplasm | 10-30 | cytoplasm | 1.38 |
| mitochondria | 0.5-1.5 | mitochondria | 1.40 |
| ER | 0.2-1 | lipid | 1.48 |
| nucleus | 3-10 | nucleus | 1.35 |
| peroxisomes | 0.2-0.5 | protein | 1.50 |
| lysomes | 0.2-0.5 | melanin | 1.7 |

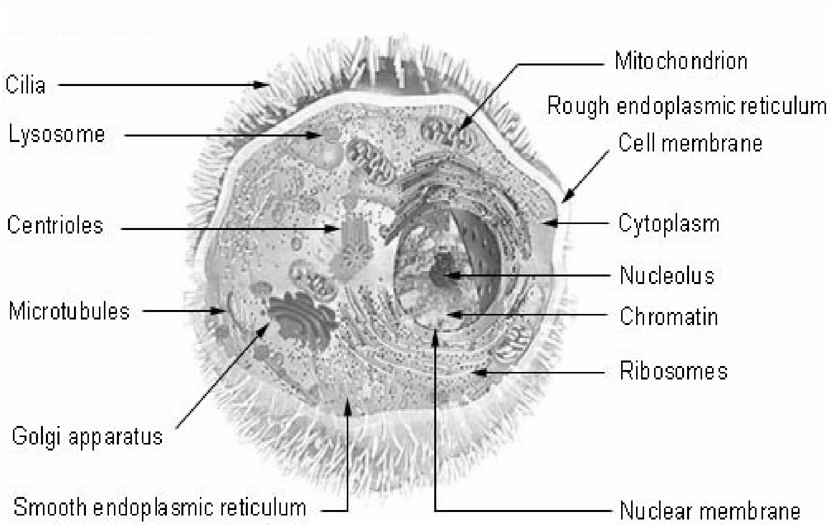

Figure 4. Illustration of a common single nucleated cell (Michael, 2003).

Although the muscle fibers (muscle cells) have the same structure as the common single nucleated cells, they are different from normal cells in their shape and the number of nuclei that exist in the cell. Pectoralis major fibers (poultry breast meat cells) are long cylindrical multinucleated cells which generally stretch the length of the muscle belly. The muscle cells (fibers) are different from common cells due to the shape and number of nuclei (Lawrie, 1991).

# Chapter 3

# OBJECTIVES

The overall objective of this research was to develop a laser range imaging subsystem as one part of a combined X-ray and laser imaging system for sensitive detection of bone fragments and hazardous materials in de-boned poultry meat. Specifically, the objectives of this research were:

1) To calculate sub-pixel profiles from scattered images;
2) To geometrically calibrate laser and X-ray imaging systems;
3) To map the laser range image to pseudo-X-ray image for further processing; and
4) To implement the laser range system for real-time on-line application.

The development of the system included the basic theory, experimental verification, and system implementation.

# Chapter 4

# EQUIPMENT AND SYSTEM OVERVIEW

## 4.1 Dual X-ray and Laser Imaging System Setup

The overall imaging detection system was designed and built to capture both X-ray and laser 3D images simultaneously at high speeds. It included two imaging subsystems: an X-ray imaging subsystem and a laser 3D imaging subsystem. Both subsystems were integrated in one machine. Figure 5 illustrates the overall configuration of the integrated X-ray and laser imaging system. The equipment of the system is shown in Figure 6.

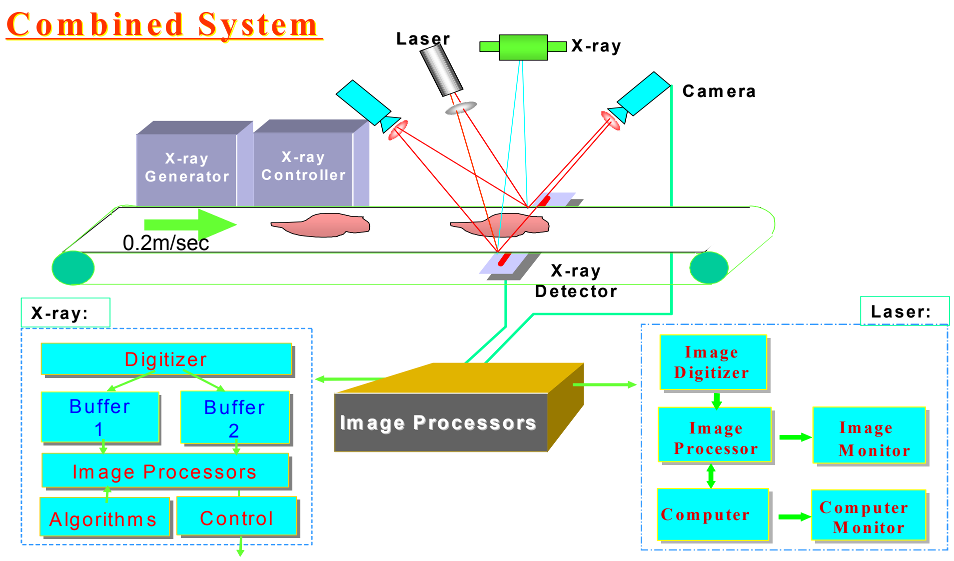

Figure 5. Illustration of the X-ray and laser integrated system.

In Figures 5 and 6, the range imaging system consisted of two laser projectors and two CCD cameras with C-mount lenses (16mm, Fujinon Inc. Woodstock, GA). The cameras were high speed Pulnix TM-6703 (Pulnix America, Inc. Sunnyvale, CA) monochromatic CCD cameras. Monochromic CCD cameras were selected because of their lower cost and higher signal-to-noise ratio. The cameras were placed on each side of the structured laser pattern generator to reduce the influence of possible occlusion caused by the curvature of the poultry fillet. These two cameras were connected to one Matrox Genesis LC board (Matrox Electronics Systems Ltd., Quebec, Canada). The grabber was plugged into a Pentium IV 1.4GHz computer. The cameras and laser structured light generator were mounted on a fixed frame in the X-ray chamber. Objects to be scanned were placed on the conveyor that traveled under the X-ray and laser lights. The laser line generators used in this system were class 3 lasers with wavelength of 635nm and power of 5 mW, (Lasiris SNF501L, Stockyale, Montreal, Canada). Red diode lasers were selected because of their low price and small size. The lasers produced a non-Gaussian, evenly illuminated line of laser light such that the laser beam did not have any light intensity variations or fading toward the ends of the beam. When the laser pattern struck the object, the object's profile was seen by the cameras. To adjust the laser line strength reflected into the camera and avoid the saturation of the object profiles' image, a polarizer was placed in front of the laser pattern generator.

To reduce occlusion caused by the uneven and random surface shape, two cameras were set up facing each other, making an angle with respect to the conveyor belt. The angle was determined by the accuracy requirement, view of the field, and space availability in the chamber. Both cameras were calibrated and attached to the stationary frame. The distance between the two cameras and the distance from the camera plane to the object plane were decided by the angle. To synchronize the cameras, one of the cameras was set as master and the other one as slave, where the master camera sent the synchronization signal to the slave camera. Also, to reduce the image processing time, both cameras were connected to a single image board through two signal channels. An encoder mounted on the conveyor belt shaft was used to provide the signal to synchronize the master camera and the conveyor. Related details about the synchronization and configurations can be found in Tao (1996, 1999). The laser 3D subsystem was entirely hosted in an X-ray chamber. To correctly align images and reduce the mismatch of the two images by possible slipping of the conveyor, the laser beam was arranged to stay as close to the X-ray beam as possible.

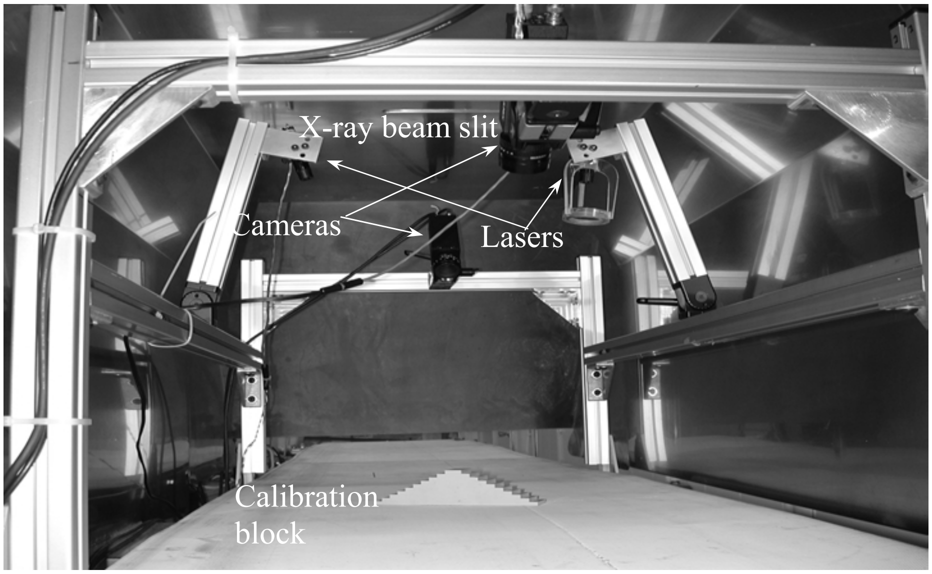

Figure 6. Illustration of dual system setup.

The images were grabbed and saved in the computer using software written with Microsoft Visual C/C++ (Microsoft Corp., Redmond, Wash.). The software utilized a Matrox (Matrox Electronics Systems Ltd., Quebec, Canada) library to interface with the frame grabber. The software was capable of simultaneously grabbing images from the X-ray system and computing the 3D laser images from the two cameras. Laser images were grabbed and calculated with eight bits resolution. The 3D laser image and X-ray image were fully synchronized by an encoder pulse. All the image grabbing and processing was done on-line. The operating system used in this application was Windows 2000 (Microsoft Corp. Redmond, Washington).

## 4.2 Three Dimensional Laser Range Imaging

In this study, a laser range imager using one structured light beam plane (two beams in the same plane) was used as illustrated in Figure 7. Two diode laser pattern generators were used to project a laser light line onto the chicken fillet. The thickness variation of the sample was registered by the shift in the stripe lines. The geometry of the structured light system is shown in Figure 8. If the laser beam is perpendicular to the conveyor, and the angle between the camera z axis and the conveyor surface is $\theta_z$, the laser beam illuminates the object at the coordinates

$$x_0 = x_s - (z_0 - z_s)\tan\theta_z, \tag{4}$$

$$x_i = \frac{f}{z_0}x_0 = \frac{f}{z_0}(x_s + z_s\tan\theta_z) - f\tan\theta_z, \tag{5}$$

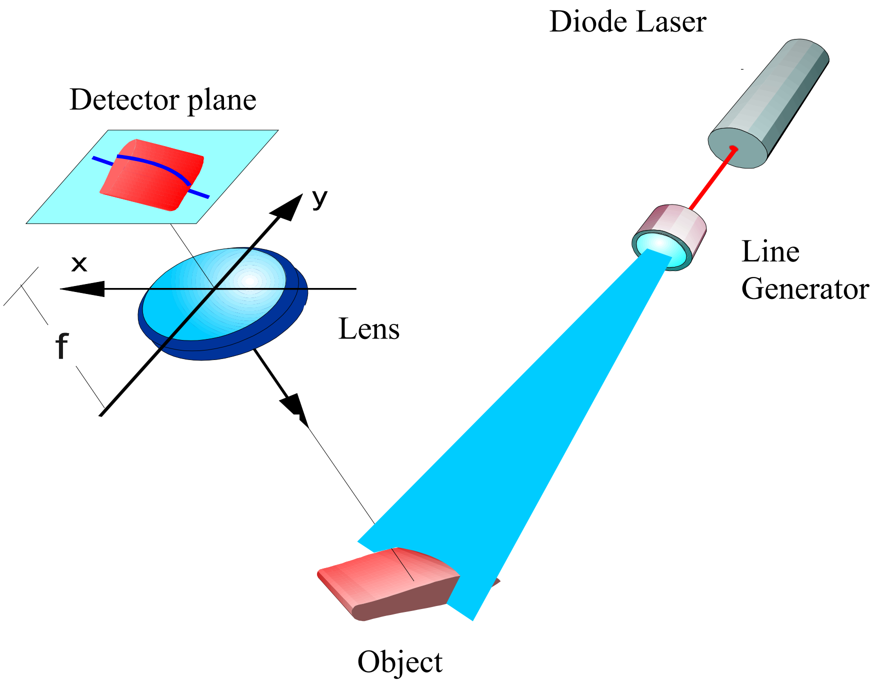

Figure 7. Schematic of a laser-based structured light system for surface shape determination.

where f is the distance between the receiving lens and detector, which is equal to the focal length of the camera lens. If this image point is compared to that produced by an point at a distance $z_{ref}$, the displacements of the image are given by

$$\Delta x = f(x_s + z_s \tan\theta_z)\left(\frac{1}{z_0} - \frac{1}{z_{ref}}\right), \tag{6}$$

The x displacement can be used to calculate the object distance:

$$z_0 = \frac{z_{ref}}{1 + \Delta x \cdot z_{ref} / f(x_s + z_s \tan\theta_z)}, \tag{7}$$

The thickness of the meat can be calculated by:

$$T = \frac{z_o - z_{ref}}{\cos\theta_z}, \tag{8}$$

where T is the thickness of the meat at that point.

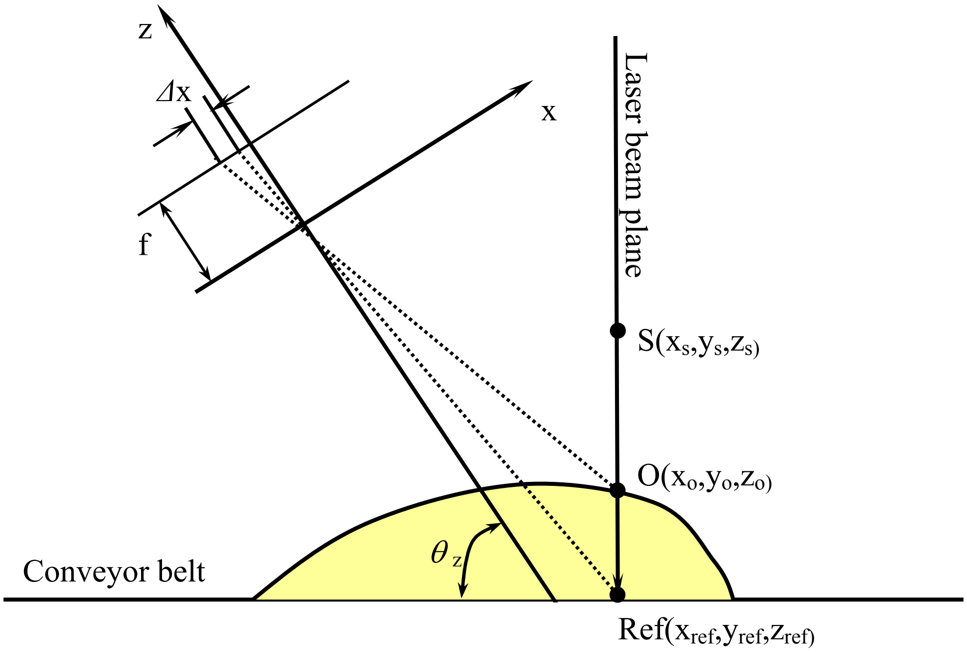

Figure 8. Triangulation geometry in a structured-light system.

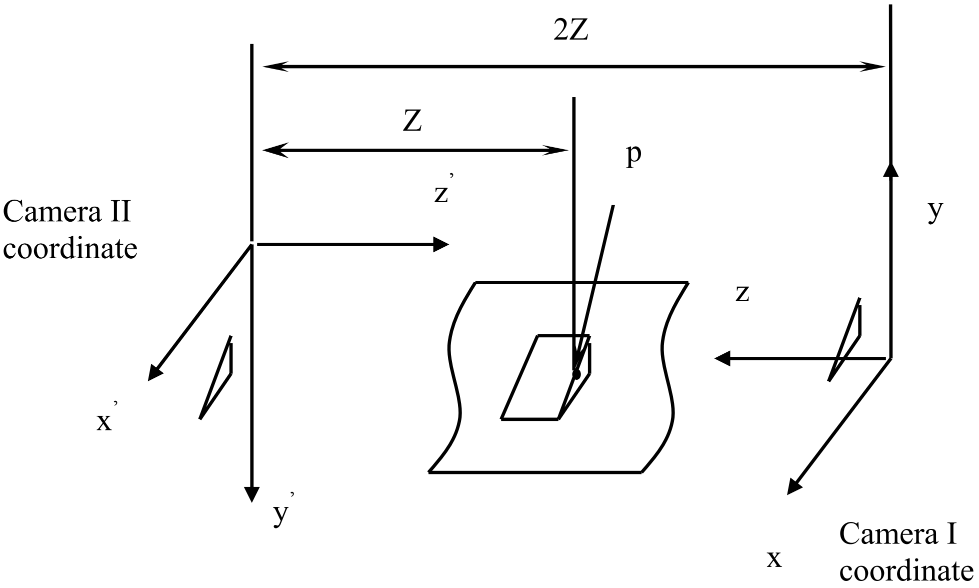

Figure 9. Sketch of two camera coordinates.

As illustrated in Figure 9, two cameras capture laser line images without occlusion. When two cameras were calibrated, the pictures in each camera mirror each other as shown in Figure 9. In fact, the coordinates of the second camera are translated 2Z distance from the coordinates of the first camera and are rotated $180^0$ in the first camera coordinate x-axis. Thus,

$$T_{c2} = T_z \times T_t \times T_{c1}, \tag{9}$$

where

$$T_t = \left\{\begin{matrix} 1 & 0 & 0 & 0 \\ 0 & 1 & 0 & 0 \\ 0 & 0 & 1 & -2z_{c1} \\ 0 & 0 & 0 & 1 \end{matrix}\right\}, \tag{10}$$

$$T_z = \left\{\begin{matrix} 1 & 0 & 0 & 0 \\ 0 & -1 & 0 & 0 \\ 0 & 0 & -1 & 0 \\ 0 & 0 & 0 & 1 \end{matrix}\right\}, \tag{11}$$

Suppose $T_{c1} = \begin{bmatrix} x_{c1} & y_{c1} & z_{c1} & 1 \end{bmatrix}^{\mathrm{T}}$, then $T_{c2} = \begin{bmatrix} x_{c1} & -y_{c1} & z_{c1} & 1 \end{bmatrix}^{\mathrm{T}}$.

The thickness image was obtained by moving the object and calculating each pixel shift, $z_0$, of each stripe continuously. The lateral resolution was the distance, d, that the conveyor belt traveled between the two encoder pulses. The d was set at 0.8 mm. The horizontal resolution was determined by the pixel resolution, typically being 0.7 mm/pixel (field of view 16" x 25.4 mm / 600 effective pixels of CCD camera). The depth resolution was 0.7 mm/pixel (field of view 6" x 25.4 mm / 200 pixels of CCD camera).

To test the effect of using two cameras, a plastic doll face with similar geometrical complexity to a poultry fillet was scanned. Figure 10(b) is the original object. Due to object curvature, the view to center part of the face was blocked in one direction. Figure 10(a) clearly shows the occlusion effect. However, the center part of the object was not blocked if viewed from another side of the object, as shown in Figure 10(c). If two cameras were placed looking in opposite directions, the occlusions were removed in this case. Figures 10(d) and (e) are reconstructed 3D images.

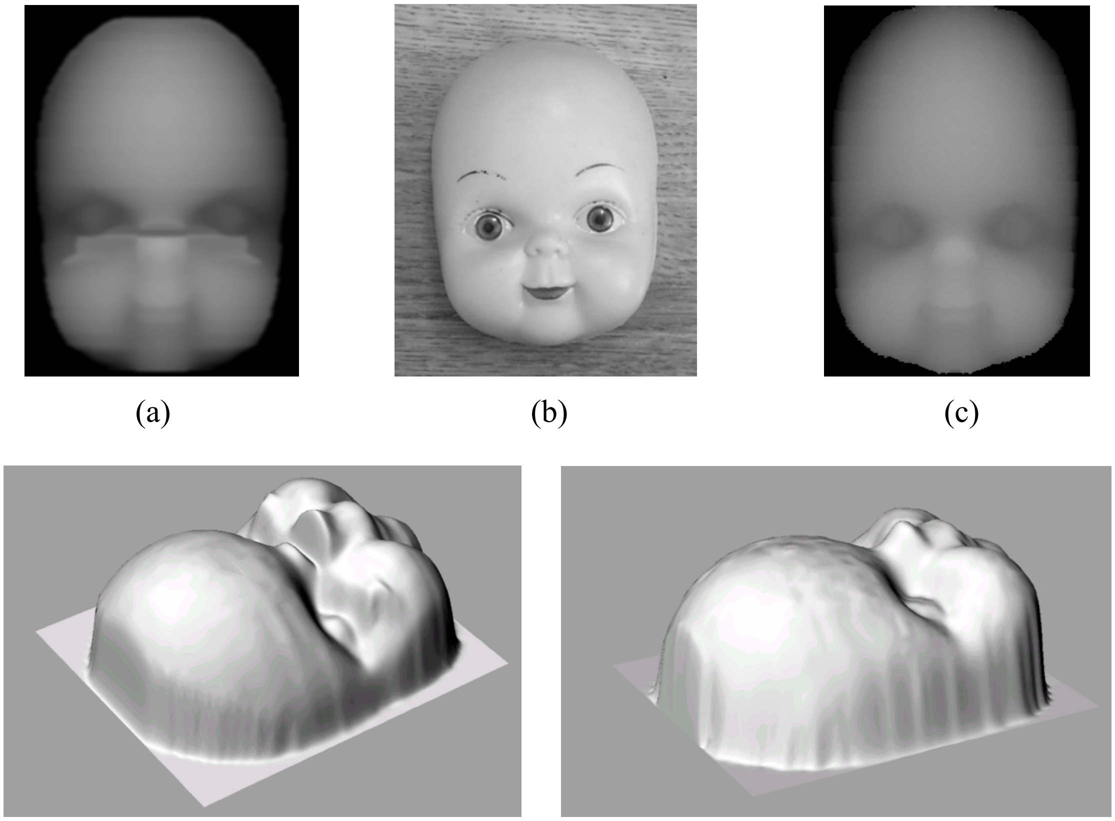

(a) (b) (c)

(d) (e)

Figure 10. Example images to illustrate the effect of using two cameras. (a) Range image captured with one camera, (b) doll face, (c) range image captured with two cameras, (d) picture of (a) after rendering, and (e) picture of (c) after rendering.

# Chapter 5

# SUBPIXEL ACCURACY CALCULATION OF SCATTERED LASER PROFILE

## 5.1 Introduction

In order to develop a chicken bone fragment detection system, a laser range imager was developed to be used in conjunction with the X-ray imaging. The range imager was designed based on the triangulation method. A laser pattern was projected onto the surface of the chicken fillet to obtain information regarding the depth of the meat. Because the laser profile had a certain width that occupied several pixels in the image, image processing was needed to accurately obtain the center of the profile. There were image processing methods that addressed this issue in the literature. Huertas (1986) used a complex Laplacian-Gaussian mask to obtain the profile center with sub-pixel accuracy. Valkenburg, et al. (1994) gave detailed descriptions of a centroid algorithm using a restricted polynomial model and Gaussian reconstruction. Similarly, Shortis, et al. (1994) presented a centroid algorithm with sub-pixel methods such as ellipse fitting. The performances of various methods were also compared by Shortis. Alexander and Ng (1991) presented an algorithm to eliminate systematic error in centroid estimation. Fillard (1992) examined the method presented by Alexander and Ng (1991) and introduced Fourier phase shift analysis to eliminate the error that existed in the depth calculation.

The laser profile formed on the object surface needed to be thin, clear, and free of noise. However, the center of the profile detected by the methods mentioned above did not generate an accurate result when the profile was corrupted by noise. The most common causes of noise were: 1) Laser speckling if the surface roughness was comparable to the incident coherent light wavelength (Baribeau and Rioux, 1991a, and 1991b); 2) The variation of object surface reflection; and 3) light scattering (Kim and Lin, 1998).

When coherent light strikes an object with a rough surface, reflected light is typically superimposed on incident or other reflected light. If the phases of two light sources are opposite, they cancel each other. Speckles on the surface of the object are formed where phases alternately cancel and reinforce each others. In speckle-corrupted images, Baribeau and Rioux (1991a) analyzed the influence of laser speckle on line image centroid identification and derived an analytical expression for centroid fluctuation. It was concluded that applying a linear filter to the speckle corrupted image did not improve the image quality. In another paper, Baribeau and Rioux (1991b) suggested superimposing uncorrelated corrupted gray-scale images to improve the image quality. However, this method could not be used in on-line applications.

In biological applications, the most serious problem occurs when light scattering takes place on the surface or inside the object. Light scattering is a very complicated phenomenon (Chu, 1974). It occurs when light passes through a medium that contains fluctuations in the refractive index (n). Fluctuations can be caused by discrete particles or more continuous variations in n. Scattering is different depending on the ratio of the incident light wavelength to the size of the particles in the media. When the wavelength is much larger than the media particles, Rayleigh scattering occurs. In this case, the light scatters in all directions (Posudin, 1998). Because chicken fillets are of a relatively loose structured material, laser light easily penetrates into the meat, and scattering thus occurs both at and under the surface. Laser light scattered under the surface is reflected back to the surface and blurs the laser line sharpness. Thus, this reflection degrades the image quality (Popp, et al., 2003).

To describe the laser light pattern reflected into the cameras, the Bidirectional Reflectance Distribution Function (BRDF) was used (Cohen and Wallace, 1993). BRDF gives the reflectance of a target as a function of illumination geometry and viewing geometry. BRDF was broadly used in areas such as computer graphics (Cook and Torrance, 1981) and remote sensing (Gao, et al., 2002).

## 5.2 Objectives

In this chapter, the study objective was to analyze laser scattering on poultry fillets and to develop methods to calculate the fillet depth from the scattered laser profile. Furthermore, methods used to calculate the laser profiles were compared and their performances were evaluated.

## 5.3 Materials and Methods

### 5.3.1 Image System Setup

The laser range image system used to capture the 3D images was built as one of the two subsystems for a bone fragment detection system. The laser 3D subsystem consisted of two high-speed Pulnix TM-6703 (Pulnix America, Inc. Sunnyvale, CA) monochromatic CCD cameras and two laser beam generators (635nm, Lasiris SNF501L, Stockyale, Montreal, Canada). The cameras were equipped with C-mount lenses (16 mm, Fujinon Inc. Woodstock, GA). The cameras and laser pattern generators were mounted on a frame that was firmly fastened in the stainless steel X-ray chamber. The laser patterns from the two generators were manually adjusted to be in the same plane. The pattern generated by the laser was a line with its strength evenly distributed along the line length direction with a Gaussian profile in the cross section of the profile. The width of the laser line was about 1.75 mm when the laser was 1.5 m away from the object. Two cameras were used, one on each side of the structured laser pattern generator to reduce the influence of possible occlusion caused by curvature of the poultry fillet. The angle between the camera view plane and laser pattern plane was approximately $45^0$. The cameras were connected to a Matrox Genesis LC board (Matrox Electronics Systems Ltd., Quebec, Canada) and they were triggered by the same encoder trigger signal. The image grabber was plugged into a Pentium IV computer.

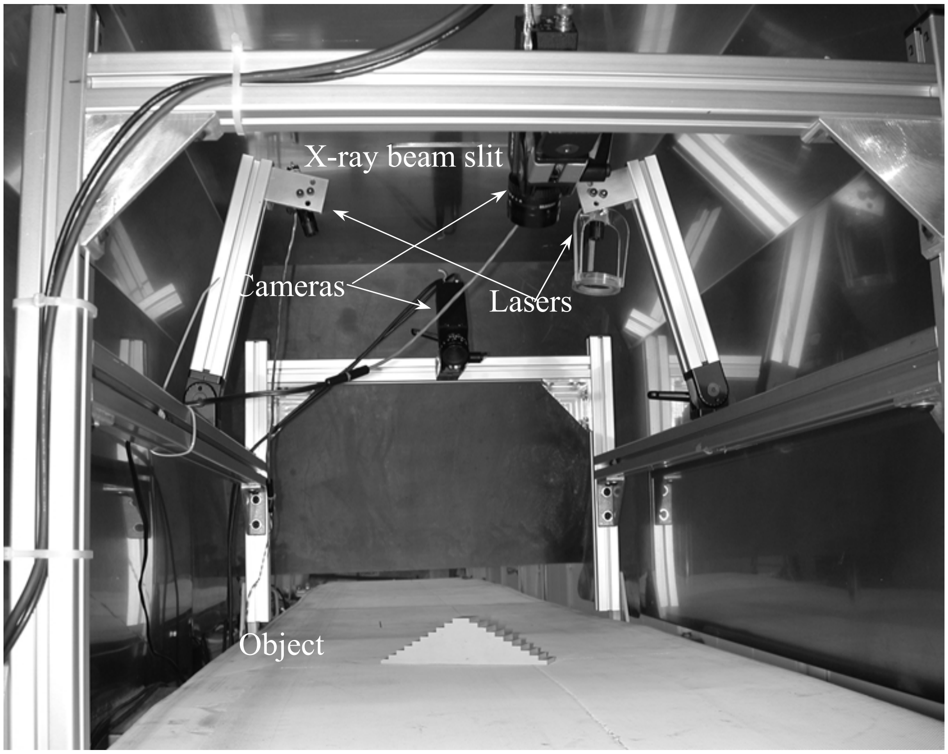

Figure 11. The inside view of the image system setup.

### 5.3.2 Laser Profile Analysis

In the laser range imaging system, the pattern generated by the laser pattern generator was a straight line with a bell shaped symmetrical cross section. The line was composed of continuously connected points. So, if every point's position was computed, the whole cross-section profile could be recovered. At the same time, a 2D line problem was changed to a 1D point problem. A line defined by $f(x)$ was modeled by continuously connected points represented by a function $I(x)$, convoluted over the whole image:

$$f(x) = I(x) \otimes h(x) + n(x), \tag{12}$$

where *h(x)* was the impulse response of system, *n(x)* was the noise added to the original signal, and ⊗ represents convolution. Ideally, *I(x)* was expected to be a symmetric Gaussian distribution (Posudin, 1998)

$$I(x) = I_0 \frac{1}{\delta\sqrt{2\pi}} e^{-(x-\mu)^2/(2\delta^2)}, \tag{13}$$

where $I(x)dx/I_0$ gave the probability that a variable with a Gaussian distribution took on a value in the range of (*x, x+dx*). $\mu$ was the mean value and $\delta$ was the standard deviation. $I_0$ was the total incident intensity.

However, because of scattering and absorption of the light energy, the reflected light strength is

$$I_R(x) = (1-\xi)I_0 \frac{1}{\delta\sqrt{2\pi}} e^{-(x-\mu)^2/(2\delta^2)} + s(x), \tag{14}$$

where $\xi$ is an index used to represent the energy lost by absorption and scattering. The function *s(x)* is scattered light. The absorbed energy changes to heat that is not detected by the camera.

Suppose that the object surface is flat and that the incident light shoots straight to the object, then part of the incident laser light is reflected back in the direction perpendicular to the object surface. However, scattered laser light is reflected in every direction as illustrated by Figure 12. The scattered laser light is seen to be symmetrical about the light incident plane. Although both reflected light directions are different, their addition is still symmetrical. So when the camera lens axis is in the same plane as the laser beam, a centroid method can be used to find the peak of the profile, and based on that point it is possible to find the height of the object.

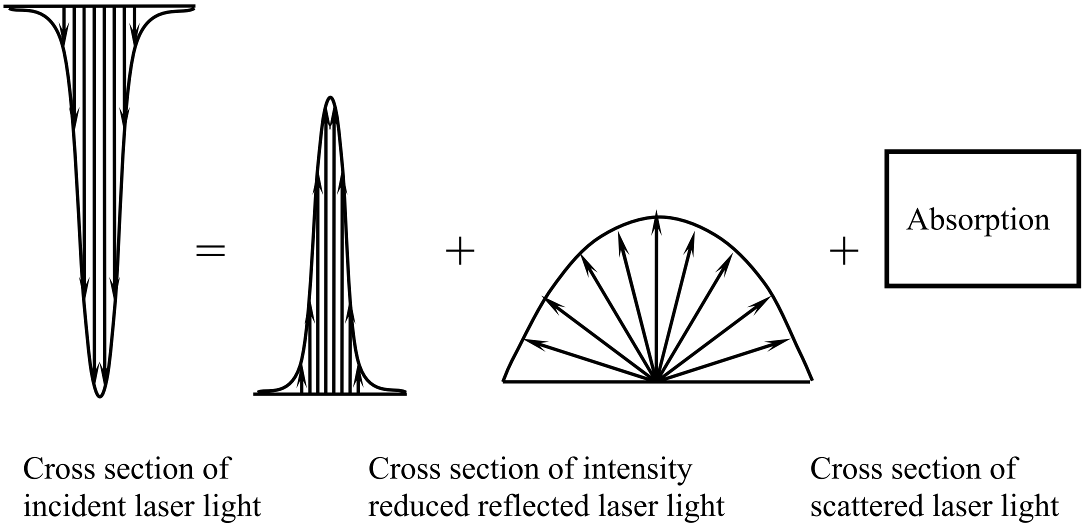

Figure 12. Illustration of reflected signal. The scattered laser light is reflected in every direction (Posudin, 1998).

### 5.3.3 Laser Profile Calculation Method

Centroid methods are broadly used to get sub-pixel accuracy. It can be shown that if there is no quantification error or noise, centroid methods are the exact representation of the edge points. All centroid methods bear a similar form,

$$C(x,y) = \frac{\sum_{c \in R} c(x,y) \times g(x,y)}{\sum_{q \in R} q(x,y)}, \tag{15}$$

where *c(x,y)* and *q(x,y)* are functions of x- or y-coordinates, *g(x,y)* is the function of the intensity of the respective pixel, and *R* is the area where the centroid method is applied.

Frequently used centroid methods include median, squared median and binary centroid methods. When using the median method, *g(x,y)* represents the image intensity of the corresponding point, and *c(x,y)* and *q(x,y)* are both x- and y-coordinates of points whose intensity is the median value of all the points in area *R*. In some cases, when considerable noise exists in the image, the squared median method will increase the signal to noise ratio (SNR), thus increasing the accuracy of the detected edge. Here, *g(x,y)* is the squared intensity value of each point, and *c(x,y)* and *q(x,y)* still indicate the x- and y-coordinates of the points. Because the signals normally have a symmetrical bell curve (Posudin, 1998), the binary centroid method is also used to detect edge points. For the binary centroid method, the *g(x,y)* and *q(x,y)* in Equation 15 are set to one, and c(x,y) is the x- or y-coordinates of the points.

Another method used to find the peak of the line is based on the profile's derivatives. If the profile has the Gaussian shape, its first derivative is zero and the second derivative is maximum at the ridge point. Different directional masks are applied to the image by:

$$S = R \otimes M, \tag{16}$$

where *R* is a vector that represents a local region. *M* is the mask used to enhance the edge. *S* represents the resulting image, which is then processed to find the presence of the ridge point. $\otimes$ represents convolution.

If the angle between the camera's lens axis and the laser beam plane is not zero, the actual light received by the camera from the laser profile is different from the reflected light intensity and has the form (Cohen and Wallace, 1993)

$$CR(x) = f(\beta, \theta) \cdot I(x) \cdot \cos\theta , \tag{17}$$

where, CR(x) is the light intensity received by the camera, *f(β, θ)* is the Bi-directional Reflectance Distribution Function (BRDF) (Foley, et al., 1990) which is determined by the physical characteristics of the object, $\beta$ is the angle between the camera lens axis and horizontal plane, $\theta$ is the angle between light incident direction and the horizontal plane as illustrated in Figure 13, and *I(x)* is the incident laser light strength.

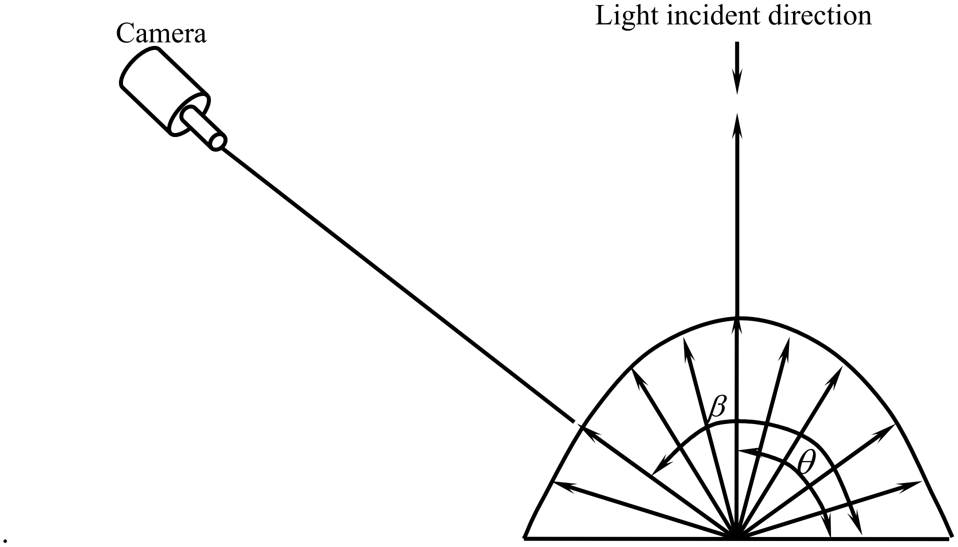

Figure 13. Illustration of camera setup and scattering cross section image.

When $\beta$ was not equal to $\theta$, because portions of the light were scattered in every direction, the image intensity distribution at the camera was different from its actual distribution. This is demonstrated in Figure 14. When the angles were equal to each other, the cross profile was symmetrical. In some portion of the laser profile, all the light is reflected back without major scattering. When the angles were different, such as shown in Figure 14(a), the cross profile was biased to one side of the image. For this reason, the calculated line location was shifted to one side of the image. Because the scattering function was very complicated, the exact shape of the scattering was not known, but the shift amount was constant when the scattering had the same pattern.

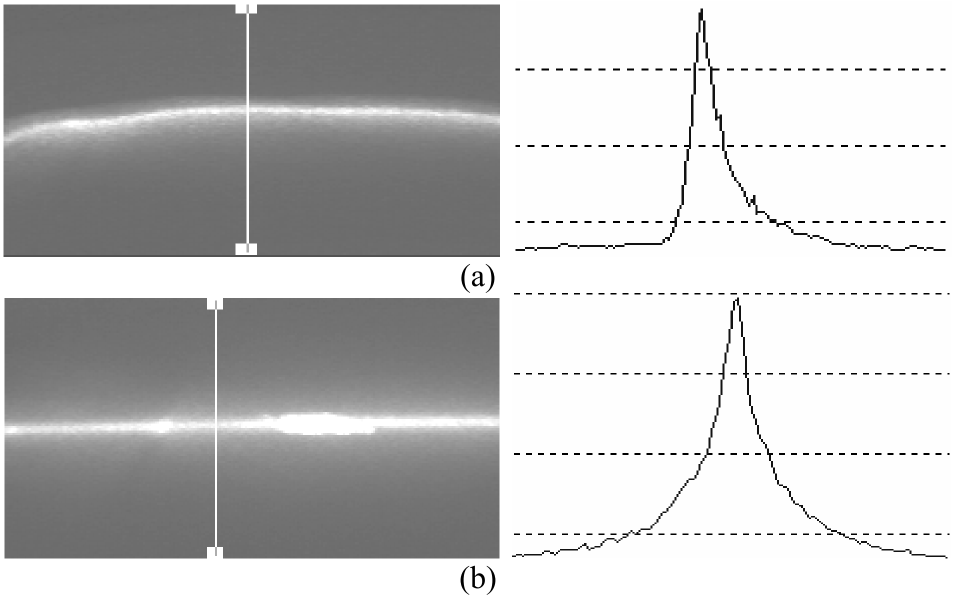

Figure 14. Illustration of effect of angle of the camera $\beta$. (a) The $\beta$-$\theta$ difference is 60 degree, and (b) the $\beta$-$\theta$ difference is approximately zero degree.

Because the scattered light only occupies a small portion of the total light energy, two methods modified from the centroid method were proposed to calculate the real profile center from the skewed image.

$$CI(x) = C(x) + \mathrm{K}1, \tag{18}$$

$$CI(x) = C(x) + \mathrm{K}2 \cdot \varphi, \tag{19}$$

where *CI(x)* is the center of the profile and *C(x)* is the centroid calculated by Equation 15. K1 and K2 are constants that represent the shift of the scatter. K1 and K2 can be experimentally computed. Because scattering at every point may not be the same, *φ,* a symmetrical index is used to modify K2 in the equation. It is expressed by

$$\varphi = \frac{\sum_{x<x(P)} s(x)}{\sum_{x>x(P)} s(x)}, \tag{20}$$

where x(*P)* represents the peak position of the profile. When *φ* is equal to one, the profile is symmetrical; otherwise, it is skewed to one side of the profile. Equation 18 is referred to as the shifted centroid method while Equation 19 is called the modified centroid method.

### 5.3.4 Reference Profile

Poultry meat is a viscoelastic material, making it difficult to produce a reference object with a specific size in order to calibrate the image detection method. To overcome this problem, a thin coating of paint was applied to the surface of the meat, making most of the laser light reflect back and reducing most scattering. Figure 15 demonstrates the difference between the images before and after the coating was applied.

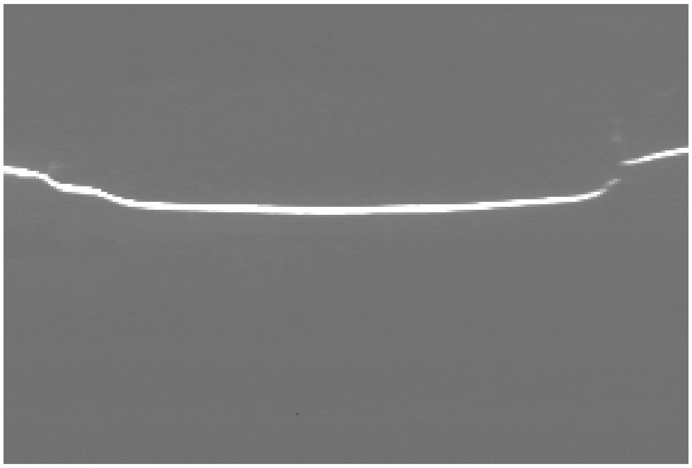

(a)

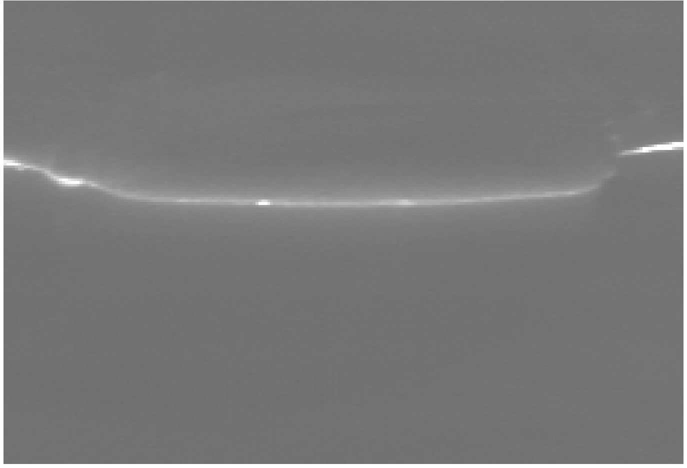

(b)

Figure 15. The comparison of image before and after the coating was applied. (a) Image with coating, and (b) image without coating.

Because scattering disappeared after applying the coating, the images taken with the coating were used as the reference to compare the results from the proposed method.

### 5.3.5 Laser Wavelength Selection

The laser is well known for its mono-chromaticity, coherence, directionality, and brightness. When a laser light is projected onto biological materials, light scattering inevitably results. Because the sizes of the cell components range in size from 0.2 to 1 μm (Alberts, et al., 2002) and the visible light wavelength falls between 400 nm and 700 nm, the light wavelength is almost on the same scale as the cell components. In this situation, Mie scattering (Chu, 1974) is the predominant scattering phenomenon (Dunn, 1997). Changing the laser light wavelength does not reduce scattering as long as the wavelength remains in the visible range. To verify this conclusion, two commercially available lasers, one red laser with wavelength of 635 nm, and the other a green laser with a wavelength of 532 nm, were used. Both laser lights were projected on the same location on the same objects. Figure 16 shows the scattered images.

Although the spectral response of the camera (Pulnix TM-6703) used peaks at 480 nm, the intensity of the red laser profile image is higher than that of the green laser profile. This shows that poultry meat absorbs more energy in the green than in the red wavelengths. The scattering of the green and red laser lights are almost the same as shown by the symmetrical indices. Considering that the green laser is far more expensive and bulkier than the red laser, the red laser was selected as the laser source.

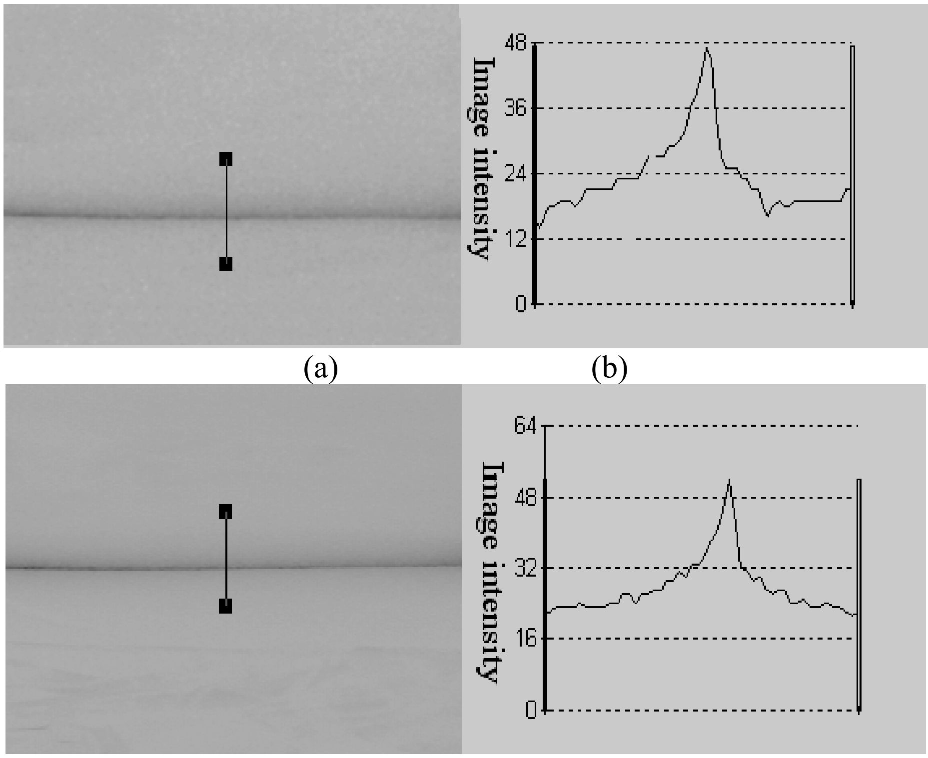

(a) (b)

(c) (d)

Figure 16. Cross section comparison of red laser and green laser profile. (a) Green laser profile, (b) green laser profile cross section, (c) red laser profile, and (d) red laser profile cross section

## 5.4 Results and Discussions

### 5.4.1 Symmetrical Assumption of Laser Profile

Biological materials are normally heterogeneous materials at the microscopic level, so scattering may not be symmetrical. Chicken breasts, which are mainly composed of skeletal muscle, have the structure shown in Figure 17.

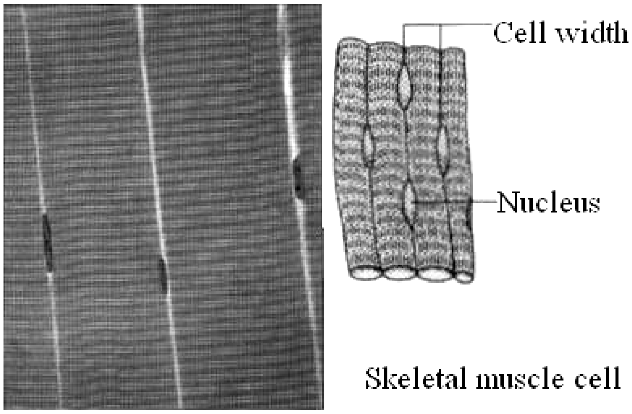

Figure 17. Illustration of poultry breast muscle (Chynoweth, 2003).

Skeletal muscle is different from cardiac and smooth muscles. It is symmetrical in the longitudinal direction except for the nucleus and tissues between the myofibril. It can be considered to be symmetrically arranged. To verify this assumption, a laser light was projected onto the surface of the poultry meat which was arranged in several directions. Then the shape of the scattered image was observed and the symmetrical index along the profile direction was calculated. Figure 18 clearly demonstrates that it was symmetrical. Therefore, the assumption that the scattered laser profile of the poultry breast meat is approximately symmetrical can be accepted.

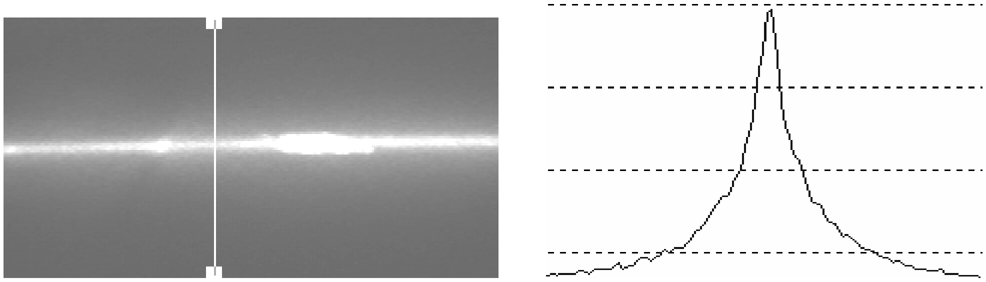

(a) (b)

Figure 18. Illustration of symmetrical profile. (a) Original image, and (b) cross section profile.

### 5.4.2 Determination of K1 and K2

The key step in the proposed method is to determine the constant value K1 and K2 in Equations 18 and 19. Twenty poultry fillets were randomly selected from a poultry processing facility. First, the fillets were scanned without applying the coating, then the coating was applied on the surface and the object was scanned again to get the reference profile To obtain both constants K1 and K2, a total of 80 sample profiles (40 scattered laser profiles and 40 reference profiles, 4 profiles from different locations in one sample fillet) were taken. Each profile was about 200 pixels long. Twenty scattered profiles were used to calculate the K1 and K2. Another twenty scattered profiles were used to evaluate the performance of proposed profile calculation methods. To calculate K1, the difference between corresponding points on the reference profiles and the scattered profiles were compared, and the mean differences were calculated and used as K1. To calculate K2, because $\varphi$ was not constant, an iteration method had to be adopted. Based on the sample profiles, the K1 value was .47 and the K2 value was 0.39.

### 5.4.3 Performance comparison of poultry profile calculation methods

To evaluate the performance of the proposed method, the proposed methods were applied to the twenty scattered profiles and their results were compared with the reference profile. In Figure 19(a), the profile obtained by the normal centroid method is compared with the reference profile. Due to the scattering influence, the whole profile was obviously shifted in one direction. If the image is shifted a distance K1 (pixels), as illustrated in Figure 19(b), the system error due to the scattering was eliminated. However, scattering acts as a low pass filter causing some detailed information to be lost (Figures 19 (a) and (b)). In Figure 19(c), the scattering effect was considered in the form of the symmetrical index, and the variation from the reference profile is decreased. This can be seen clearly in Figure 20.

To quantitatively compare the performance of these two methods, the deviation index is used

$$dev = \frac{\sum_{i=1,2,..n} |p_i - P_i|}{n}, \tag{21}$$

where $p_i$ is the calculated depth, $P_i$ is the depth of reference object depth, and $i$ is the index of the point. Numerical results appear in Table 2.

Table 2. Quantitative evaluation of modified centroid method and shifted centroid method (pixels*)

| | dev | Variance | Mean | Minum deviation | Maxum deviation |
|---|---|---|---|---|---|
| Modified centroid method | 0.2021 | 0.0671 | 0 | -0.8698 | 0.5411 |
| Shifted centroid method | 0.2219 | 0.0709 | 0 | -0.8400 | 0.7471 |

(*1 pixel = 0.7 mm x 0.7mm)

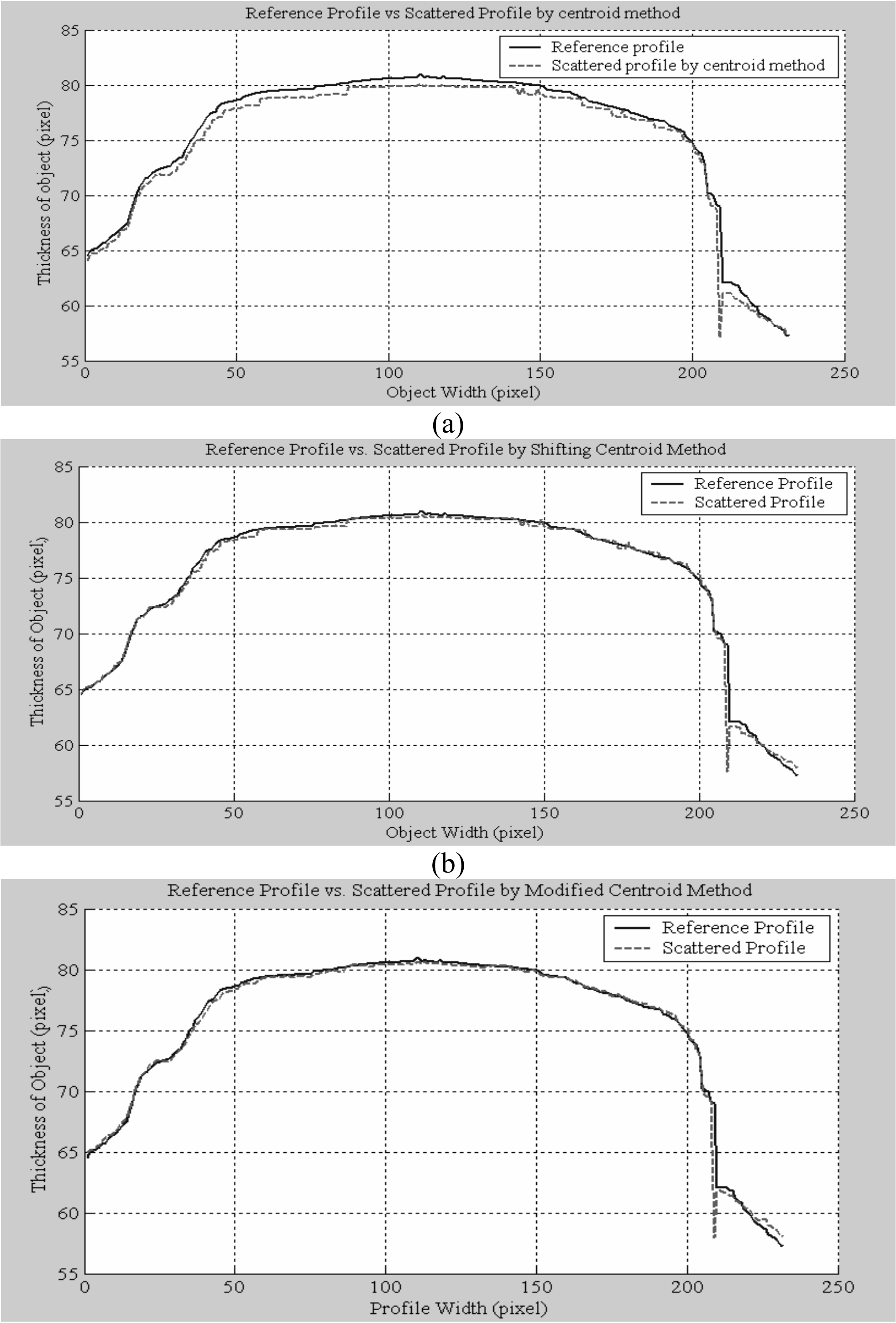

(a)

(b)

(c)

Figure 19. Result comparison from twenty samples. (a) Reference profile vs. centroid profile, (b) reference profile vs. shifted centroid profile, and (c) reference profile vs. modified centroid profile

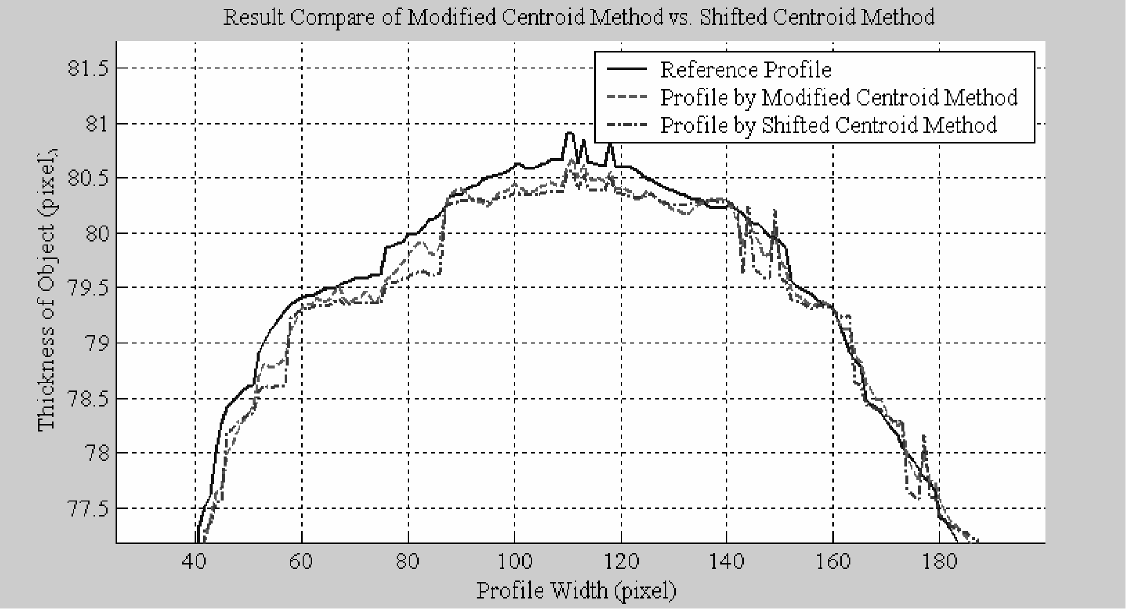

Figure 20. Detailed comparison between modified centroid method and shifted centroid method

From Table 2, both methods performed well but the modified centroid method was slightly better than the shifted centroid method. The results of both methods were only 0.2 pixels deviated from the ideal reference point. From Figure 20, the modified centroid method can be seen to have less variation than the shifted centroid method. Therefore, the modified centroid method was selected.

### 5.4.4 3D Image Repeatability Test

Because the scattering phenomenon occurred when the laser beam struck the surface of the poultry product and scattering is not a stable phenomenon, the repeatability of the obtained results was tested. The experiment tested two aspects, one with the conveyor belt in a static position and the other one when the conveyor belt was moving. In the first experiment, a piece of poultry meat was placed on the conveyor belt. The image profile was captured five times in short intervals. Then the depth was calculated and the results of the study were compared. To compare the results, the average of the five trials was calculated, and then every trial was compared with the average value. The total of 20 sample lines were scanned and compared. The results of the repeatability test, shown in Table 3, were very stable, and there was no fluctuation between trials.

Table 3. Static reproducibility test (pixels) based on 20 poultry fillet samples.

| Test | dev | Variance | Min. deviation | Max. deviation |
|---|---|---|---|---|
| 1 | 0.00 | 0.00 | 0.00 | 0.00 |
| 2 | 0.00 | 0.00 | 0.00 | 0.00 |
| 3 | 0.00 | 0.00 | 0.00 | 0.00 |
| 4 | 0.00 | 0.00 | 0.00 | 0.00 |
| 5 | 0.00 | 0.00 | 0.00 | 0.00 |

(one pixel represents 0.7 mm by 0.7 mm).

In the second test, a whole piece of meat was scanned by the laser imager. As in the single line test, one piece of meat was put on the belt and it was repeatedly scanned five times. A total of 20 boneless poultry breast fillets were scanned. Because the trigger pulse interval was not uniform, the scanned image length was not the same and the normalization had to be made.

Table 4. Test of dynamic reproducibility (pixels) based 20 poultry fillet samples.

| Test | dev index | Variance | Min. deviation | Max. deviation |
|---|---|---|---|---|
| 1 | 0.18 | 0.13 | -0.56 | 0.56 |
| 2 | 0.11 | 0.05 | -0.3 | 0.37 |
| 3 | 0.11 | 0.05 | -0.37 | 0.37 |
| 4 | 0.16 | 0.1 | -0.6 | 0.56 |
| 5 | 0.09 | 0.02 | -0.2 | 0.2 |

The standard deviation of the residual was less than 0.18 pixels (Table 4). The minimum and maximum deviations were less than 0.6 pixels. The residuals were larger than those in the static condition because of vibration and slight variation of the conveyor belt.

## 5.5 Conclusions

In the laser 3D range image system, light scattering occurs when the laser light strikes the poultry fillet surface. Because the light scatter in the poultry meat was on the same scale as the visible light wavelength, using any visible wavelength laser source will not reduce the scattering. Although biological materials are heterogeneous, skeletal muscle cells demonstrate some symmetry, and the cross sectional shape of the laser profile reflected from the poultry breast meat surface can be considered symmetrical.

Because part of the reflected light scatters in every direction, although it is symmetric to the incident light plane, the laser profile collected by the camera is not symmetrical. To compensate for the profile skew, a modified centroid method with a symmetrical index was proposed to obtain the correct profile center based on the biased image captured by CCD camera.  The proposed modified centroid method is capable of reducing the influence of the scattering.  Based on experimental results, the calculated profile has an accuracy of 0.14 mm by 0.14 mm and it was stable in the sense that it can be repeated.

# Chapter 6

# CALIBRATION OF LASER AND X-RAY SYSTEMS

## 6.1 Introduction

Bone fragments left in boneless poultry meat are a big health concern to consumers. As the consumption of boneless poultry products increases every year, methods to accurately detect bone fragments are desired by the poultry industry. X-ray technology is traditionally used by the industry for bone fragment detection. Based on the principle that meat and bone have different X-ray absorption rates, the X-ray image intensity is different when the thickness is different. However, due to the thickness variation of individual poultry fillets, it is impossible to detect the presence of bone fragments using X-ray technology alone (Chen, 2003). Tao and Ibarra (2000) suggested adding a laser 3D subsystem and combining the depth information from the laser 3D image with the X-ray image to reduce the influence of the thickness irregularity of the fillet. The calibration of the optical devices used in the laser subsystem is critical to the success of the new detection technology.

Camera calibration is very important for an accurate description of geometrical features of a measured object. Normally, the pin-hole model is adopted to calibrate the camera. The calibration parameters are classified as intrinsic and extrinsic parameters (Tsai, 1987). Intrinsic parameters model the internal structure of the camera, such as focal length and aberration correction, while extrinsic parameters represent the relationship between the camera coordinate system and the world coordinate system, such as relative translation and rotation. Much work has been done to calibrate cameras based on the pin-hole model. Tsai et al. (1987) proposed a very accurate method to resolve the calibration problem, but the reference object had to be built with high accuracy. Similarly, Zhang (1999) used a checkerboard pattern printed on paper by a normal laser printer to calibrate the camera, and obtained a similar resolution. Reimar and Lenz (1988), Heikkila (2000), and Shen and Meng (2001) all developed their own techniques based on specific applications.

X-ray imaging is different from normal optical imaging devices, such as a CCD camera. The X-ray image intensity reflects the total absorption of the X-ray in its path by the measured object. The X-ray image of an object is defined by a combination of perspective and affine transformations (Nobel, et al., 1998). Thus the X-ray image is warped due to this transformation (Grant, et al., 2001). Nevertheless the transformation process can still be modeled by the pin-hole camera model and corrected by coordinate transformation (Gronenschild, 1997).

In general, the calibration and registration of multiple sensors is difficult. There are numerous reports on sensor data fusion and registration (Cortelazzo, et al., 1998, Hastreiter and Ertl, 1998, and Shen and Meng., 2001). In this chapter, a model based on the camera's optical characteristics is established first. Then, with the help of reference objects, the relationship between world coordinates and camera coordinates is found, and the parameters describing the established model are calculated. Calibrated range imaging data are used for mapping thickness information in the consequent chapter.

## 6.2 Objectives

In this combined X-ray and laser 3D range system, three sensors were included. To ensure the accuracy of the calibration result, the geometrical relationship between the X-ray and laser beams was investigated. The objective of the research presented in this chapter was to develop a geometrical calibration method for the laser range imaging and the X-ray, and to obtain the relationship between the X-ray and laser beams, enabling the pixel registration of the X-ray and laser images.

## 6.3 Materials and Methods

### 6.3.1 Dual Imaging System Setup

The dual imaging system was designed and built to capture both X-ray and laser 3D images simultaneously. It included two imaging subsystems: an X-ray imaging subsystem and a laser 3D imaging subsystem. The laser 3D subsystem was

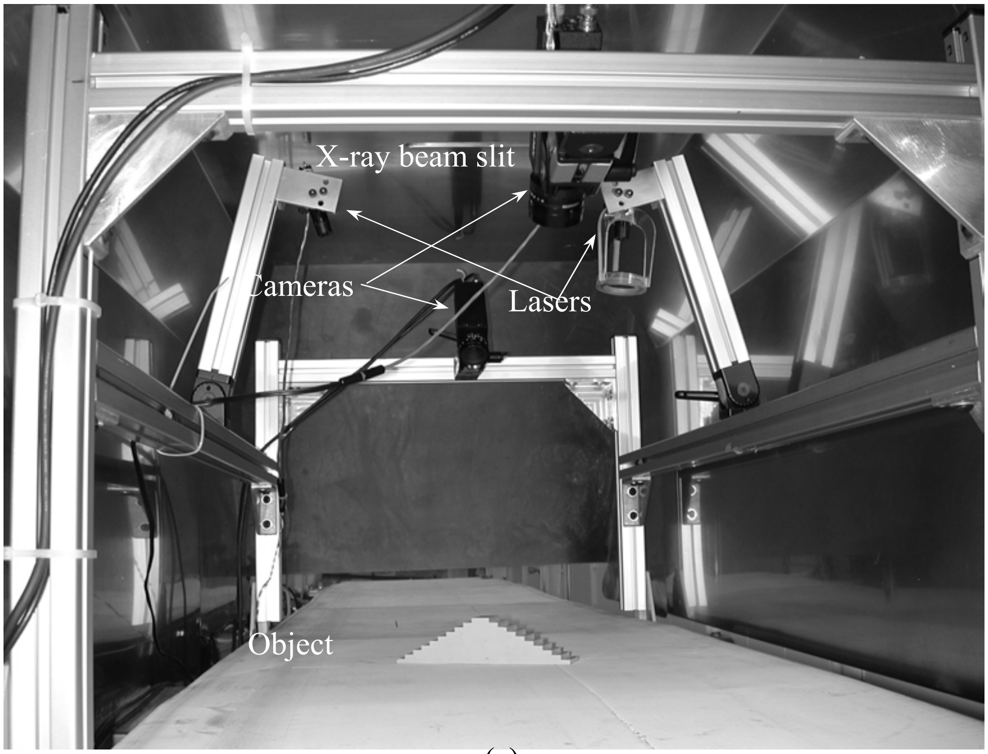

(a)

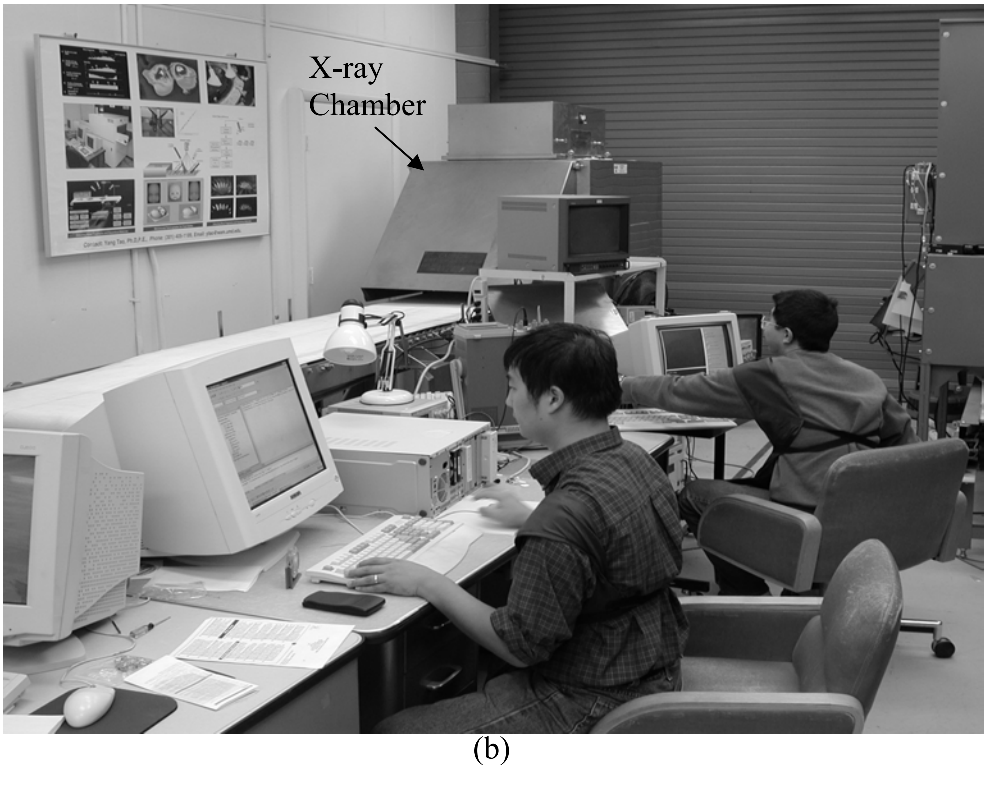

(b)

Figure 21. The setups of the dual imaging system. The laser range imaging system (a) is housed inside the X-ray Chamber as shown in (b).

housed entirely in an X-ray chamber. To correctly align images and reduce the mismatch of two images by possible slipping of the conveyor belt, the laser beam was arranged to stay as close to the X-ray beam as possible. The laser system is shown in Figure 21. For X-ray image acquisition, an X-ray tube and detector were used. The voltage and current of the X-ray tube were optimally adjusted for poultry fillet imaging (Chen, 2003). To obtain the 3D image, two cameras (Pulnix TM-6703, Pulnix America, Inc. Sunnyvale, CA) and two laser beam generators (635 nm, Lasiris SNF501L, Stockyale, Canada) were used. The two cameras were connected to one Matrox Genesis LC board (Matrox Electronics Systems Ltd., Quebec, Canada), and they were placed on each side of the structured laser pattern generator to reduce the influence of possible occlusion caused by curvature of the poultry fillet. The frame grabber was hosted in a Pentium IV computer. The cameras and laser structure light generator were mounted on a frame that was fixed in the X-ray chamber. The test object was placed on the conveyor belt that traveled under the X-ray and laser light.

### 6.3.2 Calibration Algorithms

The following procedures were conducted in the whole system setup:

1. Calibration of intrinsic and extrinsic parameters of the two cameras;
2. Correction of errors due to the camera lens distortion and projection transformation;
3. Computation of X-ray parameters;

4. Correction of X-ray geometrical distortion introduced by the cone beam effect;
5. Calculation of the relation between the two cameras;
6. Attainment of the relationship between the laser and X-ray beams.

#### *6.3.2.1 Camera Pin Hole Model*

To calibrate a camera, the pin-hole model is normally adopted. The pin-hole model (Tsai, 1987) is represented in Figure 22. In this model, parameters are divided into extrinsic parameters and intrinsic parameters. The extrinsic parameters correspond to the translation and rotation transformations of the camera coordinates

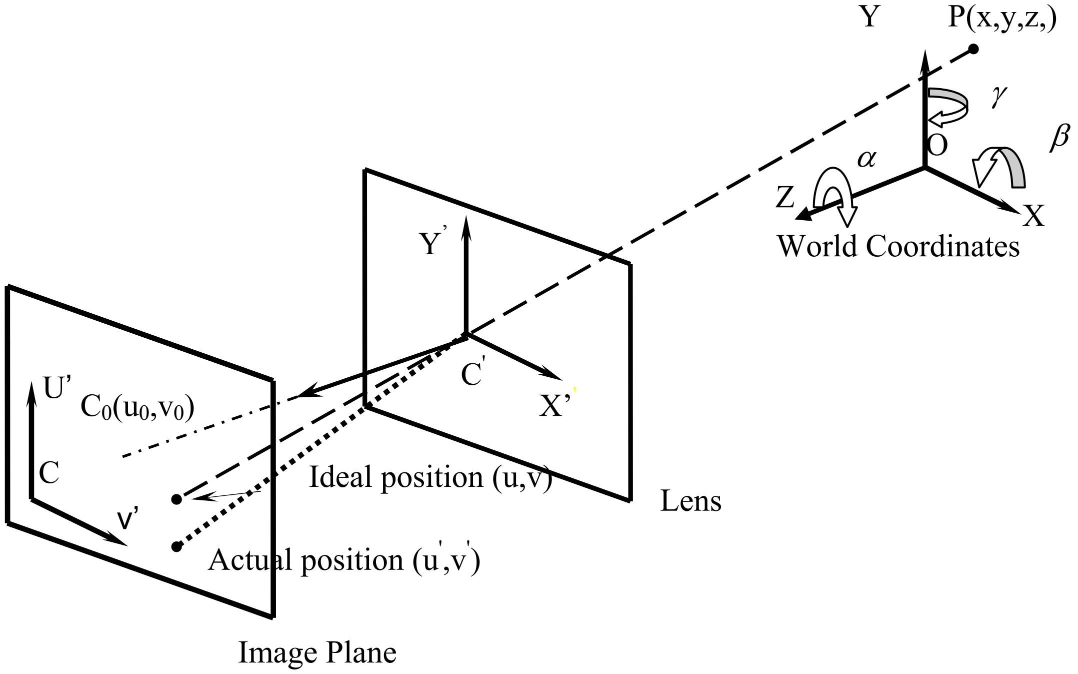

Figure 22. Illustration of a typical Pin-Hole camera model (Tsai, 1987).

into the world coordinates. The translation and rotation transformations can be expressed by the homogeneous transformation

$$\begin{bmatrix} x' \\ y' \\ z' \\ 1 \end{bmatrix} = \begin{bmatrix} r_{11} & r_{21} & r_{31} & t_x \\ r_{12} & r_{22} & r_{32} & t_y \\ r_{13} & r_{23} & r_{33} & t_z \\ 0 & 0 & 0 & 1 \end{bmatrix} \begin{bmatrix} x \\ y \\ z \\ 1 \end{bmatrix}, \tag{22}$$

where $(x, y ,z ,1)'$ is the object position in the world coordinate system; $T=(t_x,t_y,t_z)'$ is the translation of the world coordinate center to the lens coordinate system and $R=(r_1, r_2, r_3, 0)$ is the rotation of the world coordinate to the lens coordinate system. Further, the rotation matrix can be decomposed into the form

$$R = \begin{bmatrix} AB & CE+ADF & CF-ADE \\ -CB & AE-CDF & AF+CDE \\ D & -CB & BE \end{bmatrix}, \tag{23}$$

$$A = \cos(\alpha), \tag{24a}$$
$$B = \cos(\gamma), \tag{24b}$$
$$C = \sin(\alpha), \tag{24c}$$
$$D = \sin(\gamma), \tag{24d}$$
$$E = \cos(\beta), \tag{24e}$$
$$F = \sin(\beta), \tag{24f}$$

where $\alpha$, $\beta$, and $\gamma$ are angles with which each sensor plane rotates around the Z, X, and Y axes of the world coordinates, respectively. Then, points in the world coordinate system are transformed to the image coordinate system.

In the intrinsic transformation, several parameters are considered. First, image points are projected onto the image plane and the projection transformation can be described by following equation

$$\begin{pmatrix} \lambda u \\ \lambda v \\ \lambda \end{pmatrix} = \begin{bmatrix} f & 0 & 0 & 0 \\ 0 & f & 0 & 0 \\ 0 & 0 & 1 & 0 \end{bmatrix} \begin{bmatrix} x' \\ y' \\ z' \\ 1 \end{bmatrix}, \tag{25}$$

where $f$ is the focal length of the lens.

Furthermore, the actual image plane (CCD sensor) may have different scales in the horizontal and vertical directions and the angle between the two lens axes may not be a perfect right angle due to manufacturing tolerance. In this case, another matrix is introduced to correct for these errors (Figure 23).

$$\begin{pmatrix} \lambda u' \\ \lambda v' \\ \lambda \end{pmatrix} = \begin{pmatrix} d_u & -d_v \cot\theta & u_0 \\ 0 & \dfrac{d_v}{\sin\theta} & v_0 \\ 0 & 0 & 1 \end{pmatrix} \begin{bmatrix} f & 0 & 0 & 0 \\ 0 & f & 0 & 0 \\ 0 & 0 & 1 & 0 \end{bmatrix} \begin{bmatrix} x' \\ y' \\ z' \\ 1 \end{bmatrix}, \tag{26}$$

where $\theta$ is the actual angle between the two lens axes, and $d_u$ and $d_v$ represent the scale factors in the horizontal and vertical directions, respectively. $u_0$ and $v_0$ are the deviations of the center of the actual coordinates from the center of the ideal coordinates center of the image sensor plane.

Overall, any point in the world coordinate system can be projected onto an image sensor by the transform

$$p = I \times E \times P, \tag{27}$$

where $p(u',v',1)$ is the position in the obtained image, $P(x,y,z,1)$ is the point in the world coordinate system, both p and P are expressed in homogeneous form, $I$ is the intrinsic parameter matrix, and $E$ is the extrinsic transform matrix.

Lens distortion should also be accounted for. There are five aberrations introduced by lens distortion: spherical aberration, coma, astigmatism, curvature of the field, and distortion. The last two distortions have the largest effects on image deformation (Jeffrey, et al., 1994). To allow for lens distortion, nonlinear parameters were added to the model. According to Tsai (1987), only coupling second order radial distortion to the calibration model can obtain a very accurate result. In the normalized image plane, which is an ideal virtual plane with z equal to one, the position can be expressed by (Brown, 1971, Wei and Ma, 1994, and Zhang, 1999)

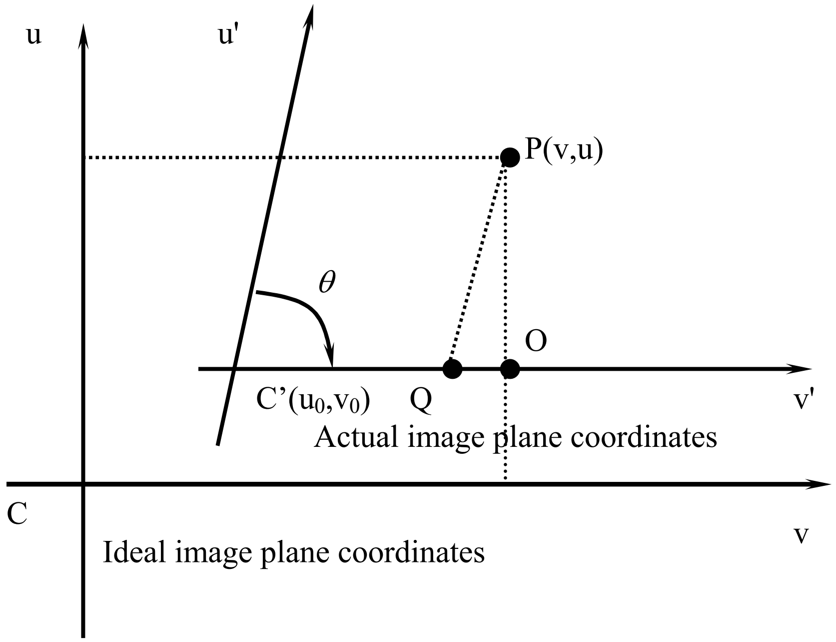

Figure 23. Illustration of actual image sensor coordinates

$$x'' = xi + xi[k_1r^2 + k_2r^4 + O(r^6)], \tag{28a}$$

$$y'' = yi + yi[k_1r^2 + k_2r^4 + O(r^6)], \tag{28b}$$

where *x"* and *y"* are distorted normalized image coordinates, *xi* and *yi* are coordinates in the ideal normalized image coordinate system. $k_1$ and $k_2$ are two non-linear indices that need to be calculated, and $r^2 = x^2 + y^2$ is the distance from that point to the lens center.

In the sensor plane, incorporating Equation 26 into Equation 28, and after some simplification, the equation can further be expressed by

$$u' = u + (u - u_0)[k_1 r^2 + k_2 r^4 + O(r^6)], \tag{29a}$$

$$v' = v + (v - v_0)[k_1 r^2 + k_2 r^4 + O(r^6)], \tag{29b}$$

where *u'* and *v'* are actual coordinates in the sensor plane, and *u, v* are ideal coordinates. $u_0$ and $v_0$ are the shifted sensor center from the ideal center position.

### *6.3.2.2 Camera Calibration*

Because lens distortion has been introduced into the calibration, it is impossible to get a closed form solution to the calibration of all of the parameters. A large amount of research has been done to calculate the intrinsic and extrinsic parameters (Abdel-Aziz and Karara 1971; Tsai, 1987; Zhang 1999; and Heikkila, 2000). The process of calibration is divided into two steps. First, an initialization is made based on some criteria and then a maximum likelihood estimation is applied to the initialization to find the best estimation of calibration parameters.

Assuming the calibration points are all in the X-Y plane of the world coordinate system, Z will be zero and the transformation in Equation 27 can be simplified as (Zhang, 1999)

$$\lambda \begin{bmatrix} u' \\ v' \\ 1 \end{bmatrix} = I \times \begin{bmatrix} r_1 & r_2 & t \end{bmatrix} \begin{bmatrix} X \\ Y \\ 1 \end{bmatrix}, \tag{30}$$

Because the exact values of *(u', v', 1)*$^T$ and *(X, Y, 1)*$^T$ are known, Equation 30 is simplified into the following form

$$\lambda \begin{bmatrix} u' \\ v' \\ 1 \end{bmatrix} = Q \begin{bmatrix} X \\ Y \\ 1 \end{bmatrix}, \tag{31}$$

where $Q = I \times \begin{bmatrix} r_1 & r_2 & t \end{bmatrix}$.

There are 11 unknowns in Equation 31. The closed form estimation is available as suggested by Tsai (1987), Zhang (1999), and Forsyth and Ponce (2002). With the presence of lens distortion, the solution will always be the estimation of the real value. Then the nominal values of the intrinsic parameters in Equation 31 are used to calculate the rotation and translation parameters. Equation 31 is further simplified to

$$I^{-1}Q = \begin{bmatrix} r_1 & r_2 & t \end{bmatrix}. \tag{32}$$

Then, the extrinsic matrix columns are calculated with

$$r_1 = (I^{-1}Q)_1, \tag{33a}$$

$$r_2 = (I^{-1}Q)_2, \tag{33b}$$

$$r_3 = r_1 \times r_2, \tag{33c}$$

$$t = (I^{-1}Q)_3,, \tag{33d}$$

Because $R$ calculated in this way is likely not orthonormal, further calibration is needed to extract the actual rotation matrix $R'$ (Kanatani, 1993 and Zhang, 1999).

$$\sum_{1}^{N} \left\| R - R' \right\|^2 \rightarrow \min \text{, subject } R'R'^{T} = I. \tag{34}$$

Because only intrinsic and extrinsic parameters are considered in the above calculation, the result can only be used as initialization. Due to the nonlinear nature of lens distortion, maximum likelihood estimation (MLE) (Tsai, 1987; Zhang 1999; and Heikkila, 2000) has to be applied to find the optimal estimation for all the intrinsic, extrinsic and distortion parameters. The estimation can be expressed as

$$\sum_{i,j} \left\| p - p'\left(I, E, P\right) \right\|^2 , \tag{35}$$

Normally, the Levenberg-Marquardt method is used to minimize Equation 35 (Bates and Watts, 1988), which converges after several iterations.

#### *6.3.2.3 X-ray Image System Calibration*

Geometrically, X-ray imaging can also be described by the pin-hole model (Figure 24). In Figure 24, the distance between the X-ray source and the detector was considered as the focal length of the imaging device, the image plane as the detector plane, and the object coordinates as the world coordinates. There were six unknowns: $f$, the focal length of the X-ray image; $\theta$, the angle between the x-axis of the world coordinates and X-ray detector plane $u_{x0}$, the deviation from the ideal coordinates center; $xt_x$, $xt_y$, the translation of origin of the world coordinates to the X-ray coordinates; and $d_x$, the scale factor of the X-ray detector. Then Equation 26 is simplified to

$$\lambda_x \begin{bmatrix} u_x \\ 1 \end{bmatrix} = \begin{bmatrix} f_x d_x & u_{x0} & 0 \\ 0 & 1 & 0 \end{bmatrix} \begin{bmatrix} \cos\theta & \sin\theta & xt_x \\ -\sin\theta & \cos\theta & xt_y \\ 0 & 0 & 1 \end{bmatrix} \begin{bmatrix} x \\ y \\ 1 \end{bmatrix}, \tag{36}$$

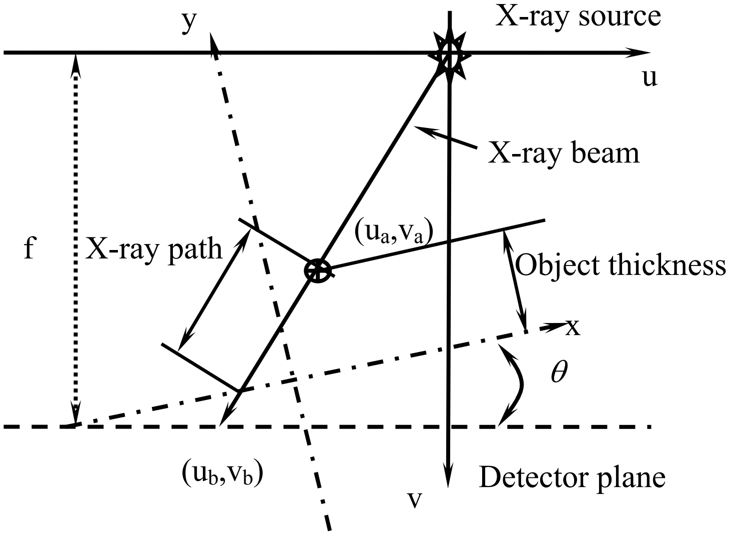

Figure 24. Illumination of X-ray model.

The same method as the camera calibration was used to calibrate this function and the optimal minimization method was used to calibrate the X-ray subsystem.

### *6.3.2.4 X-ray Cone Beam Effect Elimination*

Although X-ray can be simulated by the pin-hole model, its imaging principle is different from normal camera imaging where image intensity represents the surface reflection of incident light. If the X-ray's incident intensity is $I_0$, and it travels through a medium of density $\rho$ and the travel length is *t,* the exponential attenuation law (Beer's Law) predicts that the detected X-ray energy has intensity *I* given by

$$I = I_0 \exp\left[ -\int_T \frac{\mu(x,y,z)}{\rho(x,y,z)} dt \right], \tag{37}$$

where $\mu/\rho$ is the mass-energy absorption coefficient that characterizes the medium (Ryon, et al., 1988). That means the X-ray image intensity is related to the travel length of the X-ray and not simply the thickness of the object. Therefore, the cone-beam effect should be considered when a laser 3D image is used to correct for the thickness variation. From Figure 24, the real X-ray path is not only determined by the distance from the object surface to the detector plane, it is also influenced by the angle between the X-ray beam and X-ray detector plane

$$T = \int_T f(d,\theta) dt, \tag{38}$$

where d is the geometrical thickness of the object, and $\theta$ is the angle between a single X-ray beam and the *v* axis in the X-ray coordinate system (Figure 24). In Figure 24, if $(u_a, v_a)$ is the real image position in the X-ray coordinate system, its projection is located at $(u_b, v_b)$, and the X-ray path is

$$T = \sqrt{(ua-ub)^2 + (va-vb)^2} \text{ or } T = d/\cos(\theta), \tag{39}$$

Therefore, the points with the same height to the detector plane have different X-ray absorptions, and hence the image intensity is different at the points that are the same distance to the detector plane but at a different position. Accordingly, the laser image height needs a similar transformation to correct the warping of the X-ray image intensity by

$$v'' = v'/\cos(\theta), \tag{40}$$

where *v"* represents the transformed height, and *v'* represents the original height of the object.

### 6.3.2.5 Laser and X-ray Beam Geometrical Relation

In the combined imaging system, both X-ray and laser light beams are projected on the object. To match the X-ray image with the laser image, the laser beam and X-ray beam should be parallel to each other. In reality, the X-ray plane and laser light sheet plane may not be parallel, and their relationship to each other needs to be calculated. Suppose that the X-ray beam plane is in the *y-z* plane of the coordinate system as illustrated in Figure 25. Their relation can be determined by the angles $\alpha$ and $\beta$ angles

$$\begin{bmatrix} x_x \\ y_x \\ z_x \end{bmatrix} = \begin{bmatrix} \cos\alpha & \sin\alpha\cos\beta & \sin\alpha\sin\beta \\ -\sin\alpha & \cos\alpha\cos\beta & \cos\alpha\sin\beta \\ 0 & -\sin\beta & \cos\beta \end{bmatrix} \begin{bmatrix} x_l \\ y_l \\ z_l \end{bmatrix}, \tag{41}$$

where $\alpha$ represents the rotation angle of the laser plane around the *z*-axis and $\beta$ represents the angle of its rotation around the *y*-axis.

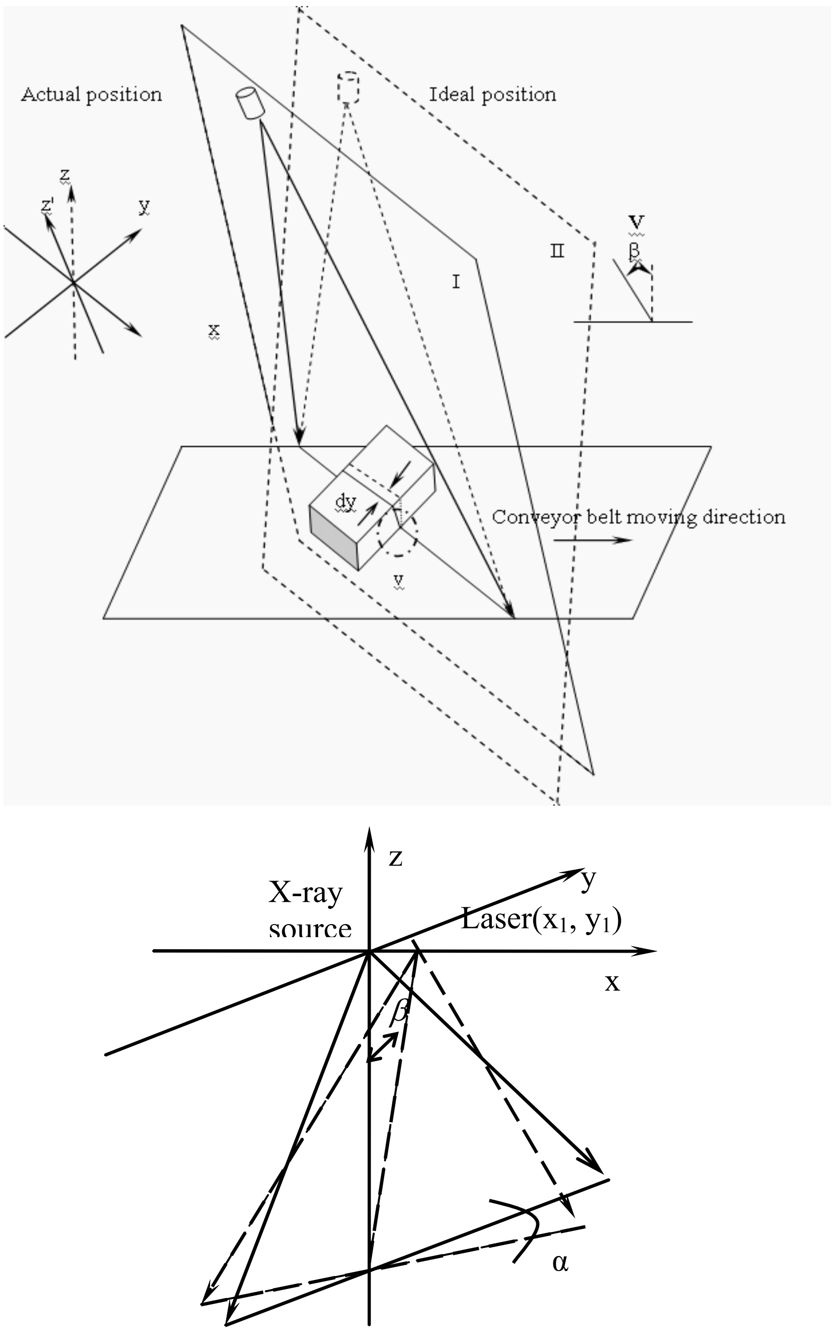

Figure 25. Illumination of laser and X-ray beam model and its relation.

To calibrate the X-ray and laser beam plane, a calibration object is needed. To determine the angle $\alpha$, an object of known size is scanned by the dual imaging system.

Because the distance the object moves, *l,* and object height, *h,* are already known , the angle $\alpha$ can be calculated by

$$\alpha = \arctan\left(\frac{l}{h}\right), \tag{42}$$

and the resolution of $\alpha$ is determined by

$$\Delta\alpha = \frac{nh}{h^2 + l^2}\Delta p\,, \tag{43}$$

where n is the total number of pulses generated when the object travels distance $l$ along the conveyor belt, and $p$ is the encoder resolution. The resolution of $\alpha$ is determined by the encoder resolution $p$.

The same approach is used to obtain the angle $\beta$. Because the angle $\alpha$ is known and the relative positions of laser and X-ray beams have been adjusted, the effects of the positions do not need to be considered when computing the angle $\beta$. Again, a known size rectangular block is used as the reference. The block is placed on the conveyor belt at approximately the same direction as the conveyor belt (the exact direction of conveyor belt is not known and does not need to be known, because only the X-ray and laser images are of importance). Suppose A, B, and C are three corners of the rectangle, the distance from A to B is $D_1$, and from B to C is $D_2$. After scanning, the 3D image (Figure 26) is warped. But the distance between point C and point F has not changed, as well as the distance between point A and point E. Based on this condition, the angle $\alpha$ is found by

$$\alpha = \arctan\left(\frac{D_1 d_2}{D_1\sqrt{D_2^2 - d_2^2} - d_1}\right). \tag{44}$$

After all of these calibrations, the laser light sheet plane is parallel to the X-ray beam plane.

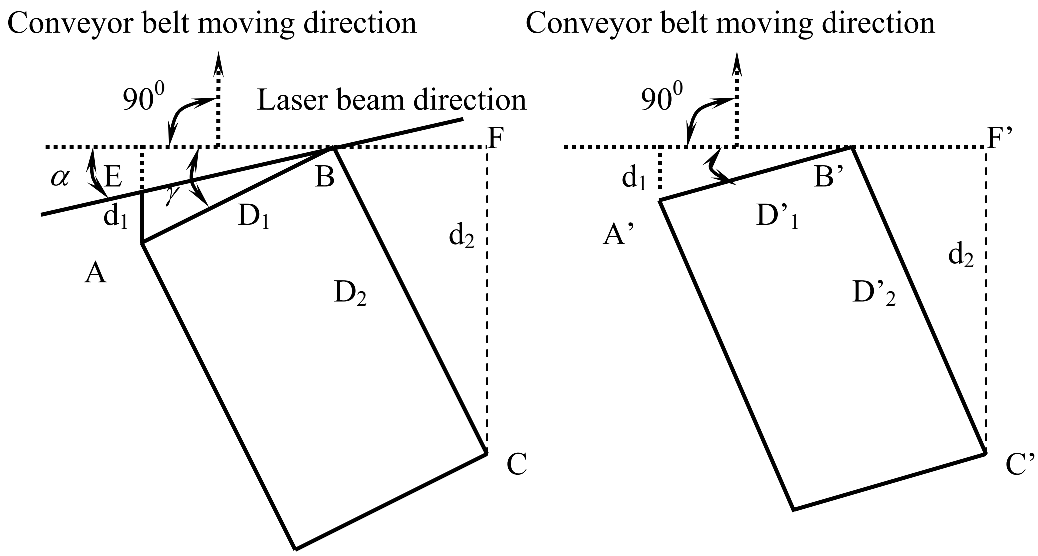

Figure 26. Illustration of angle $\alpha$ calculation.

### *6.3.2.6 Back Projection Calculation*

All of the parameters have been calculated and now the point located in the image plane can be calculated from its world coordinates by the equation

$$p = IEP + \delta\,, \tag{45}$$

where $\delta$ is the distortion caused by the lens.

In actual application, the coordinates in the sensor plane are known, but the world coordinates need to be determined by inverse computation. Because $\delta$ is nonlinear, it is difficult to obtain an accurate result without time-consuming iterative searching. Heikkila (2000) proposed a very accurate non-iterative model to compute the distortion. In his method, the following equation was used to calculate the ideal object coordinates in the image coordinate system from its distorted image

$$\begin{bmatrix} u \\ v \end{bmatrix} = \frac{1}{G}\begin{bmatrix} u'+u'(k_1r^2+k_2r^4)+2k_3u'v'+k_4(r^2+2u'^2) \\ v'+v'(k_1r^2+k_2r^4)+k_3(r^2+2v'^2)+2k_4u'v' \end{bmatrix}, \tag{46}$$

where $G=(k_5r^2+k_6u'+k_7v'+k_8)r^2+1$, and $k_1$ to $k_8$ are non-linear indices.

Although the average error of this method was less than 0.01 pixels and an iteration calculation was not used, it still required a lot of calculation and it cannot be applied to real-time applications.

Based on the distortion model as indicated in Equation 29, we can have

$$\begin{bmatrix} \delta_u \\ \delta_v \end{bmatrix} = \begin{bmatrix} (u-u_0)[k_1r^2+k_2r^4]+O(r^6) \\ (v-v_0)[k_1r^2+k_2r^4]+O(r^6) \end{bmatrix}, \tag{47}$$

where $\delta_\mu$, $\delta_v$ are the error values in the *u* and *v* directions. $\delta_u$ and $\delta_v$ are functions of *(u,v,r)*. After applying Taylor expansion (Askey and Haimo,1996) to Equation 47,

$$\begin{bmatrix} \Delta\delta_u \\ \Delta\delta_v \end{bmatrix} = \begin{bmatrix} (k_1r^2+k_2r^4)\Delta u+(u-u_0)[2k_1r+4k_2r^3]\Delta r \\ (k_1r^2+k_2r^4)\Delta v+(v-v_0)[2k_1r+4k_2r^3]\Delta r \end{bmatrix}, \tag{48}$$

where $\Delta\delta_u$ and $\Delta\delta_v$ are the distortion rates in the *u* and *v* directions. Because the measured object's size is relatively small compared with its distance to the camera lens, $r$ is much smaller than 1 (Appendices D and E), the influence of the $r^3$ term in Equation 47 is negligible. Furthermore, replacing $r$ with $\sqrt{x^2+y^2}$ in Equation 48 gives

$$\begin{bmatrix} \Delta\delta_u \\ \Delta\delta_v \end{bmatrix} \approx \begin{bmatrix} k_1(x^2+y^2)\Delta u + (u-u_0)k_1(x\Delta x + y\Delta y) \\ k_1(x^2+y^2)\Delta v + (v-v_0)k_1(x\Delta x + y\Delta y) \end{bmatrix}, \tag{49}$$

Now, the distortion can be calculated based on its neighboring points' distortion, and distortion can be eliminated from Equation 45. At this stage, the intrinsic parameters, extrinsic parameters and distortion parameters are all known, and a point's coordinates in the world coordinate system can be calculated from its coordinates in the image (sensor plane) coordinate system.

To make this method accurate, a look-up-table is constructed. The data in the look-up-table represents the distortion at that point in the sensor plane. The data points cover the sensor plane and form an evenly spaced 2D grid. Because a Taylor expansion was used to derive Equation 48, the accuracy of the result depends on the size of the grid. The smaller the size of the grid, the more accurate the result.

#### *6.3.2.7 Calibration Procedures*

The whole system calibration was calibrated by the following steps:

1. The camera's intrinsic and extrinsic parameters were calibrated using calibration patterns. First, the intrinsic parameters were calculated, then, the

extrinsic parameters were calculated when the cameras were mounted in the X-ray chamber (Appendices D and E).

2. The geometrical relation of the laser beam and X-ray beam were revealed by scanning a calibration block placed on the conveyor belt. The laser position was then adjusted to be parallel with the X-ray beam.
3. The X-ray image was calibrated using the calibration pattern. Due to the X-ray imaging characteristics, a special calibration object was made by the Computer Numerical Controlled (CNC) machine machine as shown in Figure 27.
4. The extrinsic parameters of the camera were re-calibrated in the X-ray chamber using the calibration block. The laser beam plane coincided with one plane of the world coordinate system. One look-up table was generated for the distortion correction after this step. Because computed coordinates in the world coordinate system were not necessarily evenly distributed in the 2D grid, linear interpolation was used to find those values.
5. Based on the X-ray imaging transformation matrix, the laser 3D image was transformed.

Because the conveyor only carried the object, its direction of motion affected the image but not the geometrical relationship of those sensors. Thus the direction of travel was not considered in the calibration process.

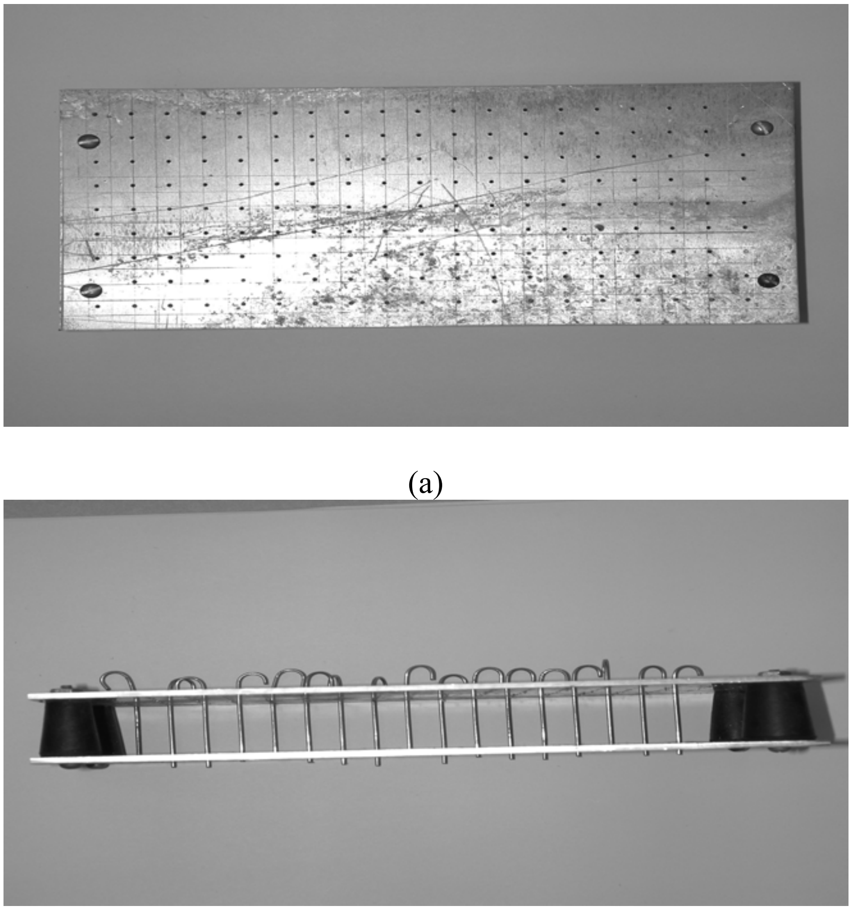

(a)

(b)

Figure 27. Images of object used for X-ray calibration. (a) The top view of calibration object, and (b) The side view of the steel pins inserted into the calibration object of (a).

## 6.4 Results and Discussion

In the calibration process, the conveyor surface plane was used as the reference plane, all the calculated height was based on this surface. To evaluate the performance of the calibration approach, the following experiments were conducted to investigate its accuracy.

### 6.4.1 Camera Reverse Calculation Accuracy

This experiment was used to test the accuracy of the inverse calculation under current settings. One thousand points were randomly generated in the sensor plane, and the distortion was calculated by Equation 47. Then Equation 49 was used to estimate the distortion from the distorted image points. The differences between the actual and estimated distortion were compared. Figure 28 shows that the error increased as the point's distance to the lens center increased. Because the proposed method was not rotation invariant, the distortion was different at points even when their distances to the center are the same. The worst case difference of the estimated method was only 0.21 pixels (1 pixel = 0.7 mm × 0.7 mm) when the points was 250 pixels away from the center. This demonstrated that the proposed method was very accurate under the current settings.

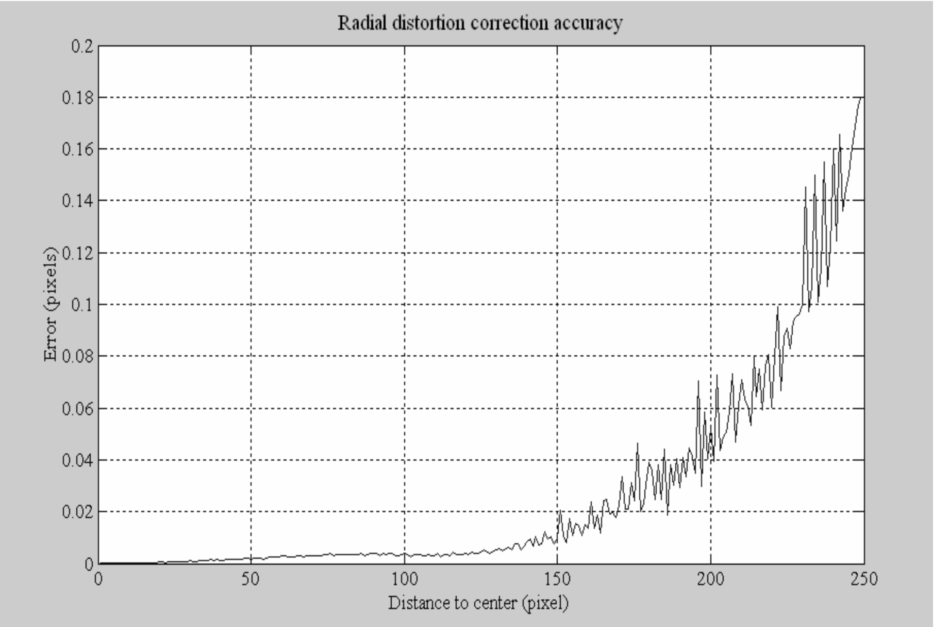

Figure 28. Illustration of reverse computing accuracy. The error increases as the point's distance to the lens center increases.

### 6.4.2 Camera Calibration

In this experiment, the camera image calibration precision was investigated. In the experiment, metal staircase blocks with height from 5 mm to 50 mm (Figure 29) were used. To ensure the accuracy of the result, the staircase blocks were made with an accuracy of 0.025 mm ( 0.036 pixels) by a Computer Numerical Controlled (CNC) machine. The blocks were placed on the conveyor and scanned. To each height plane, one thousand points were taken, and the calculated heights were compared with actual height value. Because the thickness of a chicken fillet is normally smaller than 50 mm, only the thicknesses equal or below 50mm are shown in Table 5. Table 5 shows that the calibration precision was accurate with a maximum error of 0.291mm. The data from the two cameras was very close, although one camera's data had a larger variation. However, the variation was still small compared to the real thickness.

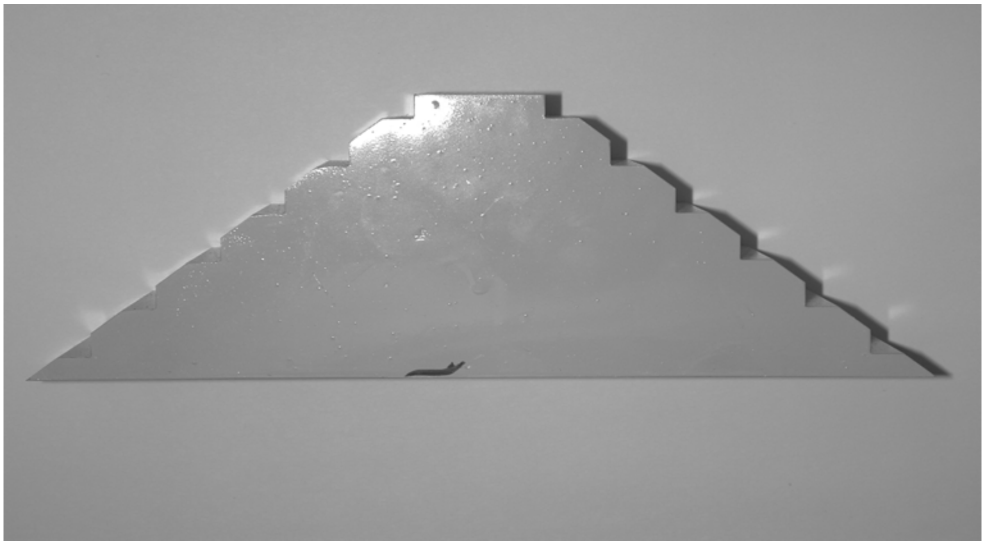

Figure 29. One of the blocks used in the calibration. It was milled by a CNC machine at an accuracy of 0.025 mm (0.036 pixels) in the x, y, and z directions.

Table 5. Camera calibration precision based on the 10 depth step test.

| Depth | First Camera | | | Second Camera | | |
|---|---|---|---|---|---|---|
| (mm) | Mean(mm | Std*(mm) | Error*(mm) | Mean(mm) | Std*(mm) | Error*(mm) |
| 5 | 4.836 | 0.0335 | -0.164 | 4.804 | 0.0922 | -0.196 |
| 10 | 9.743 | 0.0249 | -0.257 | 10.033 | 0.0652 | 0.033 |
| 15 | 14.772 | 0.0263 | -0.228 | 14.769 | 0.0760 | -0.231 |
| 20 | 19.974 | 0.0359 | -0.026 | 19.896 | 0.0691 | -0.104 |
| 25 | 24.99 | 0.0202 | -0.01 | 24.823 | 0.0614 | -0.176 |
| 30 | 30.226 | 0.0291 | 0.226 | 30.036 | 0.0454 | 0.036 |
| 35 | 35.291 | 0.0329 | 0.291 | 35.067 | 0.0434 | 0.067 |
| 40 | 40.141 | 0.0344 | 0.141 | 40.072 | 0.0500 | 0.072 |
| 45 | 44.995 | 0.0313 | -0.005 | 45.032 | 0.0484 | 0.032 |
| 50 | 50.012 | 0.0284 | 0.012 | 50.023 | 0.0442 | 0.023 |

*Std means standard deviation. Error means the difference between the measured and the actual heights.

### 6.4.3 Result of Corrected Laser 3D Image

In the combined bone fragment detection system, the ultimate goal was to combine 3D and X-ray imaging together. Because the 3D imaging was more flexible, the 3D images were transformed into a pseudo-X-ray image by Equations 36 and 40. In this experiment, the result of the transformation was examined by comparing the corner position of the calibration block in the 3D and X-ray images. As in the camera calibration, calibration objects with an accuracy of 0.025 mm × 0.025mm × 0.025mm in x-, y-, and z-direction were used. The calibration objects had different sizes and their heights ranged in size from 5 mm to 50 mm. The calibration blocks were placed on the conveyor at randomly selected locations. Both the X-ray and laser 3D images were grabbed, and were transformed by Equations 36 and 40. The horizontal positions of transformed 3D images were compared with the corresponding X-ray image points. Fifty points were compared. The results (Figure 30) show that the error became larger as the point's distance to the image center increased. The mean error was 0.183 mm and the largest error is 0.5 mm. Taking into account the 0.4mm resolution of the X-ray detector, it was about one pixel.

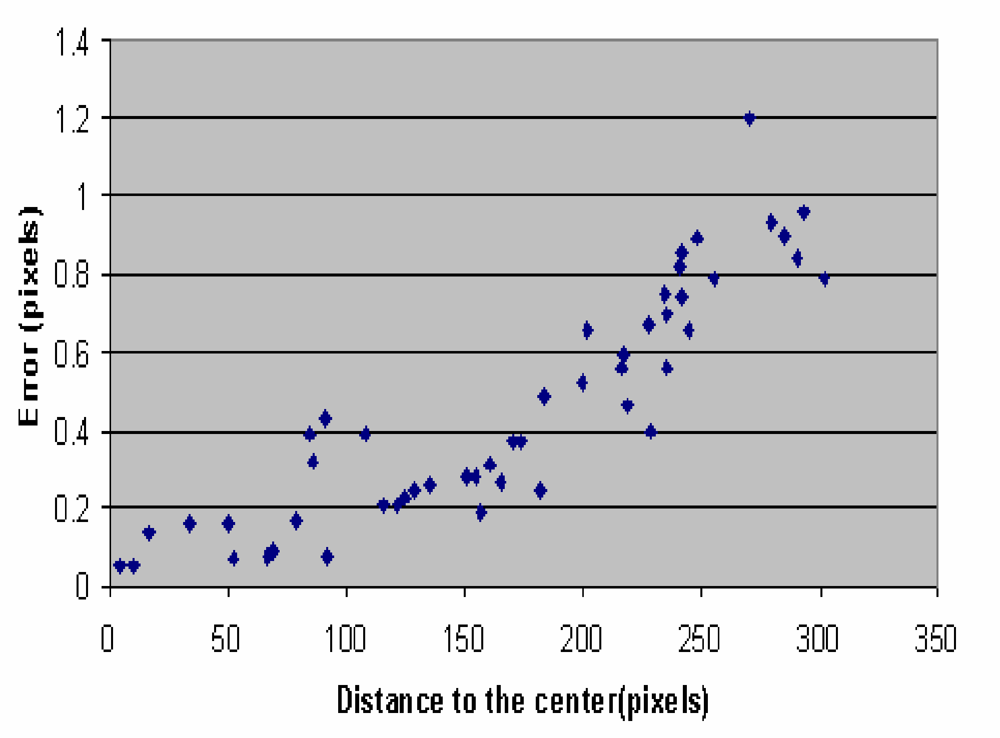

Figure 30. Error after the Laser 3D geometrical correction. The error became larger as the point's distance to the image center increased.

### 6.4.4 Typical Sample Image Results

A calibration block was scanned, and its calibrated image was shown in Figure 31. Figure 31(c) was the reconstructed image of the calibration block.

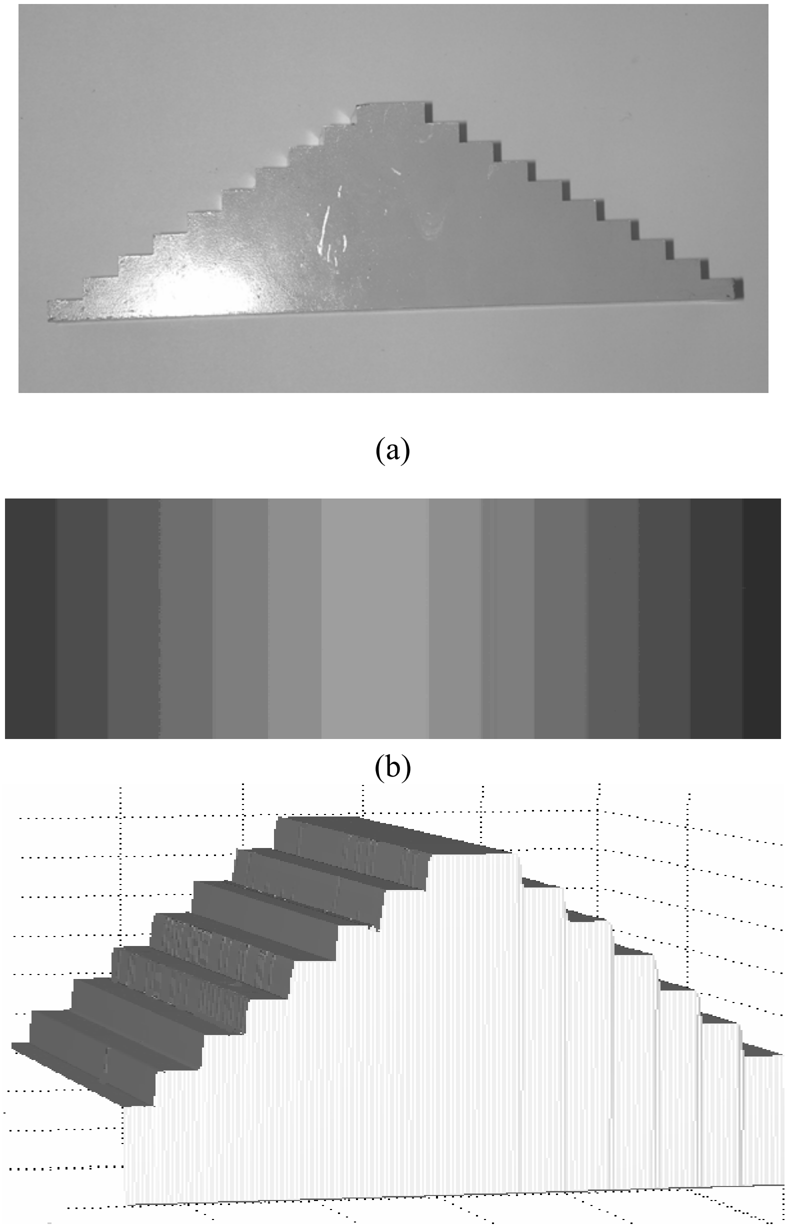
(a)

(b)

(c)

Figure 31. The 3D and reconstructed images of a calibration block. (a) Original image, (b) the calibrated 3D image, and (c) the reconstructed image.

Figure 32 shows images of a poultry meat. On the right is the calibrated 3D image. In the 3D image, the thicker the meat was, the brighter the image.

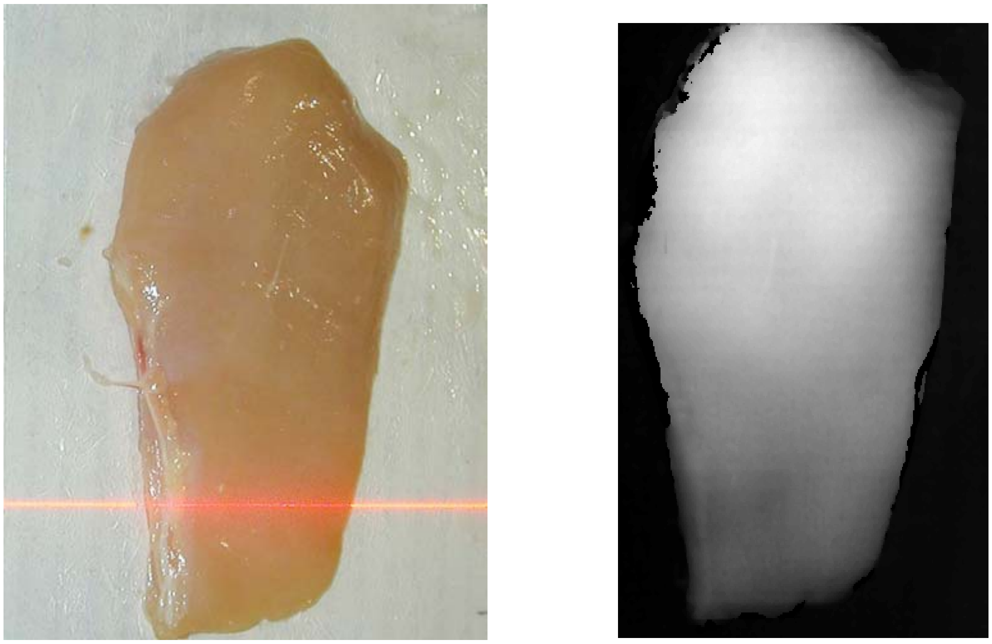

Figure 32. A typical example of poultry meat (left) and its 3D image (right).

The resulting laser range image was later transferred into a pseudo x-ray image for combined X-ray and laser bone fragment detection system. The pseudo X-ray image transformation will be described in Chapter 7.

## 6.5 Conclusion

In this chapter, the modeling and calibration of a multi-type multi-sensor system was conducted. The calibration was performed in four steps. First the calibration of the camera was carried out. In the camera calibration model, the calibration parameters were separated into intrinsic and extrinsic parameters. To obtain these parameters, a known-shaped object was used as a reference object and maximum likelihood estimation was applied to the computation.

Based on the experimental results, an accuracy of approximately 0.2 pixels (0.7mm/pixel in laser 3D image) was obtained from the calibration. To reduce the time spent on computing the image distortion, a reverse computing method was proposed and the accuracy was approximately 0.02 pixels using current settings. Second, the X-ray beam was modeled using a simplified pin-hole camera model, and the same algorithm that was used to calibrate the camera was applied to the calibration of X-rays. At the same time, the distortion caused by the fan beam effect was readily calculated. Third, the geometrical relationship of the X-ray beam and the laser beam was revealed, and the laser beam was adjusted accordingly. Finally, the performance of the calibration was evaluated. By using different objects of different shapes, the transformed 3D images matched the X-ray images very well. The average error was 0.183 mm.

Therefore, although some errors existed in the calibration, the proposed method was capable of producing an accurate range image for the input to the combined X-ray imaging system for the bone fragment detection.

# Chapter 7

# MAPPING OF 3D IMAGE TO PSEUDO-X-RAY IMAGE

## 7.1 Introduction

According to USDA regulations (USDA, 1999), de-boned meat is required to be free of any foreign parts and bone fragments. Extensive effort has been devoted to developing techniques to accomplish this difficult task. One of the frequently investigated techniques is X-ray technology. X-ray technology is widely used in areas where non-destructive detection is needed. However, it has had limited success in poultry bone fragment detection because the X-ray image intensity difference between bone and meat is small and the poultry fillet has an uneven thickness that results in false patterns in the X-ray images (Tao, et al., 2001). To tackle this difficult problem, a combined laser 3D range image and X-ray image system was proposed to provide higher sensitivity and accuracy and to eliminate the false patterns (Tao and Ibarra, 2000). To use the thickness information, the laser range image had to be transformed into a pseudo-X-ray image because the X-ray image represents the absorbed energy as X-ray passed through a material. Because the absorption index of X-ray by poultry meat was unknown (Hubbell and Seltzer, 1997), it had to be obtained through experiment.

X-ray signals are noisy by nature. The noise comes from sources such as photon fluctuation, heat accumulation, and electronic signal amplification and digitization

(Boerner and Strecker, 1988). These noises normally have high frequencies, lack spatial correlation, and are signal dependent (Alison, et al., 1998). The presence of noise in the X-ray image made the absorption index calculation difficult. Various temporal and spatial averaging methods were used to decrease the noise in the X-ray image (Boerner and Strecker, 1988). Depending on the application, other filters such as low pass, median and Gaussian filters were also employed for noise reduction (Chan, et al., 1993, and Mery and Filbert, 2002).

Usually, small patches of grease, remnant skin, and air pockets are found in poultry fillets. Because the densities of these materials are lower than that of meat, their presence causes image intensity variations. Additionally, the muscles from different parts of the chicken and from different chicken species have different compositions. Thus, differences in X-ray absorptions are expected. These variations affect the mapping accuracy of the laser image to the X-ray image.

Laser images also contain noise. Poultry meat is a heterogeneous material with approximately the same density as water. When the laser beam hits the meat, the laser light easily penetrates into the meat and is scattered. The resultant 3D image inevitably contains noise, although the noise is low compared to the real 3D information.

In a normal regression model, one variable is treated as a response variable and the other as a predictor variable. By modeling the expectation of the response variable as a function of the predictor variable, the response variable is related to the predictor variable by the regression equation. The least squares procedure is only used when predictor variables are not subject to any random variations. Because the estimation procedure is based on minimizing the least squares error in one variable, it leads to an error in the other variable, and the estimation error is not orthogonal to the estimated curve. In such cases, the least squares estimate is not optimal even if the errors in both variables are white and Gaussian. However, if the variance of the predictor variable is small compared to the variance of the response variable, or the ratio is known, the least squares method (Norman and Draper, 1998) can still be used. Several methods have been proposed to find an optimal solution to this problem (Weiss, 1989, Qjidaa and Radouane, 1999, and Gibson, et al., 2000). The presence of outliers or heavy-tailed error distribution also affects the performance of the least squares method. In these cases, robust estimation is applied to spot the abnormal points and exclude them from the regression (Zhang, 1996, and Norman and Draper, 1998).

## 7.2 Objectives

The objectives of this study were to analyze the sources of variation and noise in the X-ray and laser 3D images and to develop an image model to find the optimal mapping relationship between the laser 3D and X-ray image. The purpose of the mapping was to produce the pseudo-X-ray image from the laser range image of poultry fillets for the overall integrated imaging detection of bone fragments, as presented in the dissertation by Chen (2003).

## 7.3 Materials and Methods

### 7.3.1 Dual Imaging System Setup

The dual imaging system was designed and built to capture both X-ray and laser 3D images simultaneously. It consisted of two imaging subsystems: an X-ray imaging subsystem and a laser 3D imaging subsystem. The laser 3D subsystem was located entirely in the X-ray chamber. To reduce mismatch of images from both sources by possible slipping of the conveyor belt, the laser beam plane was arranged to overlap the X-ray beam plane. The combined system setup is depicted in Figure 33. For X-ray image acquisition, an X-ray tube and detector were used. They connected to a Matrox Genesis board (Matrox Electronics Systems Ltd., Quebec, Canada). The voltage and current of the X-ray tube were optimally adjusted according to the poultry fillet. To obtain the 3D image, two cameras and two laser beam generators were used. The cameras were connected to a Matrox Genesis LC board (Matrox Electronics Systems Ltd., Quebec, Canada), and they were placed on each side of the structured laser pattern generator to reduce the influence of possible occlusion caused by curvature of the poultry fillet. Both frame grabbers were plugged into a Pentium computer. Both cameras and the laser structure light generator were mounted on a frame that was fixed in the X-ray chamber. The test object was placed on a conveyor belt that traveled under the X-ray and laser light.

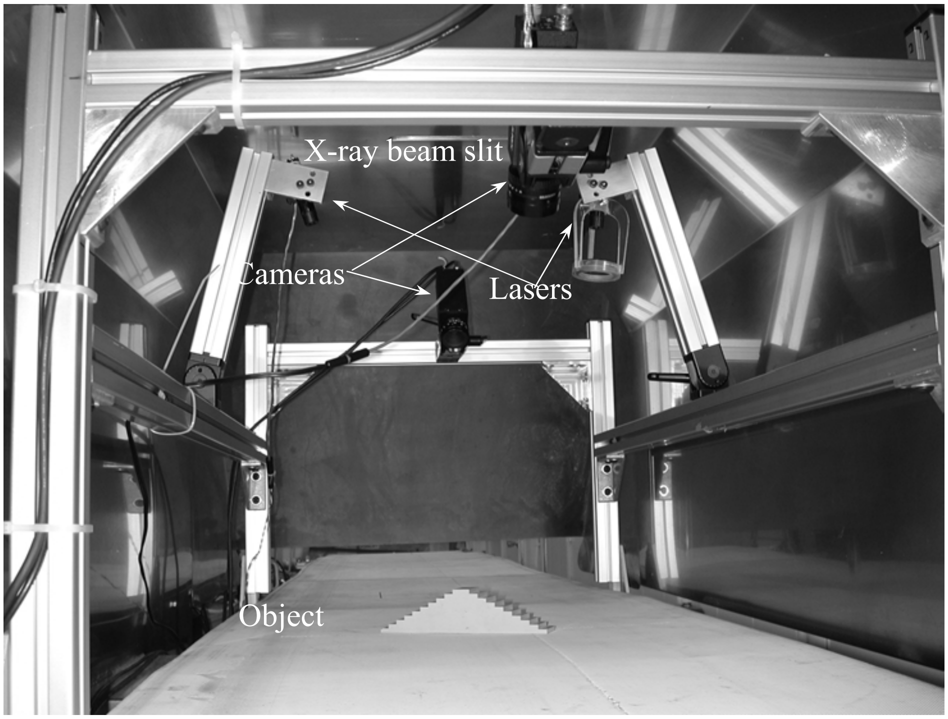

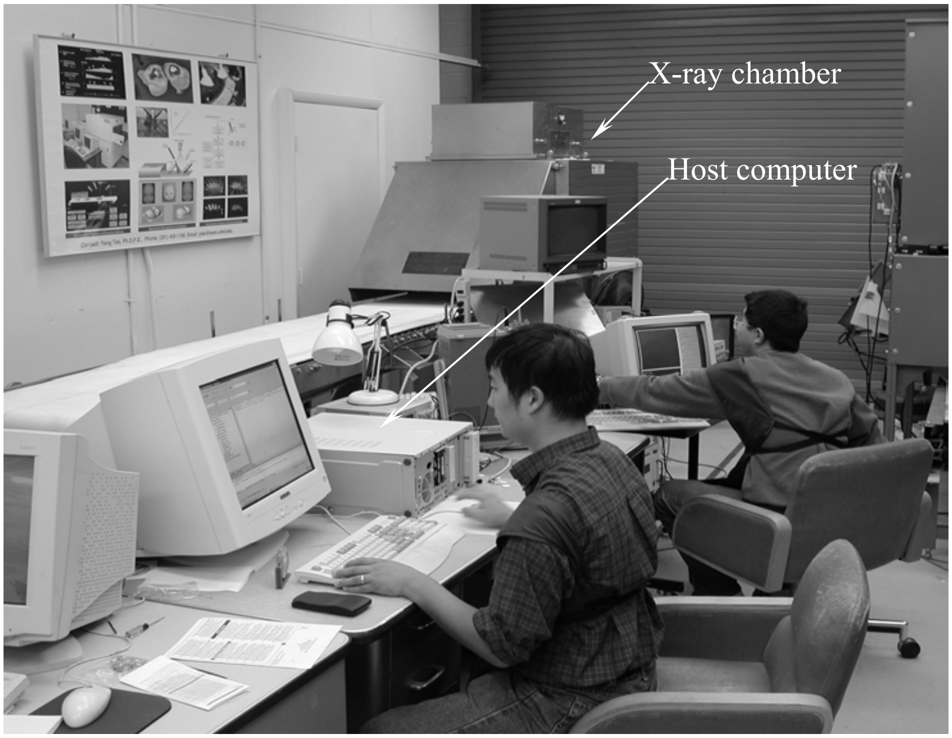

Figure 33. The setups of dual imaging system

The images were grabbed and saved in the computer using software written with Microsoft Visual C/C++ (Microsoft Corp., Redmond, Wash.). The software utilized a Matrox (Matrox Electronics Systems Ltd., Quebec, Canada) library to interface with the frame grabber. It was capable of simultaneously grabbing images from the X-ray and computing the 3D laser images from two cameras. The X-ray image had 12 effective bits. Laser images were grabbed and calculated with 8 bits resolution. The 3D laser images and the X-ray image were fully synchronized by an encoder. The image grabbing and processing was done on-line.

### 7.3.2 Model of X-ray Image Intensity Variations

A typical imaging system can be modeled by (Jain, 1989)

$$v(x,y) = g[w(x,y)] + \eta(x,y)\,, \tag{50a}$$

$$w(x,y) = \int\int_{-\infty}^{\infty} h(x,y;x',y')u(x',y')dx'dy'\,, \tag{50b}$$

where *v(x,y)* is the image obtained and *η (x,y)* is the noise added to the system for various causes. *u(x,y)* is the original image, *w(x,y)* is the image after the original image is convoluted by a image system's impulse response *h(x,y)*, and *g* is the function that models the characteristics of the image system.

Normally, the noise generated in photo-electronic systems can be modeled by

$$\eta = f\left(g(x.y)\right)\eta_1(x,y) + \eta_2(x,y)\,, \tag{51}$$

where $f$ depends on the imaging device, and $\eta_1$ and $\eta_2$ are mutually independent Gaussian white noises with zero mean (Jain, 1989). In this model, the noise comes from two sources: $\eta_2$ represents an additive wideband thermal noise, and $\eta_1$ is multiplicative and signal dependent. Because the detection and recording processes in X-ray imaging involve random electron emission, which obeys a Poisson distribution with a mean value of $g$, $\eta_1$ can be simulated by a Gaussian distribution with its standard deviation proportional to the square root of the signal. In practice, $g$ is replaced by its spatial average to simplify the calculation, so $f$ can be replaced by $\sqrt{\bar{g}}$, where $\bar{g}$ is the spatial average of $g$.

If the X-ray's incident intensity is $I_0$, and travels through a medium with density $\rho$ and thickness t, the exponential attenuation law predicts that the detected X-ray energy has intensity $I$ given by

$$I = I_0 \exp\left[ -\int_T \frac{\mu(x,y,z)}{\rho(x,y,z)} dt \right], \tag{52}$$

where $\mu/\rho$ is the mass-energy absorption coefficient that characterizes the medium (Ryon, et al., 1988). This holds true when the object is a perfect homogeneous material. However, in poultry fillets, when other materials such as grease, air pockets, and various bone fragments are present, then;

$$\begin{aligned} I_R &= I_0 \exp\left\{-\int_T \left(\frac{\mu_1(x,y,z)}{\rho_1(x,y,z)}dt_1 + \frac{\mu_2(x,y,z)}{\rho_2(x,y,z)}dt_2 + \ldots\right)\right\} \\ &= I_0 \exp\left\{-\int_T \left(\frac{\mu_1(x,y,z)}{\rho_1(x,y,z)}dt - \int_{T_2}\left[-\frac{\mu_1(x,y,z)}{\rho_1(x,y,z)} + \frac{\mu_2(x,y,z)}{\rho_2(x,y,z)}\right]dt_2 - \ldots\right)\right\}, \\ &= I_0 \exp(\beta T)\prod_{i=2}^{n} \exp(\Delta\beta_i T_i) \end{aligned} \tag{53}$$

where $T=\sum_{i=1}^{n} T_i$ , $T_i$ is the X-ray path length (54)

$$\beta = -\frac{\mu_1(x,y,z)}{\rho_1(x,y,z)}, \tag{55}$$

$$\Delta\beta_i T_i = -\int\left[-\frac{\mu_1(x,y,z)}{\rho_1(x,y,z)} + \frac{\mu_i(x,y,z)}{\rho_i(x,y,z)}\right]dt_i, \tag{56}$$

and $I_R$ is the X-ray energy that reaches the X-ray detector.

Incorporating the noise (Equations 51 and 53) into the image model (Equation 50) produces

$$I_A = I_0 \exp(\beta T)\prod_{i=2}^{n} \exp(\Delta\beta_i T_i) + \sqrt{\bar{I}_R}\eta_1 + \eta_2, \tag{57}$$

where, $\bar{I}_R$ is the spatial average of $I_R$, $I_A$ is the actual signal X-ray detector received.

From Equation 57, both the noises and foreign inclusions will cause X-ray image intensity variation. The variation due to foreign inclusions was greater than compared to the other two variation sources. From Equation 53, it can be observed that, when the same bone fragment is placed in a fillet of varied thickness, the X-ray image intensity variation is smaller when the bone is in the thicker part of the meat.

However, in the thinner part of the meat, the X-ray image variation level is larger. This suggests that different thresholds might be used to differentiate the bone fragments from meat with thickness variation. Otherwise, transformation is needed to ensure data uniformity.

### 7.3.3 Model of Laser 3D Range Image

Noise also occurs in laser 3D images. In laser 3D images, noise mainly comes from calculation error caused by scattering. Scattering is a phenomenon that occurs when strong coherent light strikes a medium that contains components that have different refractive indices and whose sizes are on the same scale as the light wavelength. It is very difficult to describe scattering accurately. Although the image quality is corrupted by scattering, thickness information can still be recovered by sub-pixel techniques that were described in previous chapters. The noise, some caused by scattering, can be considered as a Gaussian white noise with variance $\sigma_\varepsilon$ and zero mean. Then the 3D image is described as

$$T_A = T(x,y) + \delta \ , \tag{58}$$

where, $T_A$ is the obtained image intensity, $T(x,y)$ is the original image, and $\delta$ is the additive Gaussian noise.

### 7.3.4 Laser 3D Image to X-ray Image Mapping

It is difficult to measure the attenuation index when an X-ray passes through a poultry fillet unless the meat block is of a uniform height. As an alternative, least squares procedures are used to obtain the attenuation index. Inevitably, noise has to be considered in the regression. Due to the fan beam effect of X-ray imaging, the $T$ in Equation 58 is replaced by the actual X-ray path instead of the meat thickness.

Because the noise is small, Equation 60 is equal to

$$I_A - \Delta I_A = I_0 \exp(\beta T) \prod_{i=2}^{n} \exp(\Delta\beta_i T_i), \tag{59}$$

where $\Delta I_A = \sqrt{\bar{I}_R}\eta_1 + \eta_2$, (60)

Applying a logarithmic transformation to both sides of Equation 59, we have

$$\ln(I_A - \Delta I_A) = \ln(I_0) + \beta T + \sum_{i=2}^{n} \Delta\beta_i T_i. \tag{61}$$

Expanding the left side of Equation 61 by Taylor expansion, incorporating Equation 60 and making a proper transformation, it now becomes;

$$\ln(I_A) = \beta_0 + \beta T + \sum_{i=2}^{n} \Delta\beta_i T_i + \frac{\sqrt{\bar{I}_R}}{I_A}\eta_1 + \frac{1}{I_A}\eta_2, \tag{62}$$

where, $\beta_0 = \ln I_0$. Furthermore, $I_A$ can be replaced by its spatial average $\bar{I}_R$. It can further be simplified as

$$Y = \beta_0 + \beta T + \varepsilon \,, \tag{63}$$

where $Y=ln(I_A)$,

and $\varepsilon = \sum_{i=2}^{n} \Delta\beta_i T_i + \frac{1}{\sqrt{\bar{I}_R}}\eta_1 + \frac{1}{\bar{I}_R}\eta_2 \,,$ (64)

However, for use in the bone fragment detection application, it may be incorrect to assume that $\varepsilon$ follows normal distribution.

Incorporating Equation 58 into Equation 63 gives

$$Y = \beta_0 + \beta T + (\varepsilon - \beta\delta) \,, \tag{65}$$

where $\delta \sim N(0,\sigma_\delta)$. Because the errors $\varepsilon$ and $\delta$ are independent, they are not correlated and $cov(\varepsilon,\delta)$ should be zero.

As mentioned before, small patches of grease, tissue and skin are present in the poultry fillets. The absorption and density of these materials is lower than that of meat muscle. On the contrary, bone fragments and other items such as metal have higher densities and higher absorption indices compared to the muscle. Thus, it is not difficult to find that the residuals are not normally distributed and may contain outliers. In this case, a weighted least squares is adopted method to robustly find the relation between the X-ray and 3D laser images.

Using the matrix form of Equation 65, the robust estimation can be deduced from (Fuller, 1987)

$$
\begin{aligned}
&Y = T\beta \\
&WY = WT\beta \\
&T^T WY = (T^T WT)\beta \qquad , \\
&(T^T WT)^{-1}(T^T WT) = (T^T WT)^{-1}(T^T WT)\beta \\
&\beta = (T^T WT)^{-1}(T^T WT)
\end{aligned}
\tag{66}
$$

where $Y$ is an (n×1) vector of observations of the response variable; $T$ (n×2) contains the n observations on the p predictors (including the intercept term); $\beta$ (2×1) is the regression vector to be estimated, and

$$
W = \begin{bmatrix} w_1 & 0 & 0 & 0 \\ 0 & w_2 & 0 & 0 \\ . & . & . & . \\ 0 & 0 & 0 & w_n \end{bmatrix}, \tag{67}
$$

where $W$ is a diagonally weighted matrix. W depends on the variance of that point, and can be expressed as

$$
w_i = \frac{\psi\{(Y_i - T_i\beta)/s\}}{(Y_i - T_i\beta)/s}, \tag{68}
$$

where $s$ is a scale factor and

$$
s = median\left|e_i - median(e_i)\right| / 0.6745, \tag{69}
$$

is selected as suggested by Andrews et al. (1972). $e_i$ in Equation 69 is the residual. The biweight function, due to Tukey (1977), was adopted as the $\psi$-function.

$$
\psi = \begin{cases} \dfrac{e}{s}\left(1 - \left(\dfrac{1}{c}.\dfrac{e}{s}\right)^2\right)^2 & if(\dfrac{e}{s}) \le c \\ 0 & if(\dfrac{e}{s}) \ge c \end{cases}, \tag{70}
$$

with $c = 5$.

The robust estimation procedure was iterative and proceeded in the following steps:

1) Apply ordinary least squares to the data.
2) Calculate $W^0$.
3) Based on $W^0$, calculate $\beta$.
4) Re-compute $W^1$ based on newly calculated $\beta$.
5) Repeat until $W^k$ converges.

A detailed description of the robust regression algorithm can be found in Farebrother (1988) and Norman and Draper (1998).

## 7.4 Results and Discussion

### 7.4.1 Reason for making the transformation

At the beginning of the mapping operation, a transformation needs to be made to the X-ray image. In a normal regression model

$$Y = X\beta + \varepsilon, \tag{71}$$

where ε is one dimensional vector of error terms, which are to be independent and identically distributed (IID). Using the least squares method, the function

$$f(\beta) = (X\beta - Y)^T (X\beta - Y), \tag{72}$$

is minimized. Its solution is simply given by

$$\beta = (X^T X)^{-1} XY. \tag{73}$$

The result is not biased and is the maximum likelihood estimation only when 1) there are no outliers, which is a data point that is far away from the rest of the data, 2) residuals are uncorrelated (i.e. $E(\varepsilon_i\varepsilon_j)=\sigma_i^2\delta_{ij}$), and 3) variances are constant (i.e. $\Lambda_{\varepsilon_i}=\sigma^2\forall i\in[1,...,n]$) (Norman and Draper, 1998).

For this application, the relationship between the X-ray signal and laser signals is shown by Equation 52. Using Taylor expansion

$$\Delta f = I_0\exp(\beta T)\beta\Delta T-\Delta Y+O(\Delta T^2+\Delta Y^2), \tag{74}$$

Ignoring the second and larger order terms, the variance becomes

$$\Lambda_{\varepsilon_i}=E(\Delta f)^2=(\exp(2T)+1)\sigma^2, \tag{75}$$

Obviously, the variance is not the same at every point. Thus the least squares method does not yield the optimal solution, so a linearization (Equation 61) is necessary.

### 7.4.2 Residual non-normality check

In the previous discussion, it was assumed that the error distribution was not normal. To check whether that assumption was correct, two plots were used. The first one was a residual histogram, and the second one a normal plot (Barnett and Lewis, 1994).

The residual histogram plot (Figure 34) showed a normal distribution. However, from the normalized plot (Figure 35), it was clear that the residual was short tailed, thus robust estimation had to be used to make the resolution optimal.

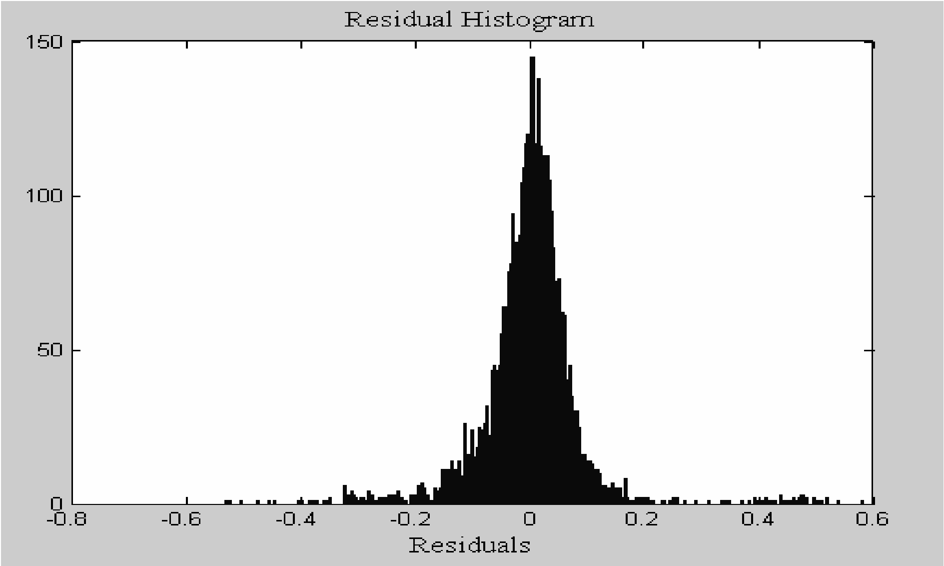

Figure 34. A typical distribution of residual errors of the X-ray intensity image and the pseudo X-ray image produced from the laser range image.

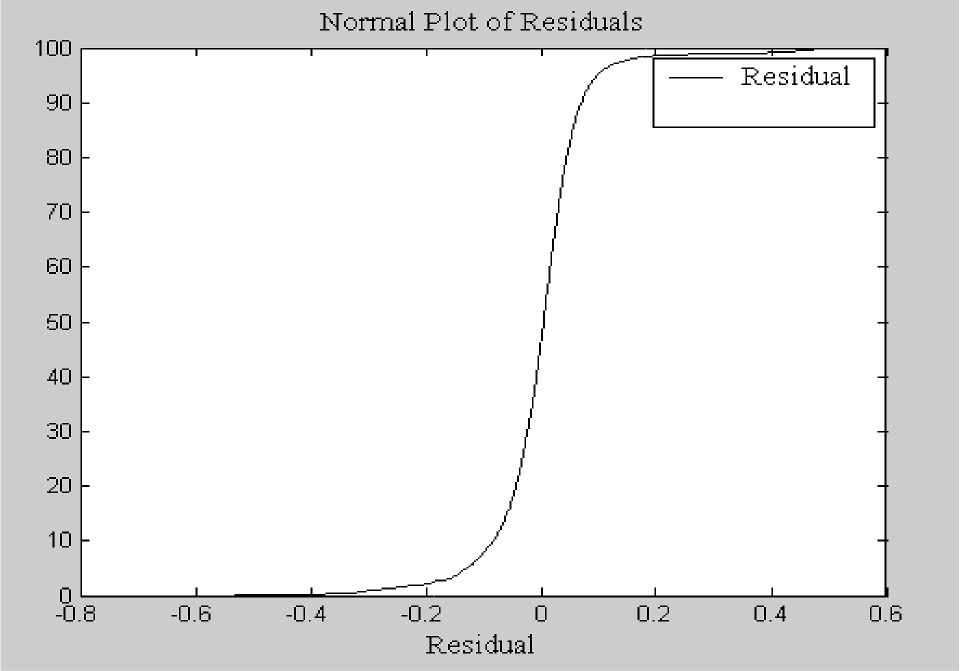

Figure 35. Normalized plot of accumulative residual errors of Figure 34 (normal plot to a sale of 100).

### 7.4.3 Experimental Results

One hundred and thirty chicken fillets were imaged and processed in this experiment. All of the fillets were directly obtained from a poultry processing plant. They were fresh cut and de-boned, but not trimmed, so that the meat condition and bone fragment size and distribution were comparable to an actual inspection process. In the experiment, three to five fillets were placed on the conveyor and consecutively scanned as a batch. To each piece of meat, the mapping relationship was found by the method mentioned before. Based on this relationship, the laser 3D image was transformed into pseudo-X-ray image, and the pseudo-X-ray image was compared with the original X-ray image. Before processing, the system was fully calibrated to ensure the accuracy of the observed data.

Figure 36 shows a sample obtained from the designed system. In Figure 36(b), there were air pockets and small bone fragments in the meat. Because the absorption index of air was lower than that of the meat, the air pockets had higher intensities in the image. The bone fragments appeared to be dark in the X-ray image. Reflected in scatter plots below (Figures 36(c) and 36(d)), the points corresponding to bone fragments were far below the regression line; whereas the points reflecting air pockets were above the regression line. Also from these two figures, it can be clearly seen that the data was scattered in a “funnel” shape, i.e. one end was wider than the other. This was because X-ray noise was proportional to signal strength itself. If the signal was strong, as was the case when the meat is thin, the noise was high. The presence of

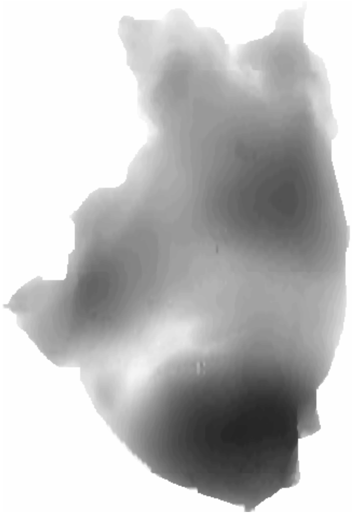

(a)

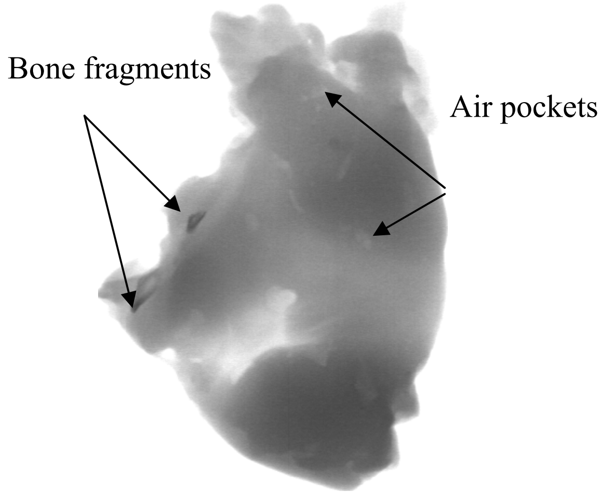
Bone fragments
Air pockets

(b)

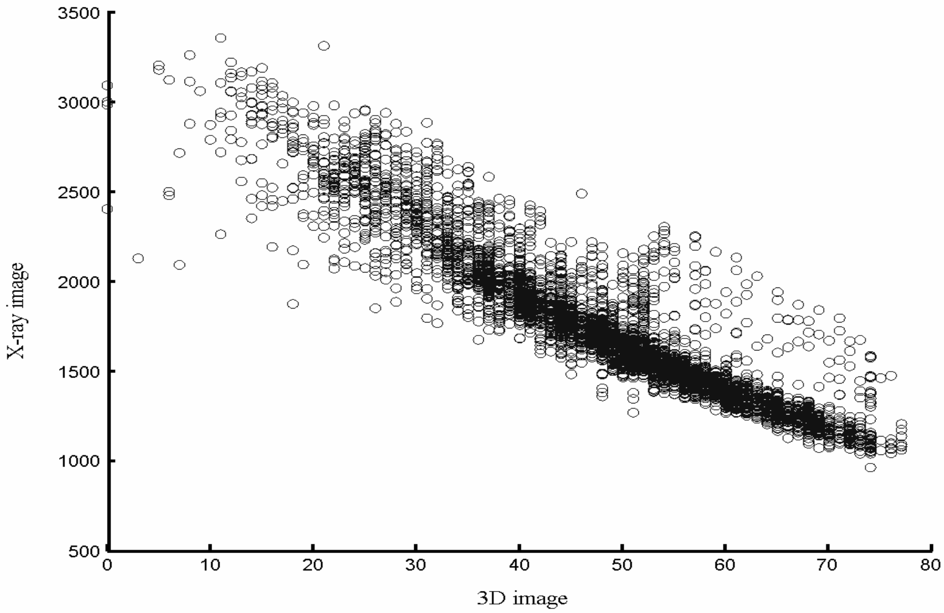
3500
3000
2500
2000
1500
1000
500
X-ray image
0
10
20
30
40
50
60
70
80
3D image

(c)

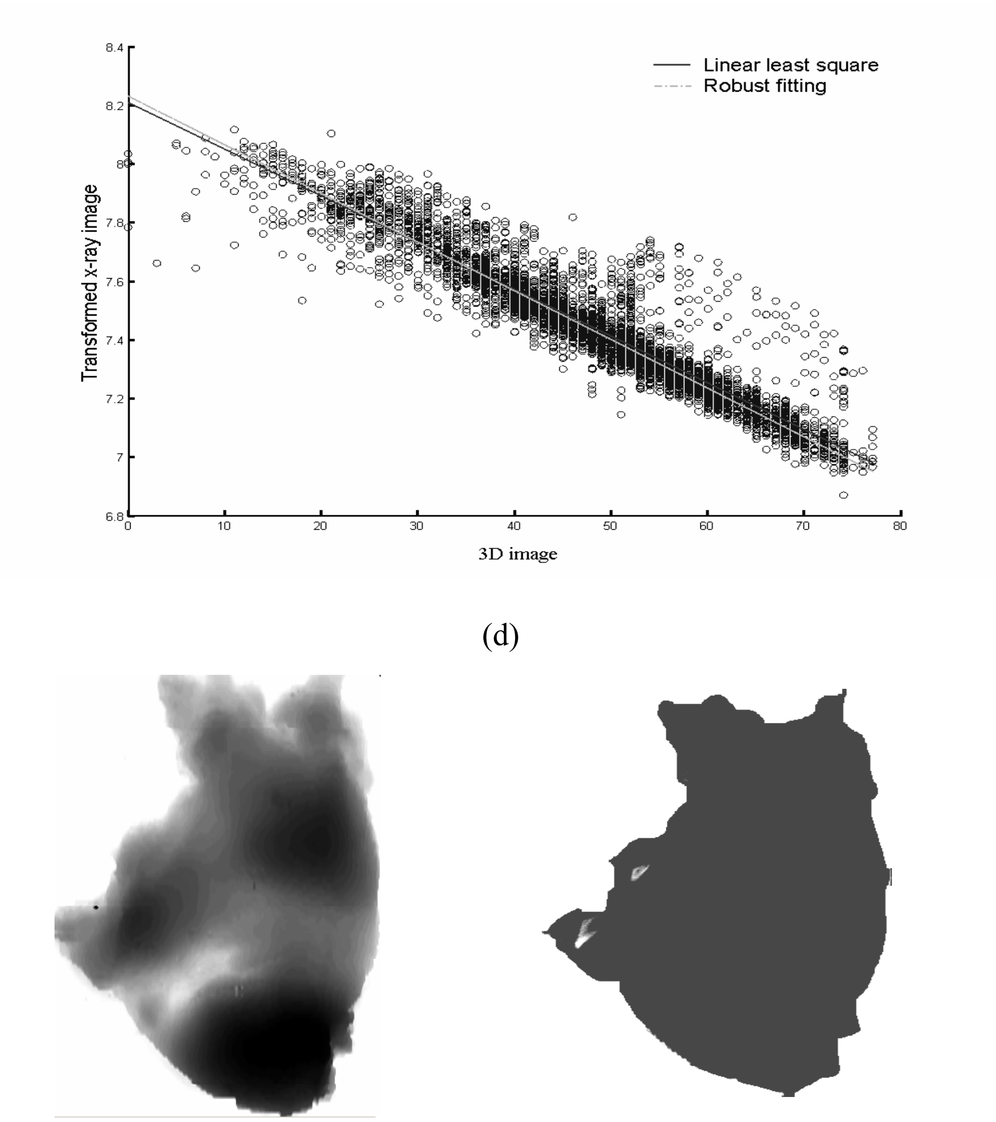

(d)

(e) (f)

Figure 36. Images and results of the whole procedure. (a) Reversed 3D image, (b) original X-ray image, (c) scatter plot of X-ray and 3D image intensity without transformation, (d) scatter plot of X-ray and 3D image intensity after transformation. The dashed line is the robust fitting result, and the solid line is the regular linear fitting result, (e) pseudo-X-ray image from 3D image, and (f) compensated X-ray image whose intensity variation was reduced.

this effect makes linearization of the X-ray signal essential in obtaining optimal results. Transformations from nonlinear to linear forms also suppressed noise. In Figure 36(d), ordinary least squares were obviously influenced by outliers, while robust estimation followed the bulk of the data and was not strongly biased towards outliers. After applying the robust estimation, the mapping relationship between the 3D and X-ray images was known and 3D image could then be transformed to pseudo-X-ray image (Figure 36(e)). When X-ray and pseudo-X-ray images were combined, the intensity variation of the resulting image due to thickness variation was reduced.

Ideally, the intensity of the combined image should be zero. Because of the presence of the noise, the actual image intensity was not zero. To all the combined sample images, their average intensity was 23.7307 and their standard deviation was 29.6. Because the X-ray image had 12 bits depth, the noise level occupied only 1.5% of the total image dynamic range (Appendix J and I).

## 7.5 Conclusion

Noise models of X-ray images and 3D laser images were developed and analyzed. The noises in X-ray image were not uniform. The X-ray noise came from the imaging device, heat accumulation, variations in the inspected material, and inclusion of foreign objects. The noise was proportional to the signal strength and was difficult to eliminate from the X-ray images. In the laser 3D image, the noise mainly came from calculation errors due to light scattering. The distribution of residuals of the X-ray image was “shorter-tailed” than normal, while residuals of the 3D images were modeled as Gaussian white noise fields with zero mean. The relationship between X-ray image intensity and thickness of an object is nonlinear by nature. It was necessary to transform the X-ray image to a linear form.

Because the X-ray noise was short tailed and contained outliers and the X-ray image intensity was not linear with the thickness, using an ordinary least squares regression method could not get an unbiased solution. Therefore, a robust fitting procedure was important to fit the data set. The robust fitting successfully revealed the relationship between the X-ray image and 3D information. The pseudo-X-ray image transformed from 3D image can be used to reduce the X-ray image intensity variation due to the thickness variation. The residual image’s intensity average was 23.7302 with standard deviation of 29.6, and only occupied 1.5% of the dynamic range of the X-ray image. This built the foundation for the performance of a combined bone fragment detection system.

# Chapter 8

# SOFTWARE AND HARDWARE DEVELOPMENT

## 8.1 Introduction

The designed bone fragment detection system was a very complicated system. It consisted of X-ray and the laser 3D imaging systems. Consequently, the system had to be able to handle the data coming from both sources and finish all calculations in a very short time. In the dual imaging system, the desired conveyor belt speed was 0.2 m/sec. If the 3D image resolution was one millimeter in the conveyor belt moving direction, the system had to be able to process an image frame, perform calculations, combine the data from both sources and detect the bone fragments in 1.6 milliseconds, which posed a big challenge to the software, hardware, and operating system.

In this chapter, the real-time characteristics of Windows NT, and the architecture of the image grabber and data flow structure are introduced. At the end of the chapter, results are discussed of tests performed to make sure the designed system was capable of performing all these operations at the speed desired.

## 8.2 Window NT Real-Time Feature Introduction

Windows NT has been adopted due to its portability, reliability and robustness, (Curster, 1993). Windows NT offers users many conveniences, including an easy-to-use graphical interface interoperability with Windows-based applications, network communications, easy information access, and powerful information processing capabilities. In addition, its preemptive multitasking and multithreading features meet some of the real-time requirements of a variety of industrial applications. Therefore, Windows NT has been considered as an alternative for operating systems used for real-time applications.

### 8.2.1 Architecture of Windows NT

Windows NT is a complex operating system. Figure 37 illustrates the architecture of Windows NT. It is divided into two parts: the user-mode portion and the kernel portion. In the user-mode portion, there are various subsystems. Each provides a user interface and is fundamental to the system's operation. However, the application that runs under the user mode has a limited set of available interfaces and limited ability to access system data. The kernel mode is composed of five modules: Windows NT executive, Windows NT kernel, hardware abstraction layer (HAL), device driver, and windowing and graphics system (Solomon, 1998). This part of the operating system has the ability to access the system data, and some parts of it can communicate directly with the hardware.

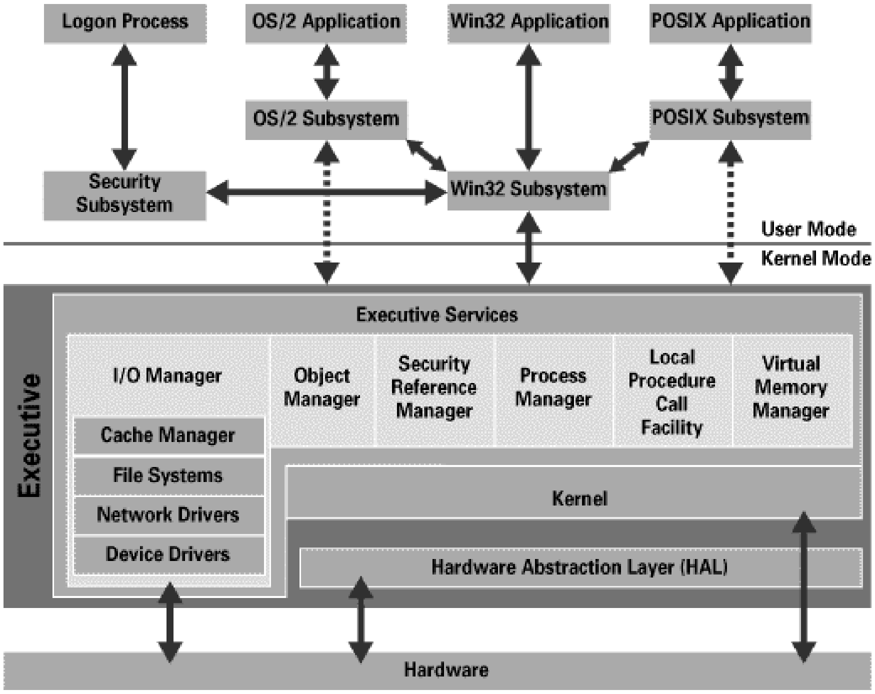

Figure 37. The Windows NT architecture (Solomon, 1998).

The design of Windows NT borrows concepts both from the layered model and the client/server model (Solomon, 1998). In the client/server model, the client and server communicate through a message-passing facility. First, the client sends a message to the message-passing facility. Then the message is dispatched to the server, and the server performs the operation and returns the results to the client through the message-passing facility. Each server can be developed separately as long as the message interface is clearly defined. Updates and upgrades to the operating system can be easily managed, and it is more likely to be reliable because smaller, independent modules are easier to program than large, interconnected complex systems. In the Windows NT environment, application programs are clients, and protected subsystems are servers. The application program clients send messages to the protected subsystem servers through the NT executive, which provides a set of shared services for all the servers. The servers again reply though the NT executive.

### 8.2.2 Real-time Feature of Windows NT

Windows NT is known as a general-purpose operating system. However, it provides certain features for real-time applications.

Interrupting is used by a real-time application to ensure that external events are noticed by the operating system. Responses to interrupt are critical to real-time applications. Within Windows NT, there are 32 possible interrupt levels, as shown in Table 6. Interrupts are handled on a preemptive basis, that is to say, when a higher level interrupt occurs, all executions at lower interrupt levels are suspended and execution begins immediately on the higher level interrupt request. Processing continues until the higher level interrupt is completed or an even higher level interrupt occurs. In this way, the operating system ensures that the higher level interrupt always has the privilege to run, allowing a quick response to the external event.

Within Windows NT, user applications are defined as processes. A process is composed of several threads. Associated with the process property is its priority class that defines the basic priority at which the application will run. There are four classes, or 32 priority levels, of which 16 are reserved for the operating system and real-time processes. Among them, the zero (idle) is the lowest, while 31 (real-time time critical)

Table 6. Windows NT interrupt levels (Custer, 1993).

| Interrupt Level(s) | Definition |
|---|---|
| 31 | Hardware error interrupt |
| 30 | Power-fail interrupt |
| 29 | Inter-processor interrupt |
| 28 | Clock interrupt |
| 12-27 | These levels map to the traditional interrupt levels 0-15 |
| 4-11 | These levels are not generally used |
| 3 | Software debugger interrupt (DPC) |
| 0-2 | Reserved for software-only interrupts |

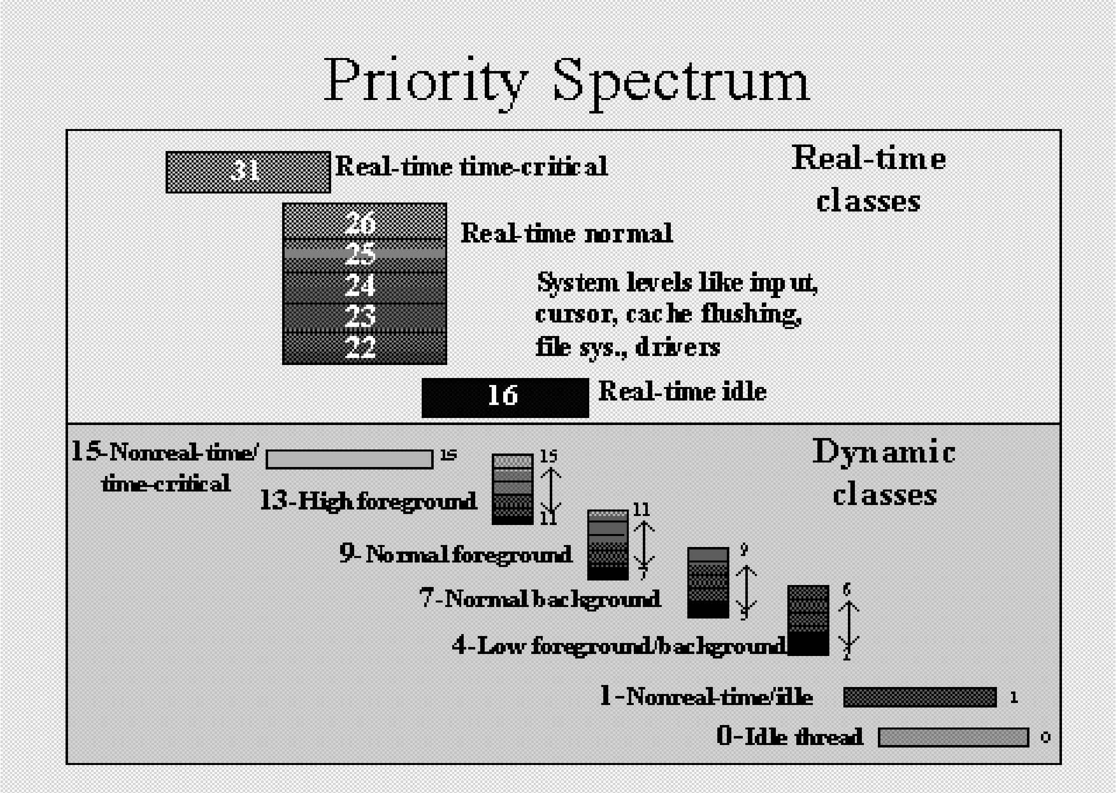

Figure 38. Windows NT priority spectrum (MSDN, 1998).

is the highest level. Every process has a base priority class. As shown in Figure 38 below, there are seven priorities allocated to real-time applications. Real-time applications can run with a base priority class of 31 (time critical), 24 (normal), or 16 (idle). Typically, real-time processes run at priority 24. Other applications (dynamic classes) have a base priority class of 15, 13, 9 (normal foreground process), 7,4,1, or 0.

The priority of the process thread changes slightly around the base priority level. For example, a process running at real-time priority 24 can have threads that run from classes 22 to 26, depending on each independent priority. These threads will always stay within the real-time priority class. In general, real-time processes have priority over almost all other activities or system events. Moreover, Windows NT contains features such as multitasking and periodic callback routines that also support real-time applications.

However, the complexity of Windows NT introduces some unpredictability and time latency to the application that severely affect its real-time characteristic. Suppose that NT detects an interrupt or an exception, the processor stops what it is doing and lets the trap handler deal with it. After the trap handler determines the condition, it transfers control to the Interrupt Service Routine (ISR) if the interrupt is time-critical. Once the ISR is running, it is not interrupted until the end of its service routine, unless a higher level interrupt occurs. If the second condition occurs, the system will save some data about the interrupt. This will cause some unpredictable latency. In the same way, the use of deferred procedure calls (DPC) introduces another unpredictable delay. Windows NT mainly uses DPC to handle the interrupts generated by the device driver. Also, the kernel employs them to handle the time-quantum expiration. The interrupt request levels (IRQL) of DPC belong to the third interrupt level. The isolations of ISR and DPC are beneficial to interrupt latency, but are harmful to the thread latency. The DPC routines that are waiting to execute are stored in a kernel-managed first-in-first-out queue called the DPC queue. So, all DPC have the same priority level, but can be preempted by an interrupt. As a result, the interrupt is responded to immediately, but the executions of threads of the DPC are delayed. Furthermore, it is possible that an interrupt occurs during the execution of the kernel. Typically, user level threads cannot preempt the thread which is executing in kernel mode. During the process of execution of the kernel thread, the processor's current IRQL can be changed. Thus, some interrupt can be allowed to execute. If the IRQL is too low, even an unimportant interrupt could execute, and thus could adversely affect a real-time priority user level thread.

Windows NT is a general-purpose operating system. Some helpful features in the operating system are harmful to real-time applications. For example, Windows NT is built around a virtual memory (VM) system. Under normal conditions, it resolves the problem encountered by general applications that need large amounts of RAM to run. But if the process is very big, the processing speeds become very slow. It is intolerable for real-time applications. The cache management is the same. For the general operating system, it increases the average system performance, but it introduces an element of timing unpredictability in a real-time environment.

### 8.2.3 Reported real-time performance

A series test was performed to evaluate under what condition the Windows NT could be used as a real-time operating system (Timmerman, 1998, Jones and Regehr, 1999; and Ramamritham and Shen, 1998). Among these tests, tasks such as the I/O interference, time taken to process/thread system calls, supported clock rates, interrupt handling, and semaphores were examined. The time used for each task was different. However, the minimum time needed was ten to several thousand nanoseconds; the maximum time needed was several thousand nanoseconds to several hundred milliseconds; and the mean general latency was several hundred microseconds. Thus, for normal millisecond level soft real-time applications, Windows NT was fully capable.

## 8.3 Hardware Architecture

In this application, a Genesis LC frame grabber was used. The Genesis LC board was a high-throughput PCI grabber for color or monochrome acquisition. This board was capable of simultaneously capturing the data to an integrated display and transferring the data to the host computer. Its architecture is shown in Figure 39.

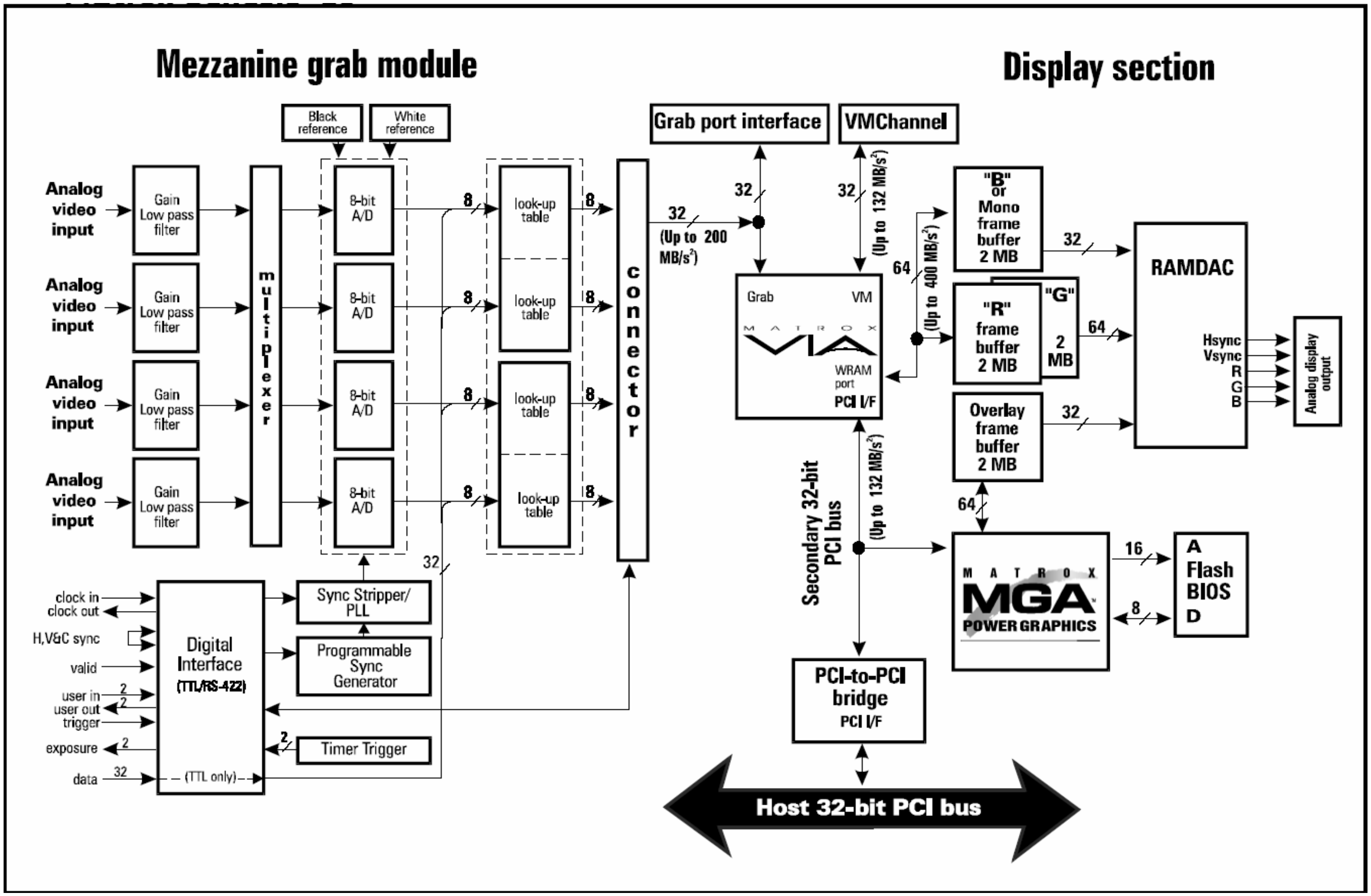

Figure 39. Architecture of Matrox Genesis-LC frame grabber (Matrox).

The board was composed of two parts: a Mezzanine grab module, which was mainly used to grab both digital and analog videos, and a display module. It was a 32 bit board with a 33MHz bus-master. To conveniently connect with other image boards, it had a grab port interface and VM channel, making the data exchange with other boards very easy without consuming any PCI bus bandwidth. There was also 8 M memory on the board, and although it was mainly designed for display, it could be adapted using software to be used as an onboard buffer to facilitate the double buffer which is very important in real-time grabbing and processing. There were programmable look-up tables on the board. Both the onboard memory and look-up tables provided the possibility to do parallel calculations.

## 8.4 Data flow Design

In the proposed system, two Pulnix TM-6703 cameras capable of taking up to 200 frames per second were used. The system was set to capture 100 frames per second. To make the depth detector work at that speed, the data flow was designed with the capabilities of both the operating system and image grabber in mind.

To decrease access times to the host, a ring buffer was set up on the frame grabber. The ring buffer, also called a circular queue, worked in the first-in-first-out (FIFO) manner. The ring buffer was a fixed size buffer with two pointers. One pointer introduced to the place where the data was to be written in, and the other pointed to

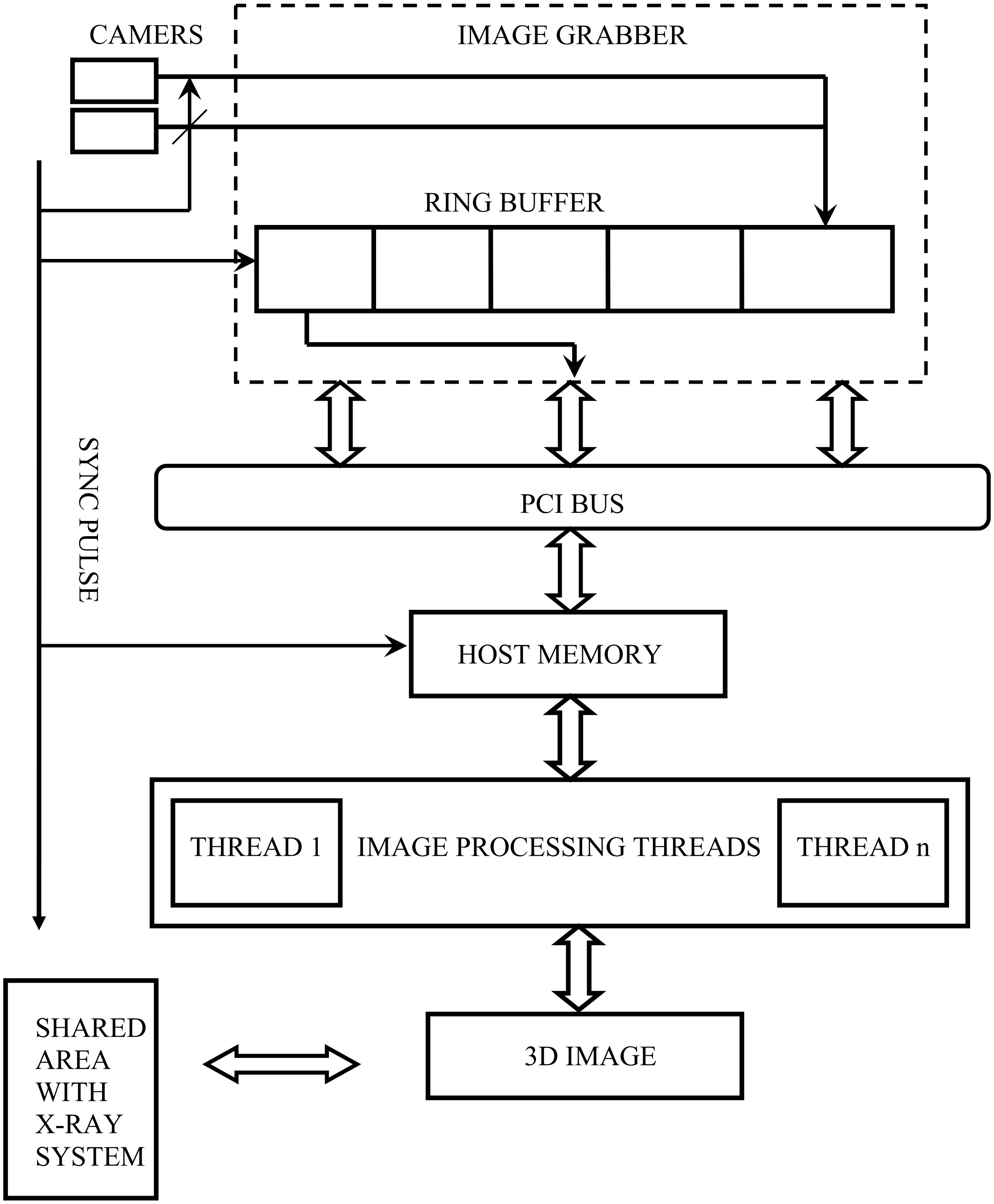

Figure 40. Illustration of data flow of laser range image generation.

place where the data was to be read out. Because the write-pointer and read-pointer pointed to different positions, it was safe even if two processes reached the ring buffer simultaneously. The grabbed image was stored on the buffer first. Then, when a copy command was issued by another process, the buffered image was transferred to the host memory, where the images were processed and depth information was calculated to be used by the X-ray subsystem.

Since the frequencies of the synchronization pulse were not fixed and the time needed to process every image was not predictable, it was possible that the processing speed was faster than the grabbing speed, in which case, the system would overrun. If the grabbing speed was faster than the processing speed, the processing was not able to keep pace and some data would have been lost. To deal with the second situation, multiple-thread technology was used in the software design. If the existing thread could not finish the work in the synchronization interval, another thread was generated that took over the task, and the existing tasks co-existed until each task was finished. The tasks had their own resources and shared the CPU time. In this system, communication between the X-ray and laser subsystems was achieved through a global structure variable. The two subsystems were designed as two parallel and independent processes. When the 3D image was ready, it was stored in the global data area, and the X-ray subsystem could fetch it when necessary. The global data area was also arranged as a ring buffer, so even when X-ray and laser subsystems accessed the data simultaneously, a deadlock would not occur.

### 8.4.1 Critical Speed Measurement

As shown in Figure 40, the data was processed using the following procedure. First, the data was copied from the image grabber to host memory; then, the data was sent to a thread to process the image. Based on this structure, there were two uncertainties in the system that could possibly make the system not respond not in a timely manners. One was in the process of copying the data from the board to host memory. Since the PCI bus was also used by other I/O operations, it was possible that the PCI could be occupied by other tasks and delay the copying request. However, it was possible to decrease its influence by increasing the ring buffer size and making other adjustments to the software. The copying speed was tested when the PCI bus was in idle, medium traffic, and heavy traffic conditions. Two images were used to test the performance. One image was 120 kilobytes and the other was 9216 kilobytes. The time used to copy these two images is shown in Table 7. Although the second image is eight times larger than the first one, the time used to transfer the image was almost the same under the idle condition. However, in the heavy traffic condition, it required 21 microseconds on average to copy the small image to the host memory and 135.6 microseconds to copy the large image. Usually, when the system was working under the medium traffic condition, the time spent to transfer the images was about two times that of the idle condition. Obviously, time was saved if the bigger buffer was used.

I/O (Input/Output) operations mentioned above were the tasks that would use the PCI bus and memory, such as the communication between the computer and its users, its storage devices, the outside world, or other computers (via a network). Here the I/O idle was defined as the situation when only minimum operations were done to access I/O, such as mouse and keyboard activity. The medium condition was when large files were being saved, opened and copied from one place to another. Under the heavy traffic condition, large files were being transferred from one computer to another device using both the PCI bus and memory access bandwidths.

Table 7. Time used to transfer an image from the board to the host memory.

| File Size (kilobyte) | Time Used (μ second) | Computer Load | | |
|---|---|---|---|---|
| | | Idle | Medium | Heavy |
| 120 | Average | 11.18 | 12.18 | 21 |
| | Worst | 17.65 | 33.093 | 63.84 |
| 9216 | Average | 12.64 | 25.93 | 135.6 |
| | Worst | 13.52 | 48.32 | 183.6 |

The second time delay concern was during the thread generating or switching. Such typical delays are shown in Table 8. The NT operating system can respond at the millisecond level. The thread switching time under different conditions was tested. Under normal conditions, the time consumed in thread switching in the worst case was 0.15 microseconds. Under heavy load conditions, the time needed was 266.1 microseconds. When the whole task's priority level was increased, the time used in thread switching was not reduced too much. When the thread priority was set to real-time, the program froze and no data were measured. Overall, under the medium load, thread spawning/switching did not have much influence on the system performance.

Table 8. Thread spawning/switching time measurement.

| Task Priority | Thread Priority | Time (μ second) | Computer Load | |
|---|---|---|---|---|
| | | | Medium | Heavy |
| Normal | Normal | Average | 0.121 | 24.5 |
| | | Worst | 0.15 | 266.1 |
| | High | Average | 0.117 | 23.2 |
| | | Worst | 0.132 | 224.3 |
| | Real Time | Average | ---- | ---- |
| | | Worst | ----- | ------ |
| High | Normal | Average | 0.115 | 21.8 |
| | | Worst | 0.16 | 250.3 |
| | High | Average | 0.112 | 20.9 |
| | | Worst | 0.162 | 212.5 |
| | Real Time | Average | ----- | ----- |
| | | Worst | ------ | ------ |

## 8.5 Conclusion

In the bone fragment system, the on-line process requirement, the NT's real-time features, the architecture of the image grabber, and the data flow were analyzed.

Although Windows NT was designed as a general operating system, it can be used in the designed system.  The Genesis image grabber provided helpful features for parallel processing.  Based on the tests, the time needed to copy a big image and small image from the image grabber to the host memory was almost the same, and thread spawning/switching time was negligible.  Based on these results, laser 3D imaging can be implemented in real-time.

# Chapter 9

# OVERALL CONCLUSIONS

In conclusion, the designed laser 3D system met the desired requirements. The following conclusions were drawn from the research:

1. The laser range image profile can be calculated with reduced scattering influence and the accuracy of the profile was 0.14 mm by 0.14 mm;
2. The laser 3D and X-ray systems were calibrated with sub-pixel accuracy, which is an important factor in finding the mapping relation between the laser and X-ray image;
3. The algorithms of converting laser range image to pseudo x-ray image were found effective. The residual image's intensity average is 23.7302 with standard deviation of 29.6, and only occupied 1.5% of the dynamic range of the X-ray image. This method built the foundation for the performance of a combined bone fragment detection system.
4. Finally, the laser 3D system developed was able to provide the accurate pseudo X-ray image for real-time detection of bone fragments using combined X-ray and laser ranging imaging techniques.

# Chapter 10

# SUGGESTIONS FOR FURTHER STUDY

In the thesis, a dynamic laser 3D imager for poultry products was designed. Future work needs to be done in the following areas:

1. Since the X-ray signature of cartilage bone is similar to that of normal meat, it is difficult to classify cartilage bones. Another method needs to be developed to resolve this problem.
2. Although the whole system calibration was very accurate, it was not fully automatic. A fully automatic method needs to be developed.
3. Currently, a prototype one-lane system was developed. A multi-lane system needs to be developed without reducing the speed and resolution.
4. Bone fragment tracking and ejecting methods need to be developed, for use after a bone fragment is detected.
5. Scattering is a very complicated phenomenon, and it has been broadly used in the biomedical area. Possible applications in food and agricultural products need to be investigated.

# APPENDICES

## Appendix A

### Spectral response

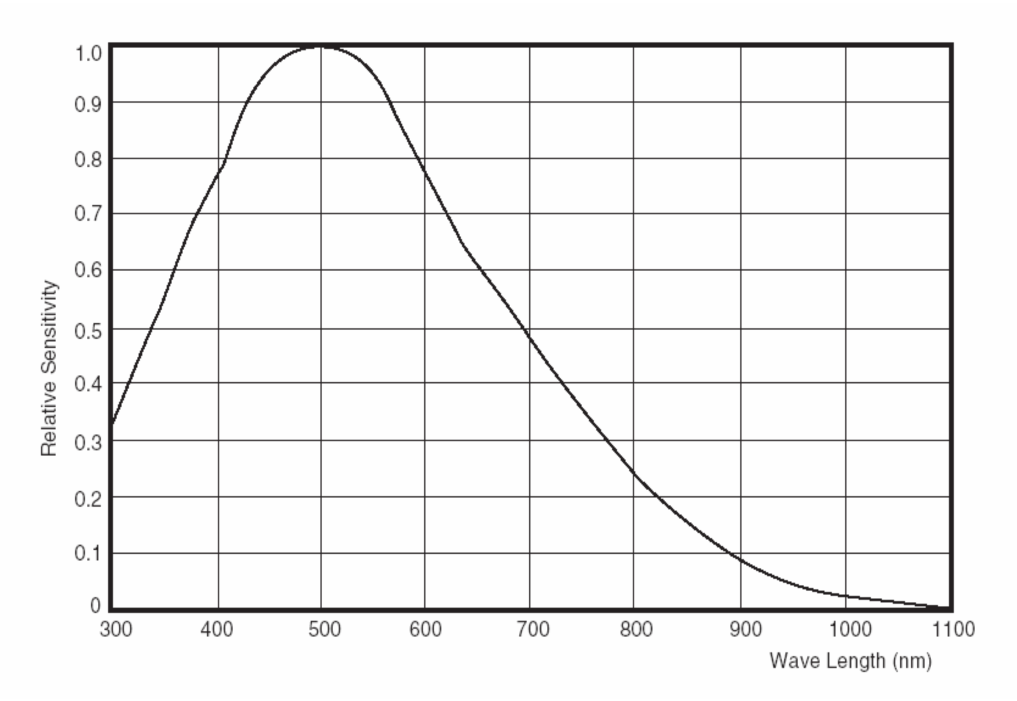

Figure 41. Pulnix TM-6703 camera spectral response

## Appendix B

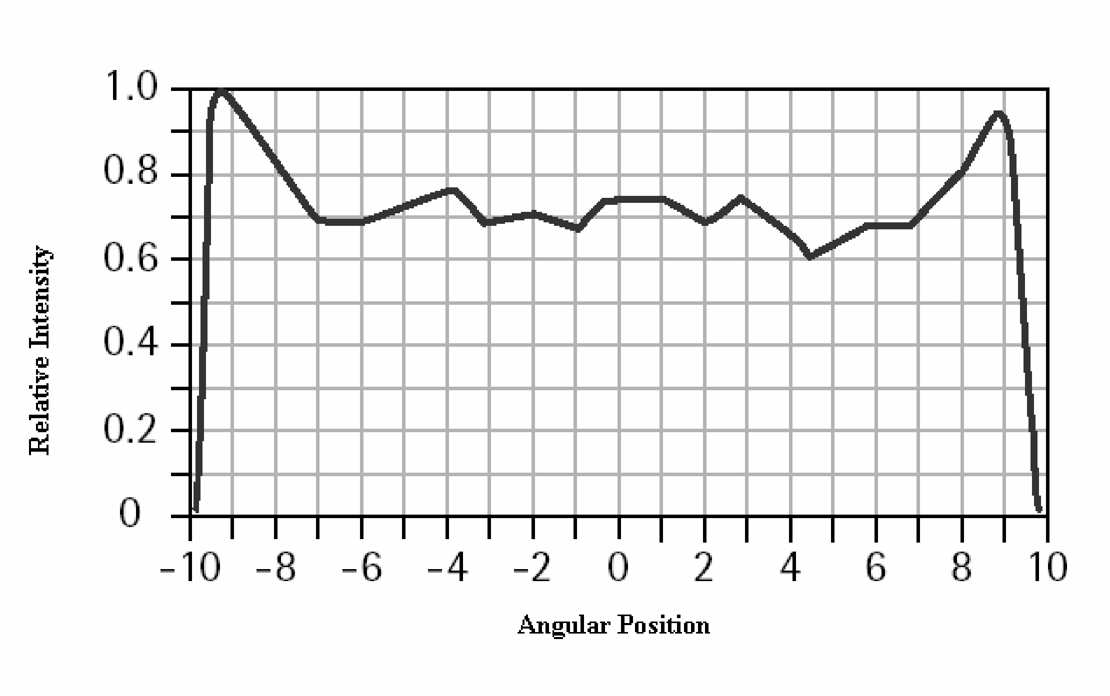

Figure 42. Laser intensity profile along line length

# Appendix C

### Equation 26 deduction.

From Figure 23, point P(v,u) is a point in vu coordinate system. It can be deducted that

$$\begin{bmatrix} v' \\ u' \end{bmatrix} = \begin{bmatrix} (v - v_0) - (u - u_0)\cot\theta \\ (u - u_0)/\sin\theta \end{bmatrix}, \tag{75}$$

From Equation 75, Equation 26 can be deducted.

# Appendix D

## Calibrated Camera Parameters

Left Camera:
Extrinsic parameters:

Translation matrix: T = [ -71.722027 4.371491 578.226395 ]

$$R = \begin{bmatrix} 0.999983 & -0.005376 & -0.002233 \\ -0.002182 & -0.701870 & 0.712302 \\ -0.005397 & -0.712285 & -0.701869 \end{bmatrix}$$

Rotation matrix: R = [ 0.999983 -0.005376 -0.002233
-0.002182 -0.701870 0.712302
-0.005397 -0.712285 -0.701869 ]

Intrinsic parameters:

Focal Length: f = [ 1780.10076 894.26278 ]

Principal point: c = [ 319.50000 99.50000 ]

Skew: α = [ 0.00000 ]

Distortion: k =[ -0.21403 -2.60592 ]

# Appendix E

## Calibrated Camera Parameters

Right Camera:

Extrinsic parameters:

Translation matrix: T = [ 80.040955 -19.352696 578.761503 ]

Rotation matrix: R = [ -0.999933 -0.003121 -0.011189

0.005432 0.725837 -0.687845

0.010268 -0.687860 -0.725771 ]

Intrinsic parameters:

Focal Length: f = [ 1803.65762 902.53550 ]

Principal point: c = [ 319.50000 99.50000 ]

Skew: α = [ 0.00000 ]

Distortion: k = [ -0.43360 5.38559]

# Appendix F

Table 9. X-ray data used for calibration.

| H(mm)<br>L(mm) | 10 | 20 | 30 | 40 | 50 | 60 | 70 |
|---|---|---|---|---|---|---|---|
| 10 | 25.841 | 24.165 | 22.489 | 20.759 | 17.493 | 14.889 | 12.779 |
| 20 | 54.252 | 52.830 | 51.408 | 49.805 | 46.802 | 44.304 | 42.472 |
| 30 | 82.500 | 81.307 | 80.115 | 79.172 | 76.3095 | 74.310 | 72.9687 |
| 40 | 109.920 | 109.457 | 108.991 | 107.951 | 106.132 | 104.312 | 102.7593 |
| 50 | 137.840 | 137.818 | 137.801 | 137.040 | 135.185 | 133.804 | 132.864 |
| 60 | 167.110 | 166.629 | 166.145 | 166.442 | 164.294 | 163.255 | 162.860 |
| 70 | 194.990 | 195.092 | 195.192 | 194.935 | 193.981 | 193.218 | 192.967 |
| 80 | 222.570 | 223.298 | 224.029 | 224.409 | 223.338 | 222.934 | 223.049 |
| 90 | 251.510 | 252.099 | 252.683 | 253.190 | 252.332 | 252.492 | 253.136 |
| 100 | 279.340 | 280.389 | 281.440 | 282.830 | 282.358 | 282.493 | 283.419 |
| 110 | 307.450 | 308.819 | 310.186 | 311.379 | 311.8485 | 312.7885 | 313.8945 |
| 120 | 335.410 | 337.187 | 338.967 | 340.726 | 340.978 | 342.103 | 344.114 |
| 130 | 363.410 | 365.288 | 367.163 | 369.549 | 370.522 | 371.807 | 373.325 |
| 140 | 390.590 | 393.275 | 395.958 | 398.703 | 399.731 | 401.463 | 403.759 |
| 150 | 418.950 | 421.890 | 424.835 | 427.911 | 429.226 | 431.044 | 433.801 |
| 160 | 448.170 | 451.071 | 453.977 | 456.891 | 458.751 | 461.057 | 463.955 |

# Appendix G

Table 10. Data used to produce result in Figure 30 showing error after the Laser 3D geometrical correction.

| Distance to center(pixel) | Error (pixel) | Distance to center(pixel) | Error (pixel) |
|---|---|---|---|
| 4.2 | 0.05 | 173.1 | 0.37 |
| 10.2 | 0.05 | 182.0 | 0.25 |
| 16.3 | 0.14 | 183.6 | 0.49 |
| 33.6 | 0.16 | 199.8 | 0.52 |
| 49.8 | 0.16 | 201.6 | 0.66 |
| 51.6 | 0.07 | 216.5 | 0.56 |
| 66.5 | 0.08 | 217.2 | 0.59 |
| 68.4 | 0.09 | 218.4 | 0.46 |
| 78.5 | 0.17 | 227.8 | 0.67 |
| 84.4 | 0.39 | 228.5 | 0.40 |
| 85.7 | 0.32 | 234.4 | 0.75 |
| 90.7 | 0.43 | 235.1 | 0.56 |
| 91.8 | 0.08 | 235.7 | 0.70 |
| 107.8 | 0.39 | 240.7 | 0.82 |
| 115.1 | 0.21 | 241.3 | 0.74 |
| 121.3 | 0.21 | 241.8 | 0.85 |
| 124.8 | 0.23 | 244.8 | 0.66 |
| 128.6 | 0.25 | 248.6 | 0.89 |
| 135.5 | 0.26 | 255.5 | 0.79 |
| 150.8 | 0.28 | 270.8 | 1.20 |
| 154.2 | 0.28 | 279.8 | 0.93 |
| 156.3 | 0.19 | 284.9 | 0.90 |
| 160.2 | 0.31 | 290.6 | 0.84 |
| 164.9 | 0.27 | 293.1 | 0.96 |
| 170.6 | 0.37 | 302.0 | 0.79 |

1 pixel = .4 mm x .4 mm

# Appendix H

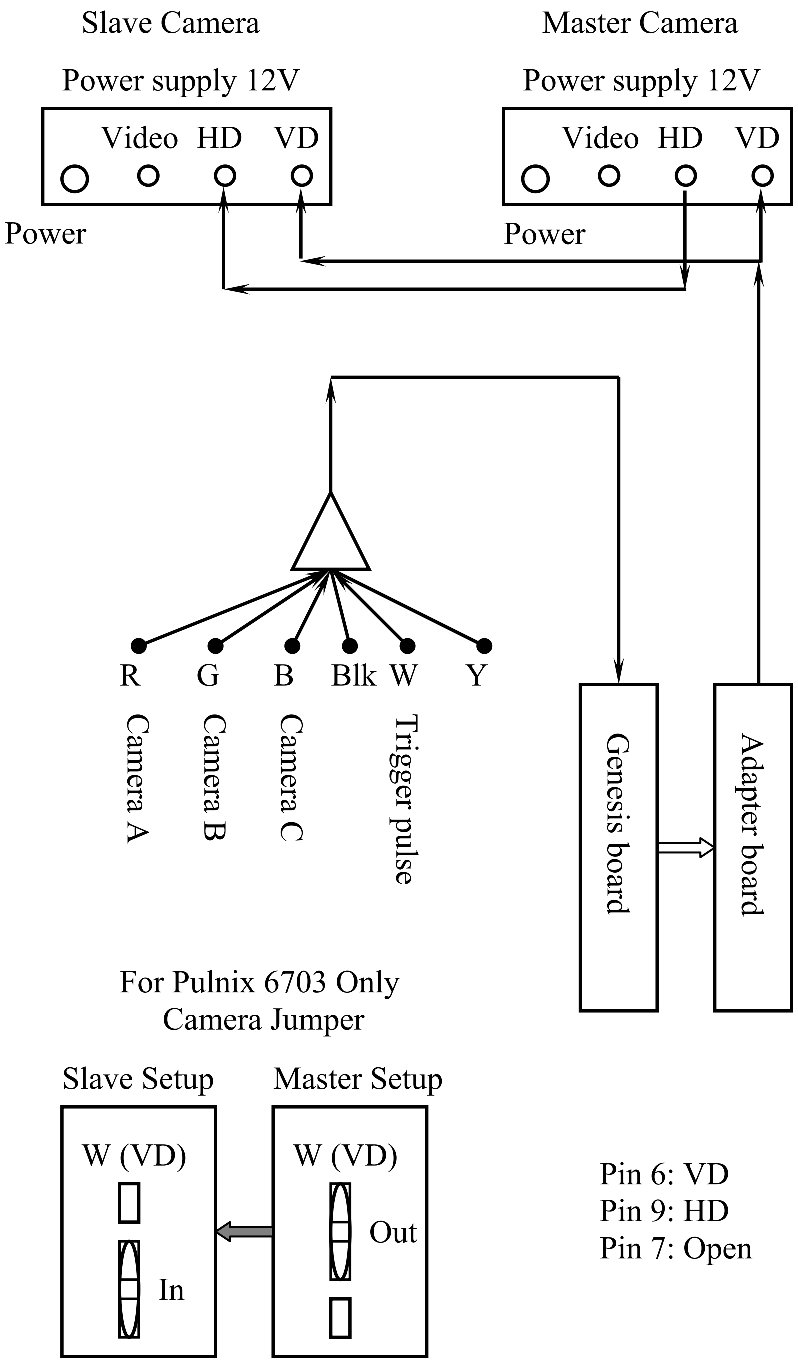

Figure 43. Camera connection graph.

# Appendix I

## Sample Laser Range images

(The image intensity indicates the thickness of the object)

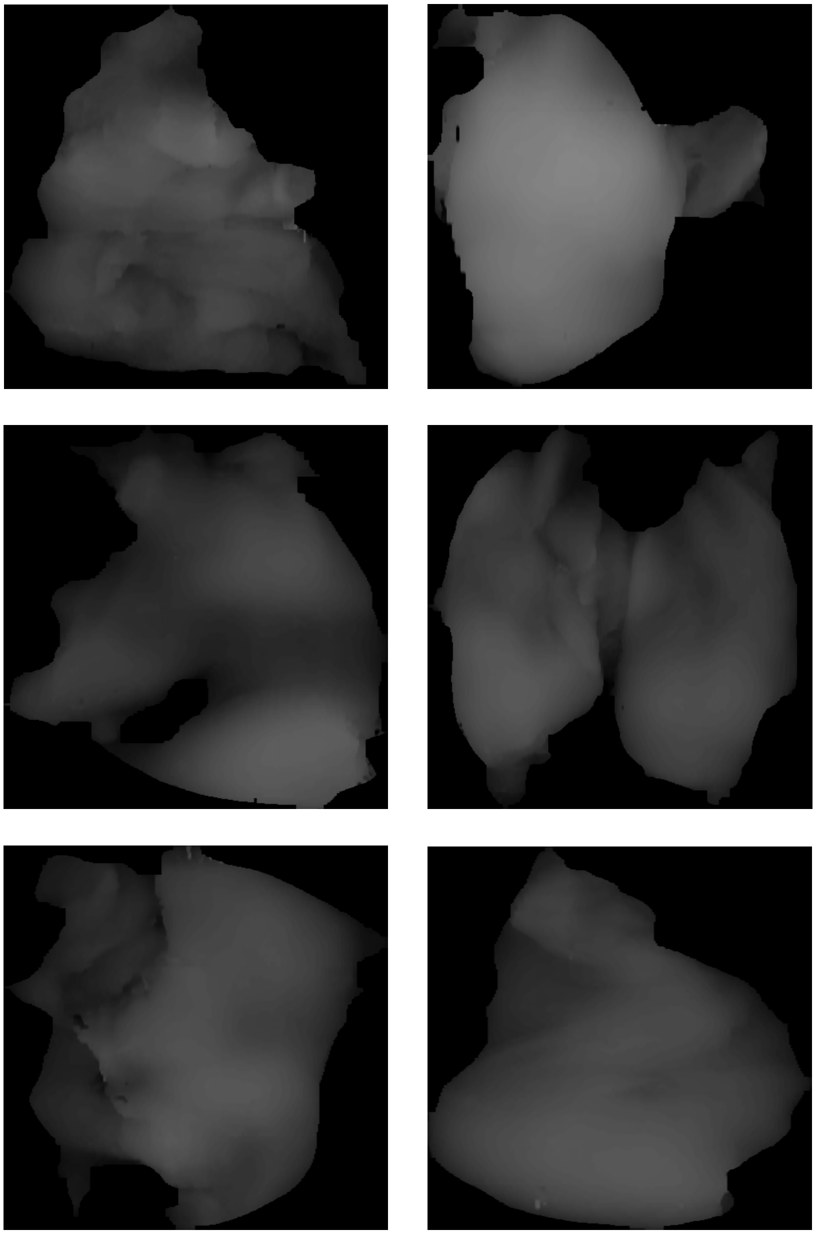

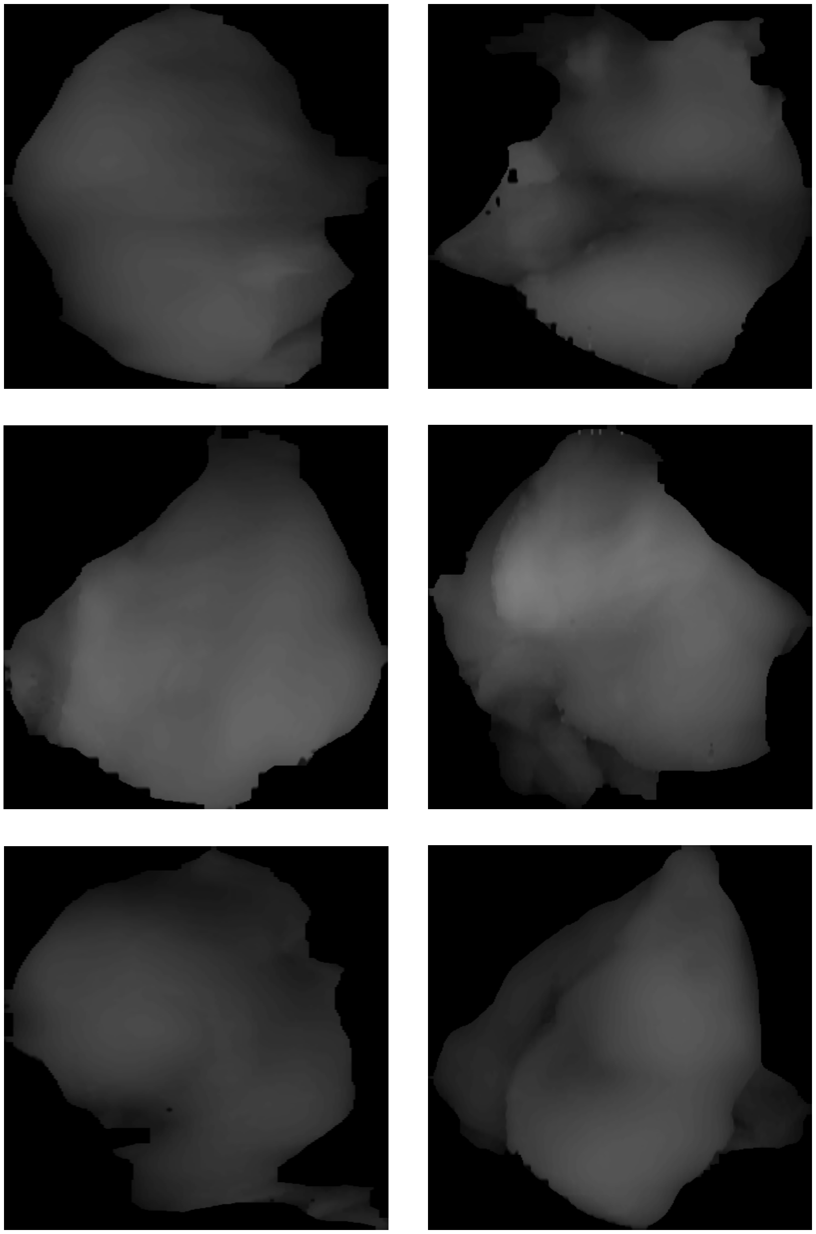

Figure 44. Typical laser 3D images (The image intensity indicates the thickness of the object)

# Appendix J

Typical Pseudo-X-ray images

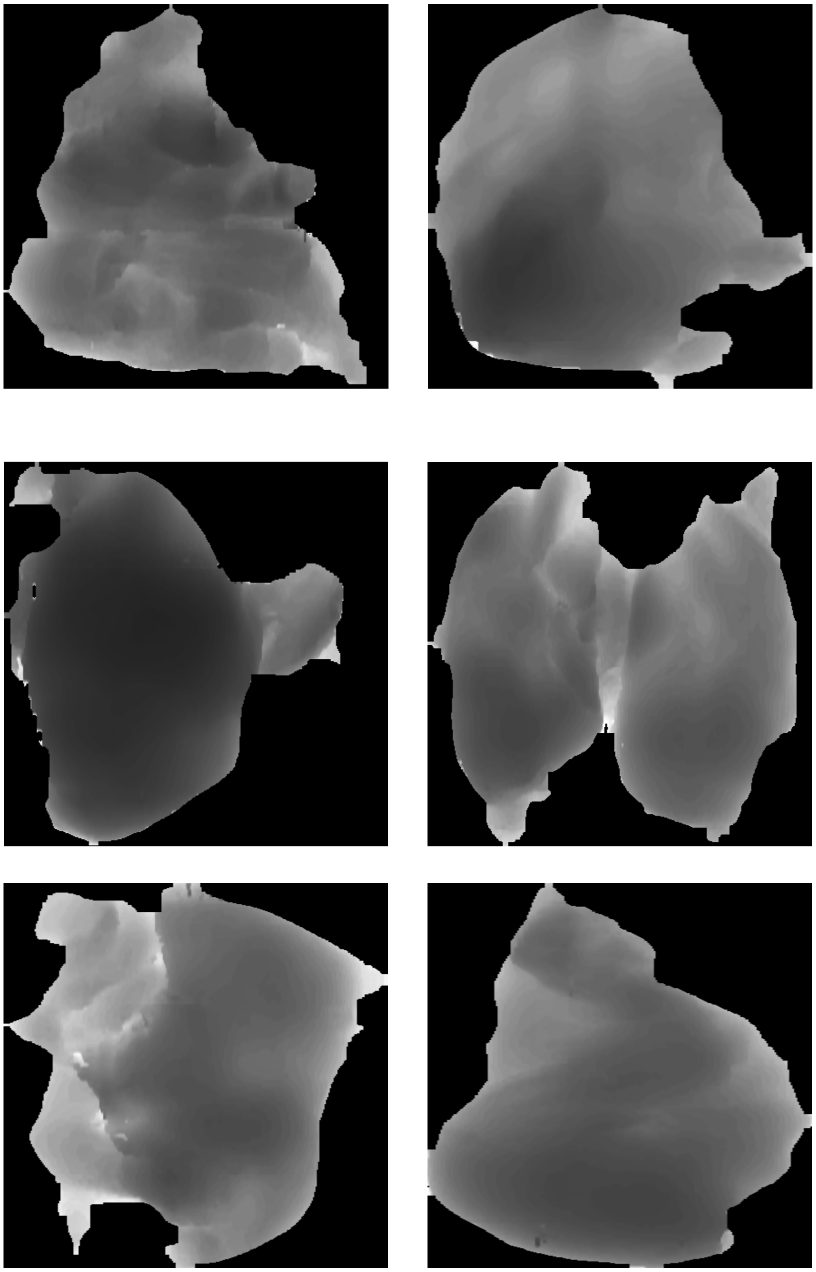

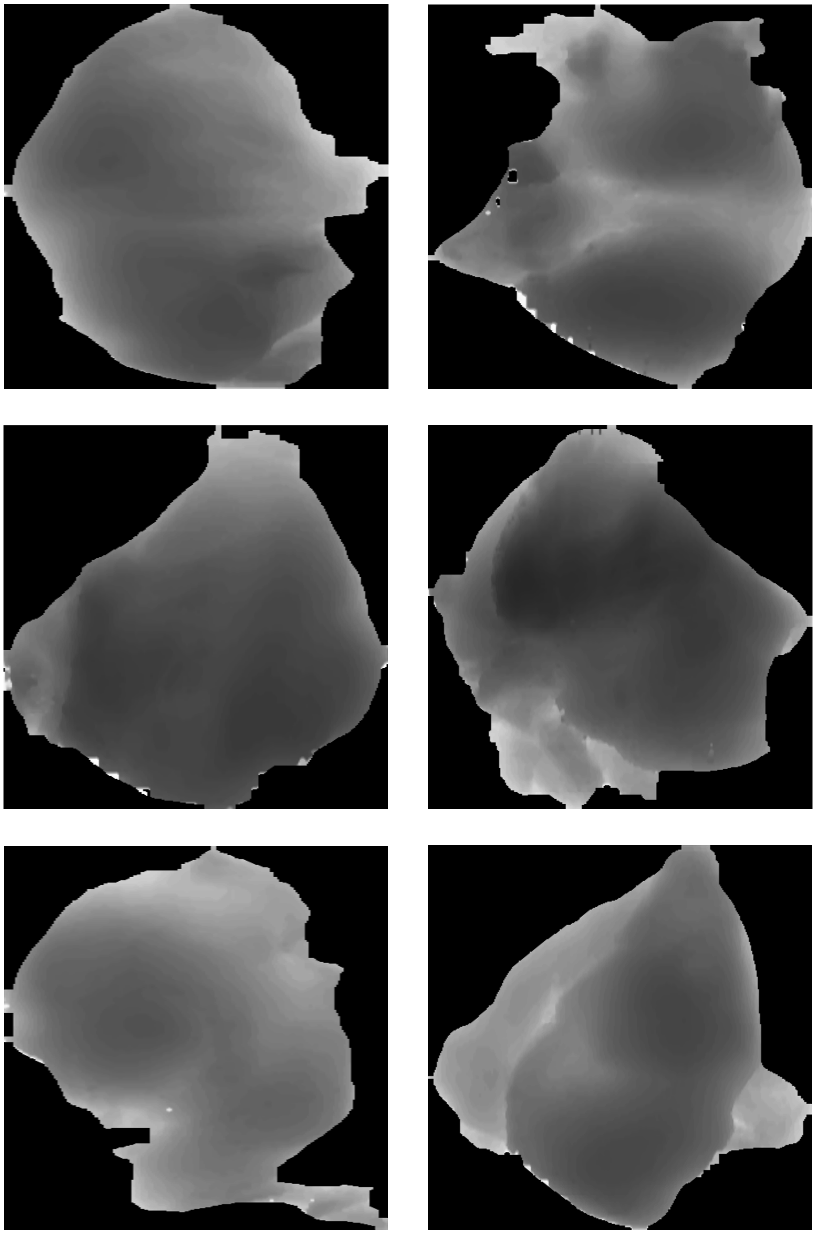

Figure 45. Selected Pseudo-X-ray images.

# BIBLIOGRAPHY

Abdel-Aziz, Y. I., H. M. Karara. 1971. Direct linear transformation into object space coordinates in close-range photogrammetry. *Proc. Symp. Close-Range Photogrammetry* 1-18.

Alberts, B., A. Johnson, J. Lewis, M. Raff, K. Roberts, and P. Walter. 2002. Molecular Biology of the Cell. New York, NY: Garland Pub.

Alexander, B. F. and K. C. Ng. 1991. Elimination of systematic error in subpixel accuracy centroid estimation, *Optical Engineering* 30(9):1321~1331.

Alison, J., R. G. Nobel, M. Joe, S. Andrea and I. H. Richard. 1998. High precision X-ray stereo for automated 3D cad-based inspection. *IEEE Transactions on Robotics and Automation* 14(2):292-303.

Andrews, D. F., P. J. Bickel, F. R. Hampel, P. J. Huber, W. H. Rogers, and J. W. Tukey 1972. Robust Estimations of Location. Princeton. NJ: Princeton University Press.

Askey, R. and D. T. Haimo. 1996. Similarities between fourier and power series. *American Mathematic Monthly* 103:297-304.

Baribeau, R. and M. Rioux. 1991a. Centroid fluctuations of speckled targets. *Applied Optics* 30(20).

Baribeau, R. and M. Rioux. 1991b. Influence of speckle on laser range finders. *Applied Optics* 30(23):2873-2878.

Barnett, V. and T. Lewis. 1994. Outliers in Statistical Data. Chichester: John Wiley & Sons.

Bates, D. M. and D. G. Watts. 1988. *Nonlinear Regression and Its Applications.* New York: Wiley. Pp: 3-4.

Boerner, H., and B. Strecker. 1988. Automated X-ray inspection of aluminum castings, *IEEE Transactions On Pattern Analysis And Machine Intelligence* 10(1), 79-92.

Brecht, J. K. R. L. Shewfelt, J.C. Garner and E. W. Tollner. 1991. Using X-ray computed tomography to nondestructively determine tomato maturity. *Horticultural Science* 26(1):45-47.

Brown D.C. 1971. Close-range camera calibration. *Photogrammetric Engineering* 37(8): 855-866.

Bumbaca, F., F. Blais and M. Rioux. 1986. Real-time correction of three-dimensional nonlinearities for a laser rangefinder. *Optical Engineering* 25(12):561-572.

Caspi, D., N. Kiryati and J. Shamir. 1998. Range imaging with adaptive color structured light. *IEEE Transactions on Pattern Analysis and Machine Intelligence* 20(5).

Chan, C. L., A. K. Katsaggelos, and A. V. Sahakian. 1993. Image Sequence filtering in quantum-limited noise with applications to low-dose fluoroscopy. *IEEE Transactions on Medical Imaging* 12(3):610-622.

Chen, X. 2003. Detection of physical hazards in boneless poultry product using combined x-ray and laser range imaging technologies. Ph.D. diss., University of Maryland at College Park.

Chen, Y. R., D. R. Massie and W.R. Hruschka. 1992. Detection of abnormal (septicemic and cadaver) poultry carcasses by visible-near-infrared spectroscopy. *Food Processing Automation. ASAE. Vol III: 193-204.*

Chu, B. 1974. Laser Light Scattering. New York, Academic Press. Pp:16-17.

Chynoweth, D. P. 2003. Biology for engineers. [Online]. Available: WWW: http://www.agen.ufl.edu/~chyn/age2062/lect/lect_19/146.gif.

Cohen, M. and J. R. Wallace. 1993. *Radiosity and Realistic Image Synthesis*. Academic Press.pp:28-30.

Cook R. L.and K. E. Torrance. 1981. A reflectance model for computer graphics. *Computer Graphics* 15(3):301-316.

Cortelazzo, G. M., G. Doretto, L. Lucchese, and S. Totaro. 1998. A frequency domain method for registration of range data. *Proceedings of the 1998 IEEE International Symposium on Circuits and Systems* 5:518-512.

Custer, H. 1993. Inside Windows NT. Redmond:Washington. Microsoft Press. Pp:44-60.

Deng, K. and J. Wang. 1994. Nanometer-resolution distance measurement with a noninterferometric method. *Applied Optics* 33:113-16.

Devic, S., J. I. Monroe, S. Mutic, B. Whiting, and J. F. Williamson. 2000 Dual energy CT tissue quantization for Monte-Carlo based treatment planning for brachytherapy. *Engineering in Medicine and Biology Society, 2000. Proceedings of the 22nd Annual International Conference of the IEEE Vol 1* 23-28 July. pp: 364-367.

Dunn, A. K. 1997. Light scattering properties of cells. Ph. D. diss., University of Texas at Austin, pp:2-3.

EG&G. Inc. 1995. An X-ray Inspection Overview.

Farebrother, R. W. 1988. Linear Least Squares Computations. *New York, Marcel Dekker.* pp:120:142.

Farid, H. and E. P. Simoncelli. 1998. Range estimation by optical differentiation. *Journal of the Optical Society of America. A, Optics, Image Science, and Vision* 15(7):1777-86.

Fillard, J. P. 1992. Subpixel accuracy location estimation from digital signals, *Optical Engineering* 31( 11): 2465~2471.

Foley, J. D, A. Dam, S. K. Feiner, and J. F. Hughes. 1990. *Computer Graphics: Principles and Practice*. Addison-Wesley, second edition.

Forsyth, D. A. and J. Ponce. 2002. *Computer Vision, A Modern Approach*, Prentice Hall.pp:144-164.

Frankot, R. T. and R. Chellappa. 1987. Application of a shape from shading technique to SAR imagery. *Proceedings IEEE International Geoscience & Remote Sensing Symposium,* Ann Arbor, MI, May. Pp:285-289.

Fuller, W. A. 1987. Measurement Error Models. New York:John Wiley & Sons, Inc.

Gao, F., Y. Jin, X. Li, C. Schaaf, and A. H. Strahler. 2002. Bidirectional NDVI and Atmospherically Resistant BRDF Inversion for Vegetation Canopy, *IEEE Transanction on Geoscience and. Remote Sensing*. 40:1269-1278.

Geng, Z. 1997. Color ranging method for high speed low-cost three dimensional surface profile measurement. United States Patent No. 5,675,407.

Gibson, J. S., G. H. Lee, and C. F. Wu. 2000. Least-squares estimation of input/output models for distributed linear systems in the presence of noise. *Automatica* 36:1427-1442.

Glaser, I. K. and W. N. Konforti. 1992. Parallel range-image acquisition by astigmatic defocus. *Applied Optics* 31:6594-6597.

Godhwani, A., G. Bhatia and W. Vannier. 1994. Calibration of a multisensor structured light range scanner. *Optical Engineering* 33(10):1359-67.

Grant, M., R. S. Stevens and J. Norbert. 2001. Alignment of a volumetric tomography system. *Medical Physics* 28(7):1472-1482.

Gronenschild, E. 1997. The accuracy and reproducibility of a global method to correct for geometric image distortion in the X-ray imaging chain. *Medical Physics* 24(12):1875-1889.

Harrison, R. D., W. A. Gardner, E. W. Tollner and D. J. Kinard. 1993. X-ray computed tomography studies of the burrowing behaviour of forth-instar pecan Wevil (Coleoptra: Curculionidar). *J. Econ. Entomolo.* 86(6):1714-1719.

Hastreiter, P. and T., Ertl. 1998. Integrated registration and visualization of medical image data. *Proceedings Computer Graphics Internationa.* 78 -85

Headus, Inc, 2003. Osborne Park, WA, Australia.

Heikkila, J., 2000. Geometric camera calibration using circular control points. *IEEE Transactions on Pattern Analysis and Machine Intelligence* 22: 1066-1077.

Horn, K. P., Hilden, H. M, and S. Negahdaripour, 1988, Closed form solution of absolute orientation using orthonormal matrics. *J. Opt. Soc. Am. A.* 5:1127-1135.

Hubbell, J. H. and S. M. Seltzer. 1997. Tables of X-ray mass attenuation coefficients and mass energy-absorption coefficients (version 1.03), [Online]. Available: http://physics.nist.gov/xaamdi [2003, July 20]. National Institute of Standards and Technology, Gaithersburg, MD.

Huertas, A. 1986. Detection of intensity changes with subpixel accuracy using laplacian-gaussian masks. *IEEE on Pattern Analysis and Machine Intelligence* 8(5):651-665.

Jain, A. K. 1989. *Fundamentals of digital image processing.* Englewood Cliffs, Prentice Hall.pp:268-274.

Jeffrey D. H., M. A. Stephen, and S. R. McNeil. 1994. Three dimensional image correlation for surface displacement measurement. *Videometrics III, Proceedings of SPIE* 2350: 32-45.

Jing, H., Y. Tao and Y. Ying. 1999. Real-time high-resolution 3D laser range imaging of poultry products. *American Society of Agricultural Engineerings(ASAE) paper No*. 993169.Vancouver:Canada.

Jing, H., Y. Tao and Y. Ying. 2000. Dual camera real time thickness detector for poultry meat. *American Society of Agricultural Engineerings(ASAE) paper No. 003162*. Milwaukee:WI.

Jones, M. and J. Regehr. 1999. The problem you’re having may not be the problems you think you’re having: results form a latency study of Windows NT, *Proceedings of the Seventh Workshop on Hot Topics in Operating Systems, Rio Rico, Arizona. IEEE Computer Society.*

Kanatani, K. 1993. *Geometric computation for machine vision*. New York, Oxford University Press Inc. pp:100-130.

Kim, J. and J. Lin. 1998. Successive Order scattering transport approximation for laser light propagation in whole blood medium. *IEEE Transactions On Biomedical Engineering* 45(4):505-511.

Krishnan, A. and N. Ahuja. 1996. Range estimation from focus using a non-frontal imagine camera. *International Journal of Computer Vision* 20(3):169-185.

Lawrie, R. A. 1991. Meat Science. Elmsford, New York. Pergamon Press. Pp:28-30.

Manthey, D. W., K. N. Knapp and D. Lee. 1994. Calibration of a laser range-finding coordinate-measuring machine. *Optical Engineering* 33:3372-80.

Marks, D. 1999. 3D camera has no lens, great depth of field. *Science*. 284(5423):2066-2067.

Mery, D. and D. Filbert, 2002. Automated flaw detection in aluminum castings based on the tracking of potential defects in a radioscopic image sequence. *IEEE Transactions on Robotics and Automation* 18(6):890-902.

Michael, D. 2003. Animal Cell Structure. [Online]. Available WWW: http://micro.magnet.fsu.edu/cells/animalcell.html

Morita, K., S. Tanaka, C. Thai and Y. Ogawa. 1997. Development of soft X-ray imaging for detecting internal defects in food and agricultural products. *Proc. From the Sensors for Nondestructive Testing Int. Conf.,*305:315. Orlando, FL..

Motluk, A. 1997. Brain in the round. ultrasound can now produce a three-dimensional image of the human brain. *New Scientist* 155:7.

MSDN. 1998. Microsoft Developers Network Web Pages. [Online]. Available WWW: http://msdn.microsoft.com/library/default.asp?url=/library/en-us/dndllpro/html/msdn_realtime.asp

Munier, B. and W. R. House. 1989. X-ray detection of foreign bodies. *European Food & Drink Review*. 39:41-42.

NCI, 2003. Structure of skeletal muscle. [Online], Available: WWW: http://training.seer.cancer.gov/module_anatomy/unit4_2_muscle_structure.html.

Nobel, A. J., J. Mundy, A. Schmitz, and R. I. Hartley. 1998. High precision X-ray stereo for automated 3D cad-based inspection. *IEEE Transactions on Robotics and Automation* 14(2): 292-303.

Norman, R. and H. S. Draper, 1998. *Applied Regression Analysis*. New York, Wiley-Interscience.pp:567-585.

Papanicolopoulos, C., J. C. Wyvill, W. Dayley and W. Owens. 1992. A feasibility study relative to the development of an on-line X-ray system that accurately detects bone and cartilage fragments in poultry meat. Final report to Southeastern Poultry & Egg Association, SPEA research project #80, December.

Pirlet, R., J. Boelens and J. Salmon. 1986. Optical systems for dimensional control in hostile environments. *Optical Techniques for Industrial Inspection, Proceedings of SPIE. V 665:61-68. Quebec City, Canada.*

Poelman, C. J. and T. Kanade. 1993. A Paraperspective factorization method for shape and motion recovery. School of Computer Science, Carnegie Mellon Univeristy, Pittsburgh, PA.pp:206-219.

Popp A. K., M. T. Valentine, P. D. Kaplan, and D. A. Weitz. 2003. Microscopic origin of light scattering in tissue. *Applied Optics* 42(16):2871-2880.

Posudin, Y. I. 1998. Lasers in Agriculture.Enfield, New Hampshire. Science Publishers, Inc.

Poultry companies (Tyson, Inc. and Perdue, Inc.), personal communication. Fayetteville, AR.,1998.

Pratt, W. 1991. Digital Image Processing. 2nd Ed. A Willey-Interscience Plubication, John Willey & Sons, Inc. pp: 104-105.

Qjidaa, H. and L. Radouane. 1999. Robust line fitting in a noisy image by the method of moments. *IEEE Transactions on Pattern Analysis and Machine Intelligence* 21(11):1216-1224.

Ramamritham, K. and C. Shen. 1998. Using Windows nt for real-time applications: experimental observations and recommendations. *Proceedings of the Fourth IEEE Real-Time Technology and Applications, Denver, CO.* pp:102 -111.

Redus, R., J. Pantazis, A. Huber, and T. Pantazis. 2002. Improved sensitivity X-ray detectors for field applications. *IEEE Transactions on Nuclear Science* 49(6):3247 - 3253.

Reimar, K. and R. Y. Lenz (1988). Techniques for calibration of the scale factor and image center for high accuracy 3D machine vision metrology. *IEEE Transactions on Pattern Analysis and Machine Intelligence* 10(5):713-721.

Renesse, R. L. and J. W. Klumper. 1993. Glass in foods: prevention is not always possible. *Vodeings Middelen Technology* 26(24):31-34.

Richardson, R. I. and G. C. Mead. 1999. Poultry Meat Science. Poultry Science Symposium Series, Vol. 25. CABI Publishing, Abingdon, Oxfordshire.

Rioux, M. J. Beraldin and O. M. Angelo. 1991. Eye-safe laser scanner for range imaging. *Applied Optics* 30:2219-23.

Ryon, R.W., H. E. Martz, J.M. Hemanclez, J. J. Haskins, R. A. Day, J. M. Brase, B. Cross, and D. Wherry. 1988. X-ray imaging: Status and trends. *Advances in X-ray Analysis* 31(1):35-52.

Schatzki, T. F., R. Young, R. P. Haff, J. G. Eye and G. R. Wright. 1996. Visual detection of particulates in X-ray images of processed meat products. *Optical Engineering* 35(8):2286-2291.

Schatzki, T. F., R. Young, R. P. Haff, R. Young, I. Can, L-C. Le and N. Toyofuku. 1997. Defect detection in apples by means of X-ray imaging. *Proc. From the Sensors for Nondestructive Testing Int. Conf., 161-171. Orlando, FL..*

Seta, K. and T. O'ishi. 1990. Distance meter utilizing the intermode beat of a He-Ne laser. *Applied Optics* 29:354-359.

Shen T. and C. Menq. 2001. Automatic camera calibration for a multiple-sensor integrated coordinate measurement system. *IEEE Transactions on Robotics and Automation,* 17(4):502-507.

Shortis, M.R., T.A. Clarke, and T. Short, A, 1994. Comparison of some techniques for the subpixel location of Discrete Target Images, *Videometrics III, SPIE* 2350:239~250.

Solomon, D.A. 1998. The Windows NT Kernel Architecture. Redmond:Washington. Microsoft, Chapter 1:1:25.

Sorgel, W. 1997. Efficient and accurate structured light algorithm for direct measurement of cylindrical surface parameters. *Optical Engineering* 36(1):73-84.

Strand, T. C. 1985. Optical three-dimensional sensing for machine vision. *Optical Engineering* 24(1):33-40.

Tao, Y. 1996. Spherical transform of fruit images for on-line defect extraction of mass objects. *Optical Engineering* 35(2):344-350.

Tao, Y. 1997. Highly sensitive imaging detection of physical contamination on poultry packing lines. . Proc. the *USDA Food Safety Consortium* Annual Meeting,. pp. 53-57. Oct. Kansas City, MO.

Tao, Y. 1999. Sensor-fused X-ray imaging system for contaminant detection on food processing lines. ASAE paper no. 99-3160. Presented at the ASAE 1999 International Annual Meeting. July 18-21, Toronto, Canada. The American Society of Agricultural Engineering, St. Joseph, MI.

Tao, Y. and J. G. Ibarra, 2000. Thickness-compensated X-ray imaging detection of bone fragments in deboned poultry: Model analysis. *Trans. ASAE* 43(2):453-459.

Tao, Y., Z. Chen, H. Jing, and J. Walker. 2001. Internal inspection of deboned poultry using X-ray imaging and adaptive threshoulding. *Transactions of the ASAE* 44(4):1005-1009.

Thai, C. N., J. N. Pease and E. W. Tollner. 1991. Determination of green tomato maturity from X-ray computed tomography images. *Proc. Symposium on Automated Agriculture for the 21th Century. ASAE pub 11-91:134-143.*

Thermo Goring Kerr, Inc.. 2003. Markham, Ontario,Canada.

Timmerman, M. 1998. Windows NT as real-time OS. *Real Time Magazine. http://www.realtime-info.be.*

Tollner, E. W. and C. Murphy. 1991. Factors affecting soil x-ray absorption coefficient with computer tomography. *Trans. of ASAE* 34(3):1047-1053.

Tollner, E. W. 1993. X-ray technology for detecting physical quality attributes in agricultural produce. *Posthavest News and Information* 4(6):3-10.

Touraille, C. R., F. H. Kopp, C. Valin and B. Leclercq. 1981 Chicken meat quality. 2. Changes with age of some physico-chemical and sensory characteristics of meat. *Archives Geflugeljunde* 45:97-104.

Tsai, R. Y. 1987. A versatile camera calibration technique for high-accuracy 3d machine vision metrology using off-the-shelf tv cameras and lenses. *IEEE Journal Of Robotics And Automation* 3(4):323-344.

Tukey, J. W. 1977. Exploratory Data Analysis. Addison-Wesley, ISBN: 0201076160. Chapter 3:31:51.

USDA. 1998. Agriculture Fact Book, Edition:1: 26

USDA. 1999. Economic Research Service, *Poultry Yearbook*:64, 109.

Valkenburg, R. J., A. M. McIvor, and P. W. Power. 1994. An evaluation of subpixel feature localization methods for precision measurement, *Videometrics III, SPIE* 2350:229-239.

Wagner, F. C., A. Macovski, and D. G. Nishimura. 1989. Effects of scatter in dual-energy imaging: an alternative analysis. *IEEE Transactions on Medical Imaging* 8(3):236-244.

Wei, G. and S. Ma. 1994. Implicit and explicit camera calibration: theory and experiments. *IEEE Transactions on Pattern Analysis and Machine Intelligence* 16(5):469-481.

Weiss, I.. 1989. Line fitting in a noisy image. *IEEE Transactions on Pattern Analysis and Machine Intelligence,* 11(3):325-329.

Wojcik, R., S. Majewski, F. R. Parker, and W. P. Winfree. 1996. Single shot dual energy reverse geometry X-radiography (RGX)**.** *Nuclear Science Symposium, IEEE , Volume: 2 , 2-9 Nov.* 811-815.

Zhang, Z. 1996. Parameter estimation techniques: a tutorial with application to conic fitting. *International Journal of Image and Vision Computing*. 15:59-76

Zhang, Z. 1999. Flexible camera calibration by viewing a plane from unknown orientations. The Proceedings of the Seventh IEEE International Conference on Computer Vision, 1:666-673.

Zhao, F. and D. Jiang. 1992. Multiple decomposition technique for dual energy X-ray image. *Proceedings of the Annual International Conference of the IEEE , Volume: 5 , October 29- November 1.* 1778 -1779.

Zhao W. and R. Chellappa. 2001. Symmetric shape from shading using self-ratio image, *Intl. J. Computer Vision* 45:55-75.

Zhou, X. S., R. Yin and W. Wang. 2000. Calibration, parameter estimation, and accuracy enhancement of a four-dimensional imager camera turntable system. *Optical Engineering* 39:170-174.